Collisions between Jupiter-like planets

Tobias Albertsson

Lund Observatory
Lund University

2010-EXA42

Degree project of 60 higher education credits (for a degree of Master)
June 2010

Lund Observatory
Box 43
SE-221 00 Lund
Sweden

Acknowledgements

First and foremost I want to thank my supervisor Dr. David Hobbs for his support and invaluable help during this project. I would also like to thank my co-supervisor Pr. Melvyn Davies which have helped me a lot by providing essential inputs during the project. My office mate Fredrik Windmark has helped a lot and I am grateful for the countless helpful discussions over the years.

I wish to extend additional thanks to my fellow Master students; Nils Håkansson, Hannes Jensen and Carina Lagerholm, for the support and good times together during these two years. Special thanks also to Daniel Malmberg for his tireless help with the computers.

Finally, I want to thank all my family and friends who have supported and encouraged me to pursue my interests.

Sammanfattning

Med hjälp av tredimensionella datorsimulationer har vi studerat utfallen från kollisioner mellan planeter. Målet med projektet var att utreda beroendet av kollisionsparametrar som till exempel avståndet vid närmaste passage, hastighet och planeternas massor.

Vi kom fram till att planeterna kan bli gravitationellt bundna efter kollisionerna på grund av energiförluster som gör att de eventuellt kolliderar igen och sammansmälter. Vissa kollisioner kan även sammansmälta direkt om planeterna kolliderar tillräckligt våldsamt.

Där kollisioner inte är tillräckligt våldsamma för att planeterna ska bli bundna efteråt, kan ändå markanta skillnader i planeternas strukturer observeras. I kollisionerna kommer planeterna förlora både massa och energi, vilket vi bestämmer och undersöker hur det beror på hur nära planeterna är varandra under kollisionen och deras hastigheter.

Result från detta projekt kan hjälpa att förstå vilka typer av kollisioner mellan planeter som kan förekomma och vilka resultat vi kan förvänta oss som kan observeras i framtiden.

Abstract

Using three-dimensional smoothed particle hydrodynamics (SPH) simulations, we have studied the outcomes from collisions between Jupiter-like planets. Planet models have been generated from polytropic profiles using a polytropic index of n=1 and each planet is represented by 15,000 particles. The dependency on a range of parameters specifying the point of closest approach, velocity at infinity and masses of the planets have been considered and discussed. From a range of collisions, we studied the effect of different collision parameters.

After the collision, the planets may become gravitationally bound due to energy loss, and eventually merge. Some collisions might instantly merge if the collision is close enough to head-on.

For collisions not violent enough for the planets to become gravitationally bound, the planets might be disrupted, resulting in small mass loss and two planetary remnants. Most encounters result in some mass loss. The results may help understanding what kind of collisions can occur and the expected outcomes, which can be used to identify possible remnants that could be observed in the future.

Contents

1 Introduction

The study of extra-solar planets, or exoplanets for short, is a research topic that has gained a lot of interest since the first confirmed observations of an exoplanet orbiting a main-sequence star (Mayor & Queloz 1995). Since then, over 450 exoplanets have been observed, and the growing sample constantly improves our understanding of planets and their formation scenarios. In the near future, we can expect a great boost in our knowledge of exoplanets. Projects such as Kepler (Borucki et al. 2003), which has begun gathering data already, and GAIA (Perryman 2003; Lindegren 2010), which is expected to see first light in 2012, will greatly enhance our understanding of exoplanets and planet formation. It is believed that early collisions may account for the build up of massive planets to some extent, and in this project, we evaluate different types of collisions to determine which lead to mergers and study the mass exchange.

The formation of planets and planetary systems is one of the primary goals of exoplanet research, something for which, before the findings of Mayor & Queloz (1995), we only had our own Solar system to compare with. The standard model for planet formation was proposed by Safronov (1972) and suggests that gravity causes the dust particles in a gaseous disc around a star to collide and accrete into larger bodies, so called planetesimals. Proto-planets are then formed through collisions and mergers of these small bodies, often ranging in diameters up to a few kilometers (Ida 2010).

Unusual planet properties have been observed in the solar system which the standard model cannot account for. The standard model suggests that a significant number of collisions take place during the later stages of planet formation, which may be able to explain these odd properties (Wetherill 1990).

Mercury has an unexpectedly high mass density, for which Urey (1951) has suggested a high fraction of iron versus silicate as an explanation. This was studied through numerical simulations by Benz et al. (1988), who found that a collisions with an object one-sixth of Mercury's mass could explain this with an impact velocity approximately five times the mutual escape velocity, stripping Mercury of its mantle.

Earth's moon is another example that points towards a violent history in our solar system. With a similar composition to that of the Earth's mantle, this suggests that the moon was formed from similar material, possibly through a collision early on in Earth's evolution (Wiechert et al. 2001). Simulations have shown this to be possible (Cameron & Benz 1991).

Several other examples exist, such as the unusual tilt of Uranus (Benz et al. 1989) and the formation of the Pluto-Charon system (Stern 1992; Canup 2005). These show how violent our solar system has been, and how much effect collisions in the last stages of planet formation can have. But our solar system cannot be a lone example of a planetary system with a violent history.

Observations of the brown dwarf 2M1207 revealed a companion, determined to be a large Jupiter-like planet companion, the properties of the 2M1207 system are

discussed in detail in Mohanty et al. (2007). Comparison between measured and synthetic spectra yielded the effective temperature $T_{\rm eff,A} \approx 2550\pm$ 150 K and $T_{\rm eff,B} \approx 1600\pm$ 100 K of the host and the planet respectively. Implementing these effective temperatures into evolutionary models yielded $M_{\rm A} \approx 24 \pm 6$ $M_{\rm J}$ and $M_{\rm B} \approx 8 \pm 2$ $M_{\rm J}$. However, the luminosities of the planet consistent with these masses only agree with measurements for $M_{\rm A}$, while $M_{\rm B}$ is ~ 2.5 mag fainter than expected. Mamajek & Meyer (2007) propose from these findings that the object 2M1207b is the aftermath from a planet collision early in the systems age. They estimate this should cause the planet to be significantly more metal-rich than its host, which will be an observable feature to distinguish which of the two scenarios is correct.

From Spitzer observations of the star HD 172555, Lisse et al. (2009) reported evidence of the aftermath of a collision between two rocky bodies. The observations revealed signatures of vaporized rock and pieces of refrozen lava which point to a previous planet collision. For this to happen they determined that a very violent collision must have occured recently, within the few last thousand years. Analyses of the debris suggest that the collision was between a Mercury- and moon-sized planet, and that the smaller planet was completely destroyed by the impact, flinging massive plumes of hot lava into space.

Collisions may be very violent and involve high rates of energies that are released at impact, which may invoke significant increases in the luminosity of the planets. Anic et al. (2007) investigated the results of collisions between a young Jupiter with an Earth-like planet with different ages of the young Jupiter and impact parameters. The giant planet's gaseous envelope was assumed to consist of a mixture of hydrogen and helium, and modeled using the equation-of-state (EOS) of Saumon et al. (1995). The existence of a Jupiter core is highly debated, but the calculations by Anic et al. (2007) show that the results of their simulations will be insensitive to the presence or absence, as well as nature of a planet core. They therefore only modeled it with the simple Tillotson EOS (Melosh 1989) assuming to consist of purely magmatic material. They found evidence for faint IR afterglows that could last from 10^6 yrs to 10^8 yrs depending on the age of the Jupiter planet. Anic et al. (2007) determined that the collision induce a $\sim 50\%$ increase in luminosity which should be observable, and it will be an important confirmation to find evidence for these events.

Marcus et al. (2009) studied collisions between terrestrial planets with masses ranging between 1 to 10 $M_{\rm Earth}$ and high velocities ranging up to approximately five times the mutual escape velocity $V_{\rm esc}$. The outcome of the collisions rely upon the impact velocity, mass ratio and impact angle of the collision. Depending on these properties, mergers, disruptions or grazing collisions occur. For mergers, the collision energies are small enough for the objects to become bound and merge into a single object with some mass loss. Disruptions may lead to changes in density of the outer layers of either object, which can be observed (Mercury was previously briefly mentioned as an example). With their results, Marcus et al. (2009) tried to determine the boundary between disrupting and grazing hits, based on the collisional parameters. This may allow for constraints to be put on the dynamical history of the observed systems, by determining whether they have evolved through collisions

or from a protoplanetary discs with substantially different composition.

No similar work has been done to determine the boundary between disrupting and grazing hits based on the collisional parameters, for Jupiter-massed objects. Collisions between gas giant planets have not been studied extensively and we lack statistics on the range of collisions; planet disruption, erosion, mass transfer and mergers.

In this project, we have therefore chosen to investigate the outcomes of collisions for a range of periapsides, mass fractions and relative initial velocities involving Jupiter-like planets. Several of the massive planets observed today may have been built up via collisions involving lower-mass planets. It therefore is important to know what types of collisions are possible and whether the planets can merge with little mass loss.

The remainder of the report is divided into four sections. In Section 2, modeling of planets is discussed and models are compared to known data from the Sun and Jupiter. Using polytropic models, properties such as pressure, density and temperature can be generated. The model profiles can then be used to initiate the numerical simulations of the collisions. This is covered in Section 3. Smooth particle hydrodynamics (SPH) is used for the simulations and has the advantage of being fast and handle the violent changes in structure that arise due to collisions. In Section 4 the method used to analyze the post-collision results is discussed. The aim of this is to determine the fraction of material bound to each planet remnant after the collision, and whether they are bound in an orbit, destined for a second collision.

Initial conditions for the simulations are discussed in Section 5, and the N-body integration package MERCURY from Chambers (1999) has been used to determine ranges of initial properties for the collisions. Using MERCURY, planetary systems are initiated with setups chosen to quickly become unstable, and information is gathered on the close encounters that occur within the integration time. At the end of the section, tables of parameters of interest are listed. The results of the collisions are presented in Section 6 and implications of these are discussed, with a final aim to study the statistics on planetary collisions involving mergers and mass loss.

2 Planet modeling

Planets are large concentrations of material that have accreted enough mass to become self-gravitating objects but not enough to ignite nuclear fusion. Two basic forces are at work; gravity, which is directed inwards, and pressure outwards. Without the pressure exerting a force outwards and balancing the compression due to gravity, the planet would collapse.

Through theoretical research as well as observational studies, we have learnt a lot about the interiors of stars. Planets are more difficult to study due to a higher opacity compared to stars, which causes transportation of photons to be inefficiently. Jupiter-like planets are observed to have a significant outer atmosphere, but there is some evidence for a solid structure in the interior for which much debate is still

ongoing as to the presence of a solid core (Fortney & Nettelmann 2009).

Analytical models can be derived for expressing the structure of planets. However, due to lack of information on the structures a few assumptions are first needed. In the following sections the structure equations are derived, which specify the change in the different properties mass, pressure, temperature and luminosity as a function of the radius r. Temperature and luminosity will not affect the outcomes of the collisions, but derivation for the temperature equation will be discussed briefly as it will be used later in Section 2.5 to compare accuracy of the planet models.

2.1 Structure equations

Many properties of an object can be derived using simple methods. The structure equations are sets of differential equations, which describe four main properties throughout the object's structure; mass, pressure temperature and luminosity. The four structure equations are derived for spherically symmetric stars, but are applicable to planet models as well.

Consider first a thin shell of the object, located a distance r from the core and with a thickness dr. As dr is considered very small, the area of the shell in the upper and lower faces can be treated as the same, $dA(r + dr) = dA(r)$. The volume of the shell will be $dV = 4\pi r^2 dr$, and with a density $\rho(r)$ the mass of the shell can be calculated. By rearranging the expression for the mass dM of this thin shell, the expression for change in mass as a function of the radius is derived:

$$\begin{aligned} dM(r) = \rho(r)dV &= 4\pi r^2 \rho(r) dr \\ \frac{dM(r)}{dr} &= 4\pi r^2 \rho(r) \end{aligned} \tag{2.1}$$

This is the first structure equation, also known as the equation of mass conservation. Since the object is considered to be spherically symmetric, we can consider forces only in the radial direction, as the tangential directions will cancel each other out. The thin shell will be subject to an expansive force, $|\boldsymbol{F}_{\text{exp}}|$, from the pressure $P(r)$ exerting a force on its lower face:

$$|\boldsymbol{F}_{\text{exp}}| = P(r)dA \tag{2.2}$$

The pressure of material residing outside of the radius $r+dr$, will exert a compressive force on the upper face of the mass element together with the gravitational force as:

$$|\boldsymbol{F}_{\text{con}}| = P(r + dr)dA + \frac{GM(r)}{r^2} dM \tag{2.3}$$

The two forces in Eq. (2.2) and Eq. (2.3) will in the case of hydrostatic equilibrium be balanced. Rewriting the change in mass $dM = \rho(r)dAdr$ and rearranging the expression one arrives at:

$$\begin{aligned} P(r)dA &= P(r + dr)dA + \frac{GM(r)}{r^2} \rho(r) dAdr \\ -\frac{GM(r)}{r^2} \rho(r) &= \frac{P(r + dr) - P(r)}{dr} \end{aligned} \tag{2.4}$$

This relates the density and gravitational force to the difference between the pressure force exerted at the upper and lower face of the shell. Now consider the thickness dr of the thin shell approaching zero ($dr \to 0$), for which the definition of a derivative gives:

$$\frac{dP(r)}{dr} = \frac{P(r+dr) - P(r)}{dr} \tag{2.5}$$

Together with Eq. (2.4), the equation of hydrostatic equilibrium is derived, which describes the change in pressure relative to the radius:

$$\frac{dP(r)}{dr} = -\frac{GM(r)\rho(r)}{r^2} \tag{2.6}$$

Three basic properties of the pressure's behavior as a function of radius is known for planets. (1) At the core, ($r = 0$), the pressure gradient will go to zero and the pressure reaches its maximum value. (2) At the surface $r = R$ it will drop to zero. (3) It will decrease outwards from the core toward the surface. Using the equation of hydrostatic equilibrium a helpful expression can be derived that relates density to radius (Prialnik 2010). Multiplying Eq. (2.6) by r^2/ρ, then differentiating with respect to r:

$$\frac{d}{dr}\left(\frac{r^2}{\rho(r)}\frac{dP(r)}{dr}\right) = -G\frac{dM(r)}{dr} \tag{2.7}$$

Inserting Eq. (2.1), the equation of mass conservation, into the right-hand side of Eq. (2.7), and rearranging gives:

$$\frac{1}{r^2}\frac{d}{dr}\left(\frac{r^2}{\rho(r)}\frac{dP(r)}{dr}\right) = -4\pi G\rho(r) \tag{2.8}$$

This is a second-order non-linear differential equation, that relates the density ρ to the radius r. This equation will be discussed more in the next section. There are two more structure equations, but which are not very important for our planet modeling. Temperature will be discussed briefly below as it will be used for model comparison later in Section 2.5, but for the luminosity readers are referred to Prialnik (2010) for further information.

The structure equation for temperature determines the change in temperature as a function of radius r and is derived from the equation for luminosity as a function of radius, $L(r) = \Phi dA$ where dA is the targeted area and Φ is the flux also expressed as $\Phi = \sigma T^4$, with σ being the Stefan-Boltzmann constant and T the temperature. Using this Prialnik (2010) derived an expression for the temperature gradient as:

$$\frac{dT}{dr} = -\frac{3\rho\kappa_r}{64\pi r^2\sigma T^3}L(r) \tag{2.9}$$

where κ_r is the Rosseland mean opacity. This equation, also called the equation for thermal equilibrium, in Eq. 2.9 is supplemented by a relation that relates the temperature and density to the pressure as:

$$P = \frac{\Re}{\mu}\rho T + P_e + \frac{1}{3}\alpha T^4 \tag{2.10}$$

where $\Re$ is the gas constant, μ the mean atomic mass and the P_e the electron degeneracy pressure. $\alpha = 4\sigma/c$ is the radiation constant, related to the total energy radiation by a blackbody, with c being the speed of light. The structure equations needed for defining the planet model are now given. However, without any further assumptions these cannot be integrated to find the profile of pressure, mass, temperature and luminosity. This is mainly due to three reasons. (1) The equations are non-linear. (2) All of the structure equations are coupled by the dependence of pressure on temperature, which means they have to be solved simultaneously. (3) The equations have two-point boundaries for the surface and core. This requires the structure equations to be solved by iterative numerical methods (Prialnik 2010). In the next section we discuss polytropic models which, upon implementation, allows us to extract some information on the structure of the object.

2.2 Polytropes

The difficulty of solving the structure equations comes from the fact that the first pair of equations (mass and pressure) are linked to the second pair of equations (temperature and luminosity), through the dependence of pressure on temperature. Had we simply had a relation between pressure and density, the equations for mass and pressure could be solved separately. This would be equivalent to a hydrostatic configuration being independent of the flow of heat through it. Analytical solutions for analyzing the structure of objects have been known for more than a century.

Polytropic models rely on a simple expression between pressure and density. Collins (1989) derived such a relation between pressure and density using basic thermodynamics. By considering the change in heat of a gas, and using the ideal gas law, he defined a polytropic gamma:

$$\gamma = \frac{C_{\mathrm{P}} - C}{C_{\mathrm{V}} - C} \tag{2.11}$$

where C_{P} is the specific heat at a constant pressure, C_{V} the same for a constant volume and C the actual specific heat. This γ is often used to define another constant, known as the polytropic index n which determines the structure of the object and is specific for different types of object:

$$n = 1/\left(\gamma - 1\right) \tag{2.12}$$

Using this, Collins (1989) defined the relation between pressure and density in its traditional form for polytropic models:

$$P = K\rho^{\gamma} = K\rho^{(n+1)/n} \tag{2.13}$$

where K is a constant, related to the mass of the object. This polytropic equation provides us with a very basic relation between the pressure and density, which can be used to extract information regarding the object's structure. Inserting the polytropic

equation in Eq. (2.13) into Eq. (2.8) to eliminate the pressure P and using the chain rule Prialnik (2010) derived the expression:

$$\frac{(n+1)K}{4\pi G n}\frac{1}{r^2}\frac{d}{dr}\left(\frac{r^2}{\rho^{n-1/n}}\frac{d\rho}{dr}\right) = -\rho \tag{2.14}$$

which is another form of Eq. (2.8). The solution to this equation for $\rho(r)$ defined in the radius $0 \leq r \leq R$ is named a polytrope. In order to find the solution it is convenient to define a dimensionless density variable θ in the range $0 \leq \theta \leq 1$, such that:

$$\rho = \rho_{\mathrm{c}}\theta^n(\xi) \tag{2.15}$$

is valid for the dimensionless radius ξ defined as:

$$\xi = r/a \tag{2.16}$$

where a can, for convenience, be chosen to include the constants of Eq. (2.14):

$$a^2 = \frac{(1+n)K}{4\pi G\rho_{\mathrm{c}}^{(n-1)/n}} \tag{2.17}$$

Inserting Eq. (2.15) and Eq. (2.16) into Eq. (2.14) we arrive at the Lane-Emden equation:

$$\frac{1}{\xi^2}\frac{d}{d\xi}\left(\xi^2\frac{d\theta}{d\xi}\right) = -\theta^n \tag{2.18}$$

It has two known boundary conditions:

$$\theta(0) = 1 \tag{2.19}$$

$$\frac{d\theta}{d\xi}_{\xi=0} = 0 \tag{2.20}$$

The first condition in Eq. (2.19) comes from the fact that the potential θ will go to unity as ξ goes toward zero, in which Eq. (2.15) will give the core density. The second condition in Eq. (2.20) comes from the equation of hydrostatic equilibrium, which states that the pressure gradient is zero at the center, meaning θ has its maximum value at this point. The solution to the Lane-Emden equation gives the profile of the dimensionless density variable θ, and from which the density profile can be determined through Eq. (2.15).

The Lane-Emden equation is only analytically solveable for a few specific polytropic indices $n = 0, 1, 5$, and needs to be solved numerically for other n. More on numerically solving the Lane-Emden equation is discussed in Section 2.4.

In Figure 1 the solutions to the Lane-Emden equation are plotted for different polytropic indices $n = 1, 2, 3, 4$, with both θ and ξ normalized to unity. $n = 1$ results in the most uniform distribution, and $n = 4$ the least. The mass of the object also becomes more concentrated towards the central regions for lower polytropic indices. The mass distribution of planets are more uniform than stars, so it will require a

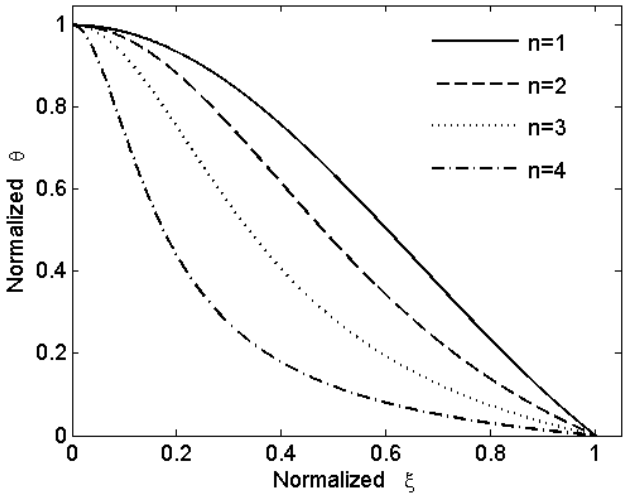

Figure 1: Solutions to Lane-Emden Equation for different polytropic indices $n = 1, 2, 3, 4$.

lower polytropic index. Before we venture deeper into the types of objects described by different polytropic indices n, we will look at how we can use the assumptions made so far to determine the properties of the polytropic models as a function of the polytropic index n.

2.3 Properties of polytropic models

The polytrope equation gives a basic relation between pressure and density, which can be used to derive the properties of the polytropic model. The enclosed mass inside a radius r' is computed by integrating over the radius of the object:

$$M(r') = \int_0^{r'} \rho dV = 4\pi \int_0^{r'} r^2 \rho dr \tag{2.21}$$

The enclosed mass is incorporated into the polytropic model by inserting the density from Eq. (2.15) and radius of Eq. (2.16). This gives an expression to determine the enclose mass of an object of radius ξ':

$$M(\xi') = 4\pi a^3 \rho_c \int_0^{\xi'} \xi^2 \theta^n d\xi \tag{2.22}$$

where ξ' is the dimensionless equivalent of the radius r'. The integral can be replaced by rearranging Eq. (2.18) to solve for $\xi^2\theta^n$, and the resulting expression integrated:

$$\begin{aligned} M(\xi') &= -4\pi a^3 \rho_c \int_0^{\xi'} \frac{d}{d\xi}\left(\xi^2 \frac{d\theta}{d\xi}\right) d\xi \\ &= -4\pi a^3 \rho_c \left[\xi^2 \frac{d\theta}{d\xi}\right]_0^{\xi'} + C_1 \end{aligned}$$

where $d\theta/d\xi|_{\xi'}$ is the derivative of θ at the point ξ'. The integration constant can be solved with the boundary condition $M(0) = 0$, resulting in an integration constant $C_1 = 0$, in which the expression become:

$$M(\xi_R) = -4\pi a^3 \rho_c \, \xi_R^2 \frac{d\theta}{d\xi}\bigg|_{\xi_R} \tag{2.23}$$

which determines the enclosed mass at the radius where $\xi' = \xi_R$, which is the dimensionless radius equivalent to the planet radius R. The density, and hence core density according to Eq. (2.15), affects all properties governed by the structure equations discussed in Section 2.1. Evidently the core density is an important property of the model. The mean density is a property that can easily be determined if one knows the mass and radius of the modeled object, and finding a relation between the mean and core density will allow to determine the core density of the model. Rewriting Eq. (2.16) as $a = R/\xi_R$, and inserting this into Eq. (2.23) gives:

$$M(\xi_R) \;=\; -4\pi \frac{R^3}{\xi_R^3} \xi_R^2 \rho_c \, \frac{d\theta}{d\xi}\bigg|_{\xi_R}$$

A planet's mean density is determined by the mass divided by its volume, $\bar{\rho} = M/V$, with the volume $V = \frac{4}{3}\pi R^3$. Using this, an expression relating the core and mean density of the object is found:

$$\begin{aligned} M(\xi_R) &= -V \frac{3}{\xi_R} \rho_c \, \frac{d\theta}{d\xi}\bigg|_{\xi_R} \\ \rho_c &= -\bar{\rho} \left[\frac{3}{\xi_R} \, \frac{d\theta}{d\xi}\bigg|_{\xi_R} \right]^{-1} \end{aligned} \tag{2.24}$$

Since the relation is derived from the solutions of the Lane-Emden equation, it will be dependent on the polytropic index n. Hence the core density will depend on the type of objects modeled, which is expected as the polytropic index determines how centrally concentrated a model is according to Eq. (2.15).

An expression for the constant K is needed to determine the pressure according to Eq. (2.13). If Eq. (2.13) is solved for the constant K, and the central pressure and density is considered, K can be determined as:

$$K = P_c/\rho_c^{1+1/n} \tag{2.25}$$

The core density is determined using the mean density in Eq. (2.24). Prialnik (2010) derived an expression for the central pressure, which is related to the mass and radius of the object as:

$$P_c = \frac{M^2 G}{R^4} \left[4\pi(n+1) \, \frac{d\theta}{d\xi}\bigg|_{\xi_R} \right]^{-1} \tag{2.26}$$

The two essential properties of the planet model can now be determined using Eq. (2.13) for the pressure, and Eq. (2.15) for the density. Temperature is of no

interest for the planet models, as they will not affect the investigated results of the collisions. Expressions for calculating the temperature is given in Eq (2.27) below and the reader is referred to G. P. Horedt (2004), who derived these expressions, for further information.

$$T(\xi) = T_c\theta(\xi) = \frac{K\mu\rho_c^{1/n}}{\Re}\theta(\xi) = \frac{\mu P_c}{\Re\rho_c}\theta(\xi) \tag{2.27}$$

where $\Re$ is the gas constant and μ the mean molecular weight. The tools needed to generate a planet model have now been presented. In the next section we look closer into the Lane-Emden equation and how to numerically solve it and how the method was implemented in the program, LEQ, which has been used to generate the planet models for this project. After this we discuss the polytropic index in more detail, and end the section with an analysis of the program, comparing the output to known data of two familiar objects: the Sun and Jupiter.

2.4 Numerical solution of Lane-Emden equation

The Lane-Emden equation discussed in Section 2.2 only has analytical solutions for a few polytropic indices, so a numerical approach for solving the equation is needed in order to generate the planet models. The profile of the function $\theta(\xi)$ is essential, as it determines the overall structure of the model, and specifically the boundary point ξ where $\theta(\xi) = 0$ needs to be determined.

The solution to $\theta(\xi)$ may show harmonic behavior for some n and give several solutions ξ. The first solution will only be of interest, as this determines the radius of the model in terms of the dimensionless radius ξ. The Lane-Emden equation can be rewritten to solve for the second derivative of the $\theta(\xi)$ function:

$$\begin{aligned}\frac{1}{\xi^2}\frac{d\theta}{d\xi}\left(\xi^2\frac{d\theta}{d\xi}\right) &= \frac{1}{\xi^2}\left(2\xi\frac{d\theta}{d\xi} + \xi^2\frac{d^2\theta}{d\xi^2}\right) \\ &= \frac{2}{\xi}\frac{d\theta}{d\xi} + \frac{d^2\theta}{d\xi^2} = -\theta^n\end{aligned}$$

Rewriting this for the second derivative of θ with respect to ξ gives:

$$\frac{d^2\theta}{d\xi^2} = -\left(\frac{2}{\xi}\frac{d\theta}{d\xi} + \theta^n\right) \tag{2.28}$$

where θ is the dimensionless density function, and ξ the dimensionless radius. Using the boundary conditions $\theta(0) = 1$ and $\left.\frac{d\theta}{d\xi}\right|_{\xi=0} = 0$, one would stepwise calculate θ using its first and second derivative, $d\theta/d\xi$ and $d^2\theta/d\xi^2$ respectively. First, the change in the first derivative of θ is computed between radii ξ_j and ξ_k using Eq. (2.28), with $j = 1, 2, 3....N-1$ and $k = j+1, j+2, j+3....N$ where N is the total number of steps. The new $d\theta/d\xi$ is computed as:

$$\left.\frac{d\theta}{d\xi}\right|_k = \left.\frac{d\theta}{d\xi}\right|_j - \left[\frac{2}{\xi}\left.\frac{d\theta}{d\xi}\right|_j + \theta_j^n\right] d\xi \tag{2.29}$$

In this way we can use a step of $d\xi$ to calculate the first derivative of θ, and with a smaller $d\xi$ the precision will increase, although the computing time will increase. Using the updated first derivative of θ_j one can update θ_k as:

$$\theta_k = \theta_j + \left.\frac{d\theta}{d\xi}\right|_k d\xi \tag{2.30}$$

Updating both $d\theta/d\xi$ and θ towards the boundary $\theta \leq 0$, the profile of the θ function can be computed. A simple interpolation between the two points surrounding the boundary $\theta = 0$ will yield ξ_R, the dimensionless radius equal to the full radius of the model according to Eq. (2.16).

Hence the profile of θ can be calculated, and then used to estimate the properties of our models with the equations derived in Section 2.3. For generating model profiles, a program in Fortran called LEQ has been written. The program code for LEQ is found in Appendix B, and a description and manual for its use is found in Appendix A.3.

2.5 Polytropic models

The polytropic index n is the most important property of the planet models as it determines the type of object and will be discussed further in this section. Mass of the modeled planet also need to be specified, and the radius can be determined by using a mass-radius relation, and these will allow the mean density to be solved for together with the remaining properties of the model.

Polytropic models are applicable to a wide range of astrophysical objects, and can with at least a reasonable precision describe their internal structure. Different types of object have different structures. Stars have, for example, more of its mass centrally concentrated than planets, which as a more uniform distribution of their mass. It is the polytropic index n which determines the slope of the dimensionless gravitational potential θ, allowing different types of structures to be modeled.

A program written in FORTRAN, that implements the polytropic models and the equations derived and discussed previously. It is used to generate the planet models for this project and requires inputs for the polytropic index n and mass M of the model, and solves the Lane-Emden equation numerically. The program is called LEQ and more information can be found in the program manual in Appendix A and the code is given in Appendix B. The generated model output of the program was tested against two familiar objects of our solar system; the Sun and Jupiter, and the results of these comparisons will be discussed separately.

Our Sun is the most well studied stellar object and its structure well known, making it a good test for our polytropic program. The Standard Solar Model (SSM) is considered to be very successful and summarizes our current knowledge of the Sun. Comparing this model to a polytropic model with a polytropic index chosen to represent the Sun, we do a first test of our program. The best choice of polytropic index according to Geroyannis (1993), is $n = 3.23$. In Table 1 are the listed properties

of our polytropic model together with the equivalent values from the SSM by Bahcall (2005).

Model	ρ_c [g cm^{-3}]	T_c [K]	P_c [Pa]
Polytropic	105	1.2×10^7	1.3×10^{16}
SSM	150	1.6×10^7	2.3×10^{16}

Table 1: Comparison between polytropic model and the SSM of Bahcall (2005) for central density, temperature and pressure of the Sun.

Considering the simple approximation used, the data samples fit very well. This was a basic test for our model, but we also need to do a comparison to data for Jupiter which will be used in our collisions. Orbiting our Sun with a semi-major axis of 5.2 au, studies of Jupiter are more difficult than observing the Sun. This has yielded significantly less well constrained understanding of the interior of the largest planet in our solar system. Constraints are found by determining properties of the planet such as mass, radius, gravitational moments as well as compositional estimations.

The model of Guillot (1999) collected observational data of gas giants into a basic three-layered model. Further constraints on the model are provided from evolutionary data on the models, since these should yield ages comparable to the planets and the Solar system. The model also takes into account uncertainties in the measurements, including that for the equation of state, opacities and surface temperature. In the model they could derive estimates of the core properties of pressure and temperature for their Jupiter model, these properties are listed in Table 2 below.

Observations have allowed for the mass and radius of Jupiter to be determined with good precision. In this project, planets with larger masses than that of Jupiter will be modeled and used in the collisions. Chabrier et al. (2009) discuss the mass-to-radius relationship ranging from planets up to stars and suitable polytropic indices for these objects. While solar-like stars are modeled well by a polytropic index of $n \approx 3$, low-mass stars are characterized by a polytropic index $n \approx 3/2$. This decrease of the polytropic index continues with lower-mass objects, down to $n = 1$ for Jupiter-like planets and $n < 1$ for terrestrial planets. A polytropic index of $n = 1$ was also determined by Bobrov et al. (1978) from observational data.

In Figure 2 the mass-radius relation for objects ranging in mass from Jupiter-like planets up to solar-like objects has been plotted. With the polytropic indices for each object type. Three different isochrone models are shown in the figure, with 10 Gyr, 5 Gyr and 1 Gyr from top to bottom. From the low-mass star objects to Jupiter-like planets, the polytropic index drops from $n \approx 1.5$ to $n \approx 1$. This is caused by the (classical) electrostatic contribution from the ions becoming comparable to the (quantum) electrons as the density decreases with the mass, causing the mass-radius relation to flatten (Chabrier et al. 2009). Specifically, for Jupiter-like planets, as modeled in this project, a suitable polytropic index is $n = 1$ (Chabrier et al. 2009).

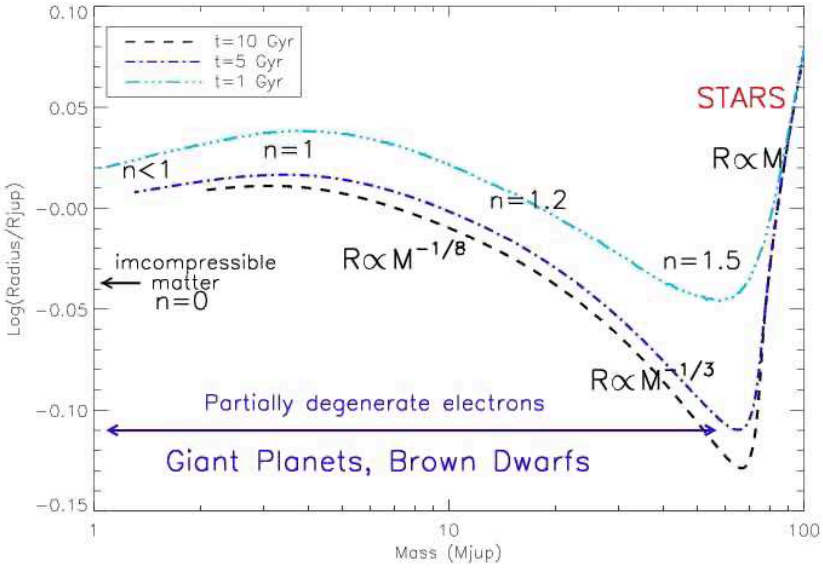

Figure 2: Mass-radius relationship from Jupiter-like planets to Solar-like stars for three different isochrones, with characteristic polytropic indices for each region indicated. Figure take from Chabrier et al. (2009).

For Jupiter-like planets Chabrier et al. (2009) determine that the radius scale to mass as $R \propto M^{-1/8}$. This means that the radius will slowly change with mass. Using Jupiter as standard, the radius is scaled with mass accordingly to this relation for the models generated in this project. It is however important to test the models with accurate estimates on the properties of Jupiter, comparing theoretical model based on observations with a polytropic model with polytropic index $n = 1$.

The central properties of the density, pressure and temperature determined through a polytropic model are listed in Table 2 below, together with the model data of Bahcall (2005). The core density is not available from the model of Bahcall (2005), but it should lie in between the value of Earth and the Sun, so an estimation is used for comparison, marked by a parenthesis for the Guillot model.

Model	ρ_c [g cm^{-3}]	T_c [K]	P_c [Pa]
Polytropic	4.64	2.37×10^5	3.62×10^{13}
Guillot (1999)	(10 - 150)	$1.50 - 2.1 \times 10^4$	4.00×10^{12}

Table 2: Jupiter model comparison between core properties of our polytropic model and the model of Guillot (1999).

The discrepancy is large for both the temperature and central density, where the polytropic model is approximately one order of magnitude larger than the values of the Guillot model. The discrepancy in temperture will not affect our collisions as

the collisional affect on temperature is not considered. Due to the complexity of modeling Jupiter from the limit available data on its properties, it is still uncertain how accurate the model of Guillot (1999) is. The core density of the polytropic model is however significantly lower than the expected range for a Jupiter planet. This disagreement can be traced back to the discussion on whether Jupiter has a core or not. Fortney & Nettelmann (2009) collected results of the determination of Jupiter's core mass since the early 1970's, showing large scatters in the results as recently as 2009, lying somewhere around $0 - 7$ M_{Earth}, consisting of a mix of ice and rock. Considering a core in the model would require a two-phased polytropic model of different polytropic indices, as the core would not follow the model profile of the outer parts of the planet. However, Anic et al. (2007) performed a number of collisions between Jupiter-like planets and Earth-sized projectiles and found that the existence of a core had quite a small effect on the results. It is uncertain if this would hold for collisions between two Jupiter-like planets as well. The presence of a core is disregarded in this project and the polytropic models are only generated by one single polytropic index. It would however be of interest to investigate the effect of a core to the results of the collisions in the future.

Using the model profile generated by the LEQ program, collisions between planets can be modeled using a hydrodynamical method, and in the next section this method is presented and discussed.

3 Smoothed particle hydrodynamics

Observations of the universe and its astrophysical phenomena imply that hydrodynamical flow and orbital mechanics are those most vital in order to model and understand its behavior. Much of what we observe in the Universe has been formed through combinations of gravity, gas dynamics and additional physical processes. However, the complexity of the involved physical processes and the lack of symmetry usually prohibit analytical treatment. Hence numerical simulations are an increasingly important method to reproduce the behavior of complex systems.

Over the years, numerous different methods for numerical simulations have been developed with different approaches to the problem. The design of the numerical method needs to fulfill several requirements to be applicable to the wide range of problems studied within astrophysics. Shocks and large releases of energy cause rapid and extreme changes in structure that can pose problems for some methods. The choice of numerical method can have a significant impact on results for certain problems.

Smoothed Particle Hydrodynamics (SPH) is used in a wide range of scientific fields including astrophysics, ballistics, vulcanology, oceanology. It was initially introduced by Lucy (1977) and Gingold & Monaghan (1977) and was developed in an attempt to avoid the limitations of present methods for modeling continuum physics.

There are two main types of numerical methods; Eulerian and Lagrangian, which handle materials in different ways. The Eulerian description considers the flow of

fluid through specific locations and tracks the change in mass, momentum and energy. This makes it difficult to track a specific point attached to the material with time. The Lagrangian description instead uses a material description which the tracks changes of fixed volumes of material.

The differences between these methods can be illustrated by an example of observing the flow of a river. In the Eulerian description, the observer would be sitting on the river bed and watch the water flow. An Lagrangian observer would however sit in the river, and move with the flow of the water. This is the difference between the methods; the Eulerian description has a static observer while the Lagrangian has an observer in motion with the material.

Implementation of either Eulerian or Lagrangian methods has its own drawbacks and advantages. The two numerical methods can be applied to grid-based numerical methods, where the spatial domain is divided up into a number of grids in which the evolution of the material is tracked.

In Eulerian grid-based methods the flow of fluid through specific locations considered, and the change in mass, momentum and energy is tracked with time. This makes it difficult to track a specific point in the material. Due to the implementation of a static grid, it is not suitable for simulating large deformations, inhomogeneities as well as simulating discrete particles rather than continuum problems. A good example of the latter involves simulating the movement of a large quantity of particles in a stellar cluster.

For the Lagrangian method, the grid is instead attached to specific points of the material and hence, opposite to the Eulerian description, it can easily obtain the time history for a point attached to it but large deformations can be difficult to handle. The Lagrangian description is more suitable for problems in astronomy and astrophysics.

SPH belongs to a group of numerical methods called meshfree methods, which are more flexible and can replace the grids. It was developed in response to the increasing demand to handle large deformations, complex geometries, discontinuities and singularities. The grid-based methods relied on a rigid grid or mesh for calculations while meshfree methods use a set of arbitrarily distributed particles (or nodes) without any mesh to connect the particles.

SPH is a Lagrangian, particle meshfree methods, where a finite number of particles represent the state of the system and the motion of the system is simulated. Its main advantage over the grid-based methods is its simplicity, adaptively, ease to visualize and analyze results and it is boundary free.

In SPH, the particles have a set of field variables describing mass, momentum, energy and position. Particles also have a property called the smoothing length, which defines their support domain. Properties of each particle are affected by neighboring particles, and computed as a weighted sum of particles inside the support domain. At each new time step, the support domain of every particle is re-evaluated to adjust for the current distribution of particles. Using sufficient particles, this method can attain high precision with good energy conservation while remaining applicable to a wide range of different simulations. In the next two section we

discuss the two approximations that the SPH formalism is based on; the Kernel approximation and the Particle approximation.

3.1 Kernel approximation

In SPH the properties are estimated at any point $\boldsymbol{r}$ by taking the weighted average of particle properties inside a certain volume. To determine this a general field function A($\boldsymbol{r}$) is considered, which may represent any of the field variables defined at the position $\boldsymbol{r}$, such as velocity or density. Convolution of the field variable and a Dirac delta function δ, gives the field function at a point $\boldsymbol{r}$:

$$A(\boldsymbol{r}) = \int_{\Omega} A(\boldsymbol{r}')\delta\left(\boldsymbol{r} - \boldsymbol{r}'\right) d\boldsymbol{r}' \tag{3.1}$$

where Ω is the volume over which the field function is defined. For SPH the Dirac delta function is substituted by a smoothing kernel function $W(\boldsymbol{r} - \boldsymbol{r}', h)$, with a characteristic width h. This is the kernel approximation. The smoothing kernel function W can have different shapes depending on its use, and needs to satisfy a number of conditions such as the normalization condition:

$$\int_{\Omega} W(\boldsymbol{r} - \boldsymbol{r}', h)d\boldsymbol{r}' = 1 \tag{3.2}$$

and as the smoothing length h goes to zero, the smoothing function will again take the form of a Dirac delta function:

$$\lim_{h\to 0} W(\boldsymbol{r} - \boldsymbol{r}', h) = \delta(\boldsymbol{r} - \boldsymbol{r}') \tag{3.3}$$

The third condition is that the smoothing function should be zero outside of its defined radius h:

$$W(\boldsymbol{r} - \boldsymbol{r}', h) = 0 \qquad \text{, when } \ |\boldsymbol{r} - \boldsymbol{r}'| > \kappa h \tag{3.4}$$

where κ is a constant related to the smoothing function and define its effective radius. The shape of the smoothing function used for this project will be discussed in Section 3.4.6. Substituting the smoothing function $W(\boldsymbol{r} - \boldsymbol{r}', h)$ for the Dirac delta function δ, Eq. (3.1) becomes:

$$\langle A(\boldsymbol{r})\rangle = \int_{\Omega} A(\boldsymbol{r}')W\left(\boldsymbol{r} - \boldsymbol{r}', h\right) d\boldsymbol{r}' \tag{3.5}$$

The smoothing function in Eq. (3.1) is denoted as $\langle A(\boldsymbol{r})\rangle$, meaning an approximation is being used. By expanding $A(\boldsymbol{r})$ around $\boldsymbol{r}$ as a Taylor series, the accuracy of the approximation can be determined.

$$\begin{aligned}
\langle A(\boldsymbol{r})\rangle &= \int_{\Omega} A(\boldsymbol{r}')W\left(\boldsymbol{r} - \boldsymbol{r}', h\right) d\boldsymbol{r}' \\
&= A(\boldsymbol{r}) \int_{\Omega} W(\boldsymbol{r} - \boldsymbol{r}', h)d\boldsymbol{r} + \nabla A(\boldsymbol{r}) \int_{\Omega} (\boldsymbol{r}' - \boldsymbol{r})W(\boldsymbol{r} - \boldsymbol{r}', h)d\boldsymbol{r}' \\
&+ O(h^2)
\end{aligned} \tag{3.6}$$

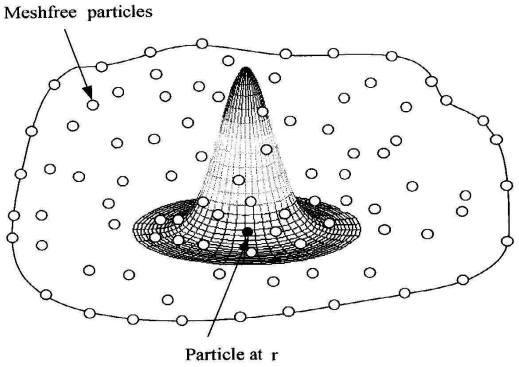

Figure 3: Illustrating the smoothing function used in SPH, taken from (Liu & Liu 2007).

where $O(h^2)$ are higher-order residuals. For an even function W, the integral of the second term in Eq. (3.6) will be zero:

$$\int_\Omega (\boldsymbol{r}' - \boldsymbol{r}) W(\boldsymbol{r} - \boldsymbol{r}', h) d\boldsymbol{r}' = 0$$

Thus for an even W, the value of the field function $A(\boldsymbol{r})$ can be approximated using the kernel approximation as:

$$\langle A(\boldsymbol{r}) \rangle = \int_\Omega A(\boldsymbol{r}') W\left(\boldsymbol{r} - \boldsymbol{r}', h\right) d\boldsymbol{r}' + O(h^2) \tag{3.7}$$

where the residuals $O(h^2)$ of second order for the kernel approximation are neglected. Therefore the kernel approximation is accurate to second order. In the next section the spatial derivative of $\langle A(\boldsymbol{r}) \rangle$ is derived.

3.2 Spatial derivative

The spacial derivative of the same field function $A(\boldsymbol{r})$ can be derived by replacing $A(\boldsymbol{r})$ with $\nabla A(\boldsymbol{r})$ in Eq. (3.5). In this way an approximation of the spatial derivative $\nabla A(\boldsymbol{r})$ can be obtained as:

$$\langle \nabla A(\boldsymbol{r}) \rangle = \int \nabla A(\boldsymbol{r}') W\left(\boldsymbol{r} - \boldsymbol{r}', h\right) d\boldsymbol{r}' \tag{3.8}$$

Using the product rule, and the divergence theorem, that transforms a volume integral into a surface integral, the expression can be rewritten as as (Liu & Liu 2007):

$$\langle \nabla A(\boldsymbol{r}) \rangle = \int_S A(\boldsymbol{r}') W(\boldsymbol{r} - \boldsymbol{r}', h) \cdot \boldsymbol{n} dS - \int_\Omega A(\boldsymbol{r}') \nabla W(\boldsymbol{r} - \boldsymbol{r}', h) d\boldsymbol{r}' \tag{3.9}$$

where $\boldsymbol{n}$ is the unit vector normal to the unit surface. The compact condition in Eq. (3.4) implies that the smoothing function will be zero outside of the defined

radius κh. Due to this boundary, the surface integral in Eq. (3.9) is zero and the final expression for the spatial derivative is:

$$\langle \nabla A(\boldsymbol{r}) \rangle = -\int_{\Omega} A(\boldsymbol{r}')\nabla W(\boldsymbol{r}-\boldsymbol{r}', h)d\boldsymbol{r}' \tag{3.10}$$

3.3 Particle approximation

As previously mentioned, SPH uses a finite number of particles to represent continuum problems, each possessing a number of field variables. This is where the particle approximation is applied, where Eqs. (3.5) and (3.10) are converted into equations involving summation over all the particles in the individual support domains of each particle. As the problem domain is converted into a finite number of particles, the expression for a specific point is converted $\boldsymbol{r}-\boldsymbol{r}' = \boldsymbol{r}_i - \boldsymbol{r}_j = \boldsymbol{r}_{ij}$ for the particles i and j, and the angled brackets are dropped.

To apply the particle approximation, the infinitesimal volume of $d\boldsymbol{r}'$ is replaced with the finite volume ΔV_j of particle j. This relates to the mass of the particle as:

$$m_j = \Delta V_j \rho_j \tag{3.11}$$

where m_j is the particle mass and ρ_j the density. In this way Eq. (3.5) and (3.10) can be rewritten in the particle approximation as:

$$\begin{aligned} A(\boldsymbol{r}_i) &= \sum_{j=1}^{N} A(\boldsymbol{r}_j)W(\boldsymbol{r}_{ij}, h)\Delta V_j \\ \nabla A(\boldsymbol{r}_i) &= -\sum_{j=1}^{N} A(\boldsymbol{r}_j)\nabla W(\boldsymbol{r}_{ij}, h)\Delta V_j \end{aligned} \tag{3.12}$$

where N is the total number of particles. The change in volume ΔV_j can be replaced by extending with ρ_j, giving $\rho_j \Delta V_j/\rho_j = m_j/\rho_j$. In this way the equation becomes:

$$A(\boldsymbol{r}_i) = \sum_{j=1}^{N} A(\boldsymbol{r}_j)W(\boldsymbol{r}_{ij}, h)\frac{m_j}{\rho_j} \tag{3.13}$$

The smoothing function W is important for SPH simulations, and its form can be selected to enhance its properties. This, along with a discussion on more properties of the code used in this project is discussed in the next section.

3.4 The Benz code

There are many different implementations of SPH code, which may vary in terms of time integration or kernel functions. In this project the code of Dale & Davies (2006) is used, which is a modified version of the Benz (1990) code. Two properties need to be conserved at all times during the simulations; the momentum and energy.

3.4.1 Physical fluid properties

In SPH the density and other properties of each particle are estimated as weighted sums of neighboring particles within a certain radius set by the smoothing length h. The smoothing length limits the number of particles which SPH uses to estimate the properties of each particle of, for example the density of a particle i is reduced to summing over the particle itself and its neighbors as:

$$\rho_i = m_i W(0, h) + \sum_{j=1}^{N} m_j W(\boldsymbol{r}_{ij}, h) \tag{3.14}$$

where N is the number of neighbors situated within a certain radius κh of particle i, where κ is a constant that defines the non-zero area of the smoothing function.

3.4.2 Momentum equation

The standard SPH formalism of momentum conservation is used in the code by Benz (1990). Initially a simple case is considered that does not take into account the contribution of viscosity or self-gravity, which will be discussed later, and the derived expression is:

$$\frac{d\mathbf{v}_i}{dt} = -\sum_{j=1}^{N} m_j \left(\frac{P_i}{\rho_i^2} + \frac{P_j}{\rho_j^2} \right) \nabla_i W\left(\boldsymbol{r}_{ij}, h\right) \tag{3.15}$$

where P_i is the pressure exerted on particle i and ρ_i the particle's density. Only particles for which $\nabla_i W\left(\boldsymbol{r}_{ij}, h\right)$ is non-negligible will contribute in the expression, which is consistent with pressure being a short-ranged force since only neighboring particles will have a significant contribution. The efficiency of SPH is limited by how quickly the neighboring particles can be found.

3.4.3 Energy conservation

In an isolated system the total energy should be conserved at all times. The first law of thermodynamics states that the energy change inside a volume should equal the summation of the net heat flux into the volume and the work done by body and surface forces exerted onto the volume.

Disregarding the contribution of viscosity and self-gravity, the expression for the energy conservation, as derived by Benz (1990), is:

$$\frac{du_i}{dt} = \frac{P_i}{\rho_i^2} \sum_{j=1}^{N} m_j \boldsymbol{v}_{ij} \nabla_i W(\boldsymbol{r}_{ij}, h) \tag{3.16}$$

where $u_i \equiv \langle u \rangle_i$ describes the smooth specific internal energy and $\boldsymbol{v}_{ij} = \boldsymbol{v}_i - \boldsymbol{v}_j$.

3.4.4 Artificial viscosity

During shocks, resulting from violent collisions, part of the kinetic energy is transformed into heat energy. By not taking this into account in the simulations this results in large, unphysical oscillations in the properties of the fluid after the collision. The solution is to add a term to handle this dissipation of kinetic energy into heat. Ordinarily two different types of viscosities are introduced in SPH, which can both be translated to artificial viscous pressure terms and combined into one single term. The viscosity is computed pair-wise between particle pairs i, j as:

$$\Pi_{ij} = \begin{cases} \frac{-\alpha c_{\rm s} \mu_{ij}}{\rho_{ij}} + \frac{\beta \mu_{ij}^2}{\rho_{ij}} & , \text{ if } \boldsymbol{v}_{ij} \cdot \boldsymbol{r}_{ij} \leq 0 \\ 0 & , \text{ if } \boldsymbol{v}_{ij} \cdot \boldsymbol{r}_{ij} > 0 \end{cases} \tag{3.17}$$

where α and β are free parameters, $c_{\rm s}$ is the speed of sound and l a typical length scale over which the shock is spread. In the code the free parameters have been set to typical values of $\alpha = 1$ and $\beta = 2$ (Bate 1995). The density $\rho_{ij} = 0.5(\rho_i + \rho_j)$ ensure that the viscosity is symmetric in i and j and hence that momentum is conserved. The term μ_{ij} is calculated as:

$$\mu_{ij} = \frac{h \boldsymbol{v}_{ij} \cdot \boldsymbol{r}_{ij}}{\boldsymbol{r}_{ij}^2 + \eta^2}$$

where the term $\eta^2 = 0.01h^2$ helps to avoid divergence for small separations between neighboring particles. The first term in Eq. (3.17) is the bulk viscosity, with a primary purpose to eliminate any subsonic velocity oscillations, while the second is the von Neumann-Richtmyer viscosity that handles high-Mach-number shocks, which is especially important for supersonic velocity oscillations.

3.4.5 Self-gravity

Self-gravity for astrophysical problems cannot be neglected, and expressions for their contribution needs to be added to Eq. (3.15). Starting with the Poisson equation, Benz (1990) derived the expression for determining the total gravitational force on a particle felt by all individual surrounding particles as:

$$-\nabla \phi_i = -G \sum_{j=1}^{N} \frac{M(\boldsymbol{r}_{ij})}{|\boldsymbol{r}_{ij}|^2} \frac{\boldsymbol{r}_{ij}}{|\boldsymbol{r}_{ij}|}$$

where $M(\boldsymbol{r}_{ij})$ is defined as:

$$M(\boldsymbol{r}_{ij}) = 4\pi \int_0^{\boldsymbol{r}_{ij}} \boldsymbol{r}^2 \rho(\boldsymbol{r}) d\boldsymbol{r}$$

As gravity is a long range force, it will not vanish at large particle separations, which means that gravity has to take into account all particles. The time needed for this at each time-step would scale as N^2, where N is the number of particles in the simulation, and this will cause problems for large numbers of particles. One

way to improve the efficiency of the gravity calculations without loosing too much precision is to implement the hierarchical tree method (Barnes & Hut 1986), and adapting it into SPH codes is easy (Hernquist & Katz 1989). Implementation allows the computation time to scale as $N\log N$, which is significant smaller for larger N. The method works such that for close neighbors to the current particle, the gravity is computed exactly, while distant particles are instead combined into simple aggregates.

3.4.6 The kernel function

Many different kernel functions have been proposed since the development of the SPH method. The code used by Benz (1990) diverged by having a compact support, meaning that it will only be valid within a certain interval. The kernel function is known as a B-spline function, and is the most widely used kernel function proposed by Monaghan & Lattanzio (1985), who defined it as:

$$W(r_i,h) = \frac{1}{\pi h^3}\begin{cases} 1-\frac{3}{2}\frac{|\boldsymbol{r}_{ij}|}{h}^2+\frac{3}{4}\frac{|\boldsymbol{r}_{ij}|}{h}^3 & , \text{ if } 0 \leq \frac{|\boldsymbol{r}_{ij}|}{h} < 1 \\ \frac{1}{4}\left(2-\frac{|\boldsymbol{r}_{ij}|}{h}\right)^3 & , \text{ if } 1 \leq \frac{|\boldsymbol{r}_{ij}|}{h} < 2 \\ 0 & , \text{ otherwise} \end{cases} \tag{3.18}$$

3.4.7 Variable smoothing length

The assumption of a constant h may cause trouble in simulations where the scale length changes. As soon as the particles become tightly packed compared to h the method breaks down, therefore h needs to vary. The number of neighboring particles needs to be roughly constant throughout a simulation, and the SPH code used in this project tries to maintain the number of neighbors between 30-70 for three-dimensional simulations.

Many ways of introducing a variable smoothing length to SPH exist. Benz (1990) suggest one which can give excellent results in practice without substantially slowing down the code. They give each particle an individual smoothing length h_i and then replace $h = 0.5(h_i + h_j)$, where i, j are the compared particles. An estimation to the smoothing length is then computed using the previous value and the change in the smoothing length with time as:

$$\frac{dh_i}{dt} = \frac{1}{3}h\nabla \cdot \boldsymbol{v}_i$$

This equation will maintain the number of neighbors of each particle well. If this form should begin to fail as the number of neighbors approach the lower or upper boundary discussed above, the expression is replaced by:

$$\frac{dh_i}{dt} = \frac{\exp(\Psi)(h\nabla \cdot \boldsymbol{v}_i)/3 \pm \exp(-\Psi)2h_i}{\exp(\Psi)+\exp(-\Psi)} \tag{3.19}$$

where $\pm$ is chosen depending on if the smoothing length needs to increase(+) or decrease(-). The exponential Ψ is calculated as:

$$\Psi = \begin{cases} (N_{\rm up} - N_n)/(0.3n_{\rm range}) & , \text{ if } (N_{\rm up} - N_n) < n_{\rm range} \\ (N_n - N_{\rm low})/(0.3n_{\rm range}) & , \text{ if } (N_n - N_{\rm low}) < n_{\rm range} \\ \infty & , \text{ otherwise} \end{cases} \tag{3.20}$$

where $N_{\rm up}$ and $N_{\rm low}$ are the upper and lower boundaries on number of neighbors a particle should have, and $n_{\rm range} = 12$ for three-dimensional simulations.

3.4.8 Time integration

Originally, SPH codes utilized a method by Benz (1984) that was based on a second order Runge-Kutta-Fehlberg integrator with adaptive time steps. The step size was set by constraints of changes on several physical properties of the particles. Particles situated in the central regions of modeled objects require smaller time steps, as the particle separations are small and densities large, compared to particles at the edge of the object where particle separations are large and densities small. With the same time step for all particles, high-density particles will set the time step and the low-density particles will use an excessive amount of iteration time.

The solution is to adapt individual time steps for particles, which will decrease simulation time. The required time step for all particles are calculated but their individual time step is restricted by the minimal time step required by the low-density particles. Particles are then binned into equivalent multiples of the minimum time step, and high-density particles will be iterated in several steps for the same time as low-density particles are only iterated for a few.

Individual required time steps of the particles are set by the lowest of three conditions; the force, Courant and Runge-Kutta conditions. The force condition gives a maximum allowed time step for a particle:

$$\Delta t_F = 0.3\sqrt{\frac{h}{|\boldsymbol{F}|}}$$

where $\boldsymbol{F}$ is the net force exerted on the particle. The Courant condition restrict the time step of a particle as:

$$\Delta t_{\rm cr} = \frac{0.3h}{c_{\rm s} + h|\nabla \cdot \boldsymbol{v}_i| + 1.2(\alpha c_{\rm s} + \beta h|\nabla \cdot \boldsymbol{v}_i|)}$$

where $\boldsymbol{v}_i$ is the particle velocity and α, β the two free parameters for the viscosity. The last term in the denominator is only used if the particle is decelerating ($\nabla \cdot \ \boldsymbol{v}_i \ < 0$). The third condition is same as for the Runge-Kutta-Fehlberg with adaptive time steps as discussed above, determined from restricted changes of the particle properties. The maximum time step endorsed by the condition is given by:

$$\Delta t_{\rm RK} = \sqrt{\frac{512\delta t_{\rm old}\lambda}{|Q_{\rm new} - Q_{\rm old}|}}$$

where $\Delta t_{\rm old}$ is the previous time step, λ determines the tolerance level and Q is the investigated particle property such as velocity, acceleration, internal energy or smoothing length. The lowest of time step as determined from these three conditions will set the time step of the investigated particle.

Round-off errors are expected especially if the difference in time steps range many orders of magnitudes. The binning of the particle's time step as described above allows for an integer representation of the time steps. With integers, no round-off errors occurs as this representation allows for a time step difference of 2^{20} for standard FORTRAN integers (Bate 1995).

3.4.9 The final Navier-Stokes equations

The energy and momentum equations of the Navier-Stokes equations were previously discussed in their simplest forms, disregarding of both viscosity and self-gravity. The contributions of viscosity and self-gravity is applied by adding their respective equations into Eq. (3.15) and (3.16). Adding the contribution of viscosity into Eq. (3.16) the energy equation becomes:

$$\begin{aligned}\frac{du_i}{dt} &= \frac{P_i}{\rho_i^2}\sum_{j=1}^{N} m_j(\boldsymbol{v}_{ij})\cdot\nabla_i W(\boldsymbol{r}_{ij},h) \\ &+ \frac{1}{2}\sum_{j=1}^{N} m_j\Pi_{ij}(\boldsymbol{v}_{ij})\cdot\nabla_i W(\boldsymbol{r}_{ij},h)\end{aligned}$$

In the same way adding the contribution of viscosity and self-gravity into Eq. (3.15) the momentum equation becomes:

$$\frac{dv_i}{dt} = -\sum_{j=1}^{N} m_j\left(\frac{P_i}{\rho_i^2}+\frac{P_j}{\rho_j^2}+\Pi_{ij}\right)\nabla_i W(\boldsymbol{r}_{ij},h) - \nabla\phi_i$$

This concludes the discussion on SPH, and in the next section we discuss the method of analyzing the results of the collisions, determining mass and energy losses for the planet(s) post-collision.

4 Post-collision analysis

Details on generating models and simulating the collisions was discussed in previous Sectionss 2.2 and 3. In the simulations, the planets are considered to start from an infinite separation with an initial velocity V_∞ and move toward each other with a specified periapsis. If the planets would just simply pass each other by, without any physical contact, they would be able to escape each others' potential well due to their initiated V_∞, and remain unbound. In collisions the planets lose energy and

material and the energy loss may be enough to bind them, and they will eventually return for another collision. The methods for determining mass and energy losses in the collisions are discussed in this section.

4.1 Mass loss

The mass lost from the system or individual planets is determined by calculating the material bound to the center of mass (COM) of the planet(s). An iterative procedure by Dale & Davies (2006) has been used for this, which determines the COM and bound material for the planet(s) and if the planets are bound. It begins with a simple estimation of the planet's COM, calculated from the particles that initially were bound to the planet prior to the collision. This is a crude estimation, especially for violent collisions, as material is ejected and transfered between the planets in the collision but serve as a good starting point. The COM, and its velocity, is calculated by summing the contribution of each particle, weighted by the sum of the particle masses $m_{\mathrm{p,i}}$ as:

$$\boldsymbol{r}_{\mathrm{com}} = \frac{\sum_{i=1}^{N} m_{p,i}\ \boldsymbol{r}_i}{\sum_{i=1}^{N} m_{p,i}} \tag{4.1}$$

$$\boldsymbol{v}_{\mathrm{com}} = \frac{\sum_{i=1}^{N} m_{p,i}\ \boldsymbol{v}_i}{\sum_{i=1}^{N} m_{p,i}} \tag{4.2}$$

where $m_{p,i}$ is the mass of the i :th particle, and $\boldsymbol{r}_i$, $\boldsymbol{v}_i$ its position and velocity vectors respectively. The amount of bound material to the COM is computed by determining the total energy E_{tot} of each particle as:

$$E_{\mathrm{tot}} = E_{\mathrm{kin}} + E_{\mathrm{int}} + E_{\mathrm{pot}} \tag{4.3}$$

An unbound particle will move away from the COM with a positive total energy, while a bound particle has a negative energy and is captured in the potential well of the bound material.

From the remaining bound material the new COM can be determined and this procedure is repeated a number of iterations. In this way bound material is determined with increasing accuracy, and the object's mass, volume and mass loss can be determined. The mass loss is defined as $\Delta M/M_0$, where M_0 is the system's initial mass. If the planets have not merged, which the iterative procedure of Dale & Davies (2006) define as if their COMs are separated by ≤ 0.2 $\mathrm{R_J}$, the planets' individual mass loss is also determined and denoted as $\Delta M/M_i$ for planet i.

4.2 Energy loss

The velocity at infinity (V_∞) specify the planets' initial energy E_0 as:

$$E_0 = \frac{1}{2} M_p V_\infty^2 \tag{4.4}$$

where M_p is the planet's mass. The initial energy E_0 allows the planets to escape each others' potential well in a close encounter. For collisions, the planets will lose energy and an energy loss equal to or larger than the initial energy E_0 would cause the planets to become bound. By determining the energy loss relative to the initial energy, unbound and bound planets can be distinguished which is of interest as bound planets may return for additional collisions.

In the rest frame of the first planet the energy E_t at a time t is determined by the sum of the kinetic and potential energy of the second planet. This way, the energy E_t is calculated as:

$$E_t = \frac{1}{2}M_2V^2 - G\frac{M_1M_2}{R_{\text{sep}}} \tag{4.5}$$

where the first term is the kinetic energy and the second the gravitational energy. The masses M_1, M_2 of the planets are determined from the bound material, and the relative velocity V is determined by the relative velocity of the planets' COM. The energy E_t is determined at a time after the collision when the planets separated by a separation R_{sep} large enough so that the planets can be distinguished (hence not already merged). Using this, the energy loss is in this project defined as:

$$\frac{\Delta E}{E_0} = \frac{E_t - E_0}{E_0} = \frac{E_t}{E_0} - 1 \tag{4.6}$$

For just bound planets, the energy loss will be $\Delta E/E_0$ = -1. Bound systems require an energy loss of $\Delta E/E_0 \leq$ -1, hence the planets have lost an amount of energy equal or larger than their initial energy E_0. In less violent collisions, such as grazing, the energy loss may be small and the planets remain unbound after the collision, and hence the energy loss is $\Delta E/E_0 >$ -1.

The boundary radius at which the planets are just bound can be determined by looking at the behavior of energy loss with periapsis. This will be discussed in more detail in Section 6.2. In next section the return time for bound planets is discussed, which is useful in order to discern whether to continue or reinitiate the collision.

4.3 Return time

Bound systems with $\Delta E/E_0 \leq$ -1 are of special interest in this project, as the planets eventually will merge. The return time for the second collision might however be very long. In these cases it may be more efficient to determine new initial parameters for the next collision and reinitiate rather than continue the simulation.

The bound planets will move in an orbit with a period P and semi-major axis a. How tight the orbit is depends on how much energy the planets have lost, and hence how tightly bound they are. The total orbital energy E_{orb} is calculated as:

$$E_{\text{orb}} = G\frac{M_1M_2}{2a} \tag{4.7}$$

where $1, 2$ denote the two planets in the system, M_i are the planet masses a the semi-major axis of the binary system. The orbital energy of the system can be compared

to the energy of the system $E_{\rm t}$, determined using Eq. 4.5. By combining Eq. (4.5) with (4.7), the semi-major axis of the system can be determined by solving for a as:

$$a = \frac{GM_1M_2}{2E_{\rm t}} \tag{4.8}$$

where E_t is determined using Eq. (4.5). Using Kepler's third law the semi-major axis can be used to determined the period of the system, and hence the return time for the planets second collision. Kepler's third law relates the square of the system's period to the cube of the semi-major axis, from which the period can be calculated by solving for P as:

$$P = \sqrt{\frac{a^3(2\pi)^2}{G(M_1+M_2)}} \tag{4.9}$$

Determining the return time of the planets, approximately half the period, a decision to continue the simulation or reinitiate a new can be made. Before the collisions can be simulated, initial conditions for the simulations needs to be determined which is discussed in next section.

5 Initial conditions of collisions

The initial conditions for the collision simulations have not yet been discussed. These consist of planet masses, relative velocities and separations at closest approach during the collision. Planetary masses can be determined from observations of exoplanets while velocities and separations at closest approach require an alternate method.

Statistics on the planets' relative velocities prior to the collisions need to be determined for initiating the collision simulations but cannot be determined through observations. There are no observations of colliding planets, with the exception for post-collisional observations. Instead statistics are gathered by iterating a number of planetary systems using the MERCURY N-body integrator. The planet masses to investigate is first determined from observational data.

5.1 Planet mass

Observations of exoplanets for most cases only reveal the minimum mass, as the inclination of the planet is unknown and hence the determined mass is $M \sin i$. Statistically the factor $\sin i$ takes on a small average value and the true mass of the observed exoplanets are generally close to the determined minimum mass (Cumming et al. 2008).

A histogram of exoplanet masses as of 2010-05-12 is given in Figure 4 for masses ranging between 1 - 26 $\rm M_J$ in bins of 1 $\rm M_J$. The histogram show how a large number of exoplanets have been observed with masses comparable to Jupiter in the range 1 - 5 $\rm M_J$. Most observational methods favor a large exoplanet mass for detectability,

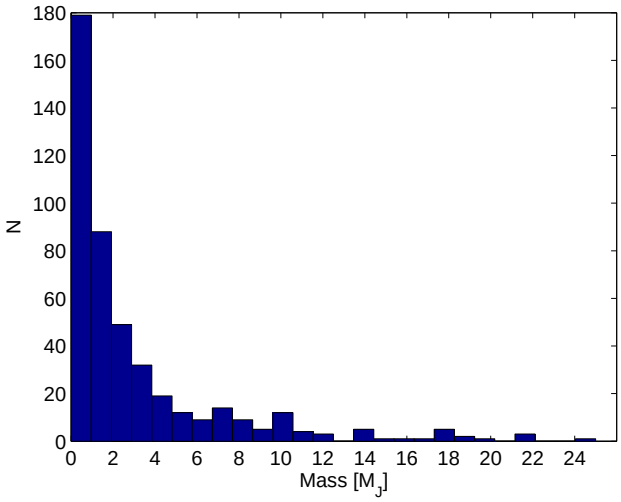

Figure 4: Histogram of determined minimum masses of observed exoplanets as of 2010-05-12 with 455 exoplanets gathered from the database of `http://exoplanet.eu` in the range $0 - 26$ M_J.

still most observed exoplanets have masses < 5 M_J and the relative amount to the more massive planet could be larger.

The fractional mass of the planets will only have a significant effect on the impact velocities when the planets gets close. In the MERCURY simulations we only considered planet systems with three Jupiter-mass planets as we are merely interested in determining the velocity well before the impact and the probability of the collisions. The detailed effect of different planet masses is fully modeled in the later collision simulations. As the majority of observed exoplanet masses lie in the range $1 - 5$ M_J, the three planet masses for the collision simulations were chosen as $1, 3$ and 5 M_J.

5.2 N-body integration

Properties of planets prior to the collisions can be investigated by integrating a few systems using a N-body integrator. Using the N-body integrator MERCURY (Chambers 1999), systems consisting of three Jupiter-like planets can be investigated and information extracted on the collisions.

MERCURY has a number of integration packages, useful for different situations and with different levels of accuracy. The Bülirsch-Stoer method by Stoer & Bulirsch (1980) is a relatively slow integration method, but has the advantage that it conserves energy with high accuracy. A high level of accuracy is important if the systems experience numerous close encounters which are sensitive to small deviations in the energy conservation.

To identify the collisions, each system was run once until any two planets experienced a collision. The simulation was then stopped and information on the time

and the planets' separation during the collision was recorded. Every system was then rerun with a modified version of MERCURY that begins tracking the colliding planets 50 time steps prior to the collison. As soon as the planets are within 0.5 au of each other the planets' positions and velocities were printed to a file.

Collisions are rare events, so to avoid excessively long simulations, the systems were intentionally generated as unstable, which significantly increase the number of close encounters and the probability for planet collisions. This in turn allows the systems to be integrated for shorter times and the choice of the slower Bülirsch-Stoer algorithm becomes less significant. Generation of these unstable planetary systems is discussed next.

5.3 System stability

Studying the evolution of planetary systems consisting of a small number of planets can yield statistics for the collision simulations. Gladman (1993) investigated the stability of two planets of masses M_1 and M_2 orbiting a star of 1 $M_\odot$. They found that the two-planet system remained stable for circular orbits if the planets' initial separation $\Delta a = a_i - a_j$ met the criteria:

$$\Delta a \geq 2\sqrt{3} R_{\mathrm{H}(i,j)} \tag{5.1}$$

where $R_{\mathrm{H}(i,j)}$ is the planets' mutual Hill radius. Two objects with masses M_i and M_j orbiting a massive host can be considered to have a mutual Hill radius defined by Gladman (1993) as:

$$R_{\mathrm{H}(i,j)} = \left[\frac{M_i + M_j}{3M_\mathrm{s}}\right]^{1/3} \frac{a_i + a_j}{2} \tag{5.2}$$

where a_i and a_j are the semi-major axes of the planets and M_s is the host star's mass. In this way, the separation between the two planets is determined as $\Delta a_{i,j} = K R_{\mathrm{H}(i,j)}$, where K is an integer of the mutual Hill radius. This mutual Hill radius defines a volume in which two smaller astronomical bodies dominate the gravitational attraction over a more massive body, such as a star. In this way, material within this mutual Hill radius is retained, and material outside may be accreted by the other body.

If Eq. (5.1) is not met, the planets build up enough perturbations for their orbits to cross and the systems may experience collisions. This criterion holds for a two-planet system, adding more planets to the system increases the complexity and the stability criteria in Eq. (5.1) will no longer be valid.

Marzari & Weidenschilling (2002) investigated the instability of multi-planet systems consisting of three Jupiter-like planets with varying masses. In one set of runs the systems were integrated with three Jupiter-mass planets, and in a second set the mass of the middle planet had been increased to 2 M_J. The planets' orbital separation was determined by an factor K of the planets' mutual Hill radius and the orbit of the inner-most planet was kept constant to $a_1 = 5.00$ au.

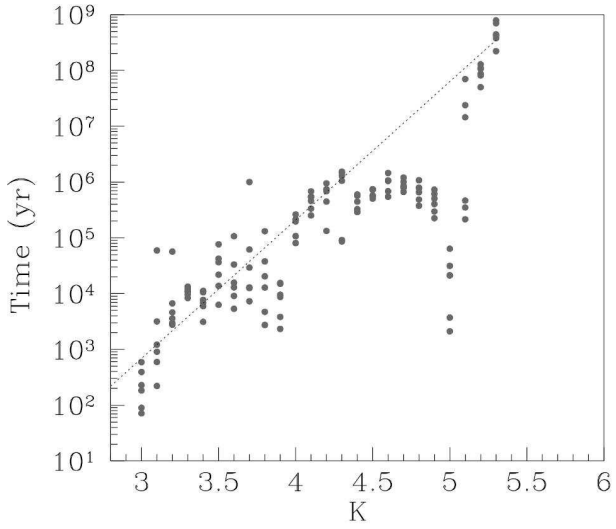

Figure 5: Figure from Marzari & Weidenschilling (2002) showing the change in timescale for the first close encounter with respect to orbital separations specified by a factor K of the planets' mutual Hill radius $R_{\rm H}$, for a system with three Jupiter-mass planets. The continuous line in the figure show the trend following the results of Chambers et al. (1996), which would be expected without the resonant perturbations in the system with Earth-mass planets.

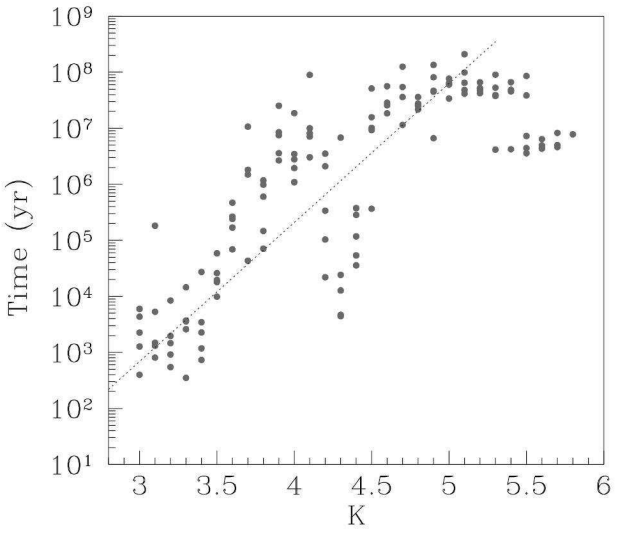

Figure 6: Figure from Marzari & Weidenschilling (2002) illustrating the change in timescale for the first close encounter with respect to orbital separation specified by a multiplicity K of the planets' mutual Hill radius $R_{\rm H}$, for a system with three planets of unequal mass. The two outermost planets have masses of Jupiter and the middle twice the mass of Jupiter. The continuous line has the same meaning as in Figure (5).

The results for systems with three Jupiter-mass planets are shown in Figure 5 with the time of first close encounter as a function of orbital separation. Chambers et al. (1996) investigated the stability of multi-planet systems, but for masses only up to Earth-mass. Their results showed a trend between the time of the first close encounter and K, which is plotted in Figure 5 as a continuous line. The results of Marzari & Weidenschilling (2002) showed a similar trend, however with a few drops in the time of first encounter, that can be interpreted as reduced instability, for certain values of K.

These drops in instability were determined to arise from mean motion resonances (MMR), generated by two orbiting objects with orbital periods that can be expressed as integer ratios of each other. Examples of this include Pluto and Neptune that orbit the Sun in a 2:3 MMR. This means that Neptune will have completed three orbits of the Sun in the same time that Pluto completes two. In Figure 5 these resonances are evident as big drops in instability at $K \approx 5$ and one smaller at $K \approx 4$. MMRs may work to either stabilize or destabilize systems, depending on the setup of the system. If the planets are synchronized in a MRR such that they never have a close encounter, the system will be stabilized, otherwise perturbations may build up faster to destabilize the system.

Marzari & Weidenschilling (2002) also investigated a system with three planets of unequal mass such that the middle planet has twice the mass of Jupiter, while the others have one Jupiter mass. The result is shown in Figure 6 with a continuous line indicating the expected results without resonant perturbations, as Chambers et al. (1996) found. One single drop is evident in the figure at $K \approx 4.5$, determined to result from a MMR as well. No significant change in the time of the first close encounter, and the measurements from the unequal-mass system followed the trend of Chambers et al. (1996) fairly well. With these results appropriate initial separations of the planets can be specified for the N-body simulations by determining a semi-major axis of the innermost planet a_1 and a value for K, which is done next.

5.4 Planet orbits

Orbital separations of the planets in the MERCURY runs have to be chosen wisely to be unstable but not too unstable, but also avoid drops in instability arising from MMRs. First the orbits of the systems should be determined. Observations of exoplanets have revealed that they orbit their host star with a wide range of semi-major axes.

The cumulative distribution of semi-major axes for observed exoplanets is plotted in Figure 7, which shows a large range of orbits ranging from 0.01 au and up to ~ 700 au. The very tight planet orbits with $a < 1$ au are not consistent with the standard formation model, that predicts gas giants form outside of the snow line. The snow line marks the distance to the host star inside which the temperature is high enough to evaporate ice and other hydrogen compounds. Here the gaseous envelope that engulfs the inner core-like structures of gas giants has evaporated, and only the rocky core remains. Hence gas giants, according to the standard formation model,

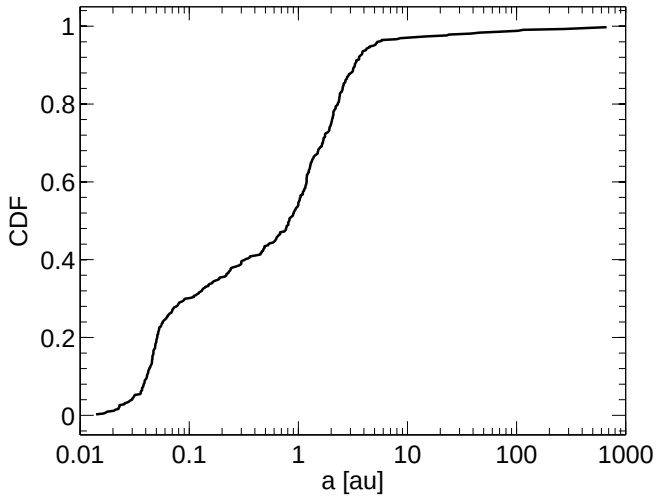

Figure 7: Cumulative distribution of semi-major axes for observed exoplanets as of 2010-05-24 with semi-major axes > 0.01 au.

form in wider orbits with small orbital velocities, while terrestrial planets form much closer to the host star with larger orbital velocities.

Many theories exist as to how hot Jupiters have moved into tighter orbits from their formation site at larger distances to the host star and two theories are considered the most probable; migration and planet-planet scattering. In young planetary systems, gas giants may migrate into a tighter orbit by interacting with the dust of the protoplanetary disk that forms around the host star. Planet-planet scatterings may cause gas giants to be sent into eccentric orbits. If the orbit is not eccentric enough so that it may instead collide with the star, the gas giant may interact with the disk which effectively circularizes the planet into a tighter orbit (Lubow & Ida 2010; Marchi et al. 2009).

It would take an excessive amount of time to investigate the whole range of observed exoplanet orbits, so we had to limit the range. Exoplanets in extremely wide orbits (> 10 au) as well as extremely tight (< 1 au) have only been observed in small numbers. The majority of orbits of observed Jupiter-like exoplanets lie in the range $a \approx 0.1 - 3$ au.

The orbital velocity is similar to V_∞, mentioned in the previous section as an important parameter of the collision simulations. The tight systems will have the largest orbital velocities, and hence harbor the most violent collisions, while wide systems will harbor low velocities. The orbital velocity $V_{\rm orb}$ for circular orbits is computed as:

$$V_{\rm orb} = \sqrt{\frac{G(M+m)}{a}}$$

where M is the host star's mass, m the planet's mass and a the orbit of the planet around the star. Considering a planet orbiting a solar-mass star, the orbital velocities

for the discussed range of orbits that exoplanets have primarily been observed in, are $V_{\rm orb} = 9.24 - 94.2$ km/s.

Four systems were investigated in this orbit range, with the orbit of the innermost planet $a_1 = 0.1$ au, 0.5 au, 1.0 au and 3.0 au. For each of these systems were 100 realizations integrated. With orbits ranging from $0.1 - 3.0$ au the systems are similar to both hot Jupiters and Solar system-like orbits.

Figures 5 and 6 from Marzari & Weidenschilling (2002) showed how the time of the first close encounter (defined $\tau_{\rm CE}$ in this project) depended on the planet separations determined by K. Collisions are rare events and systems will have experienced numerous close encounters before any planets get close enough for a collision. Therefore the systems need to be integrated for a significantly larger time than $\tau_{\rm CE}$ for an adequate number of collisions to occur. The planets in the wide systems require a longer time to finish one orbit and the expected time between close encounters is large, hence the collision rates will be smaller.

A $K = 3$ will, according to figures 5 and 6, allow the systems to quickly become unstable and the resulting planet orbits show no clear signs of any MMRs for the determine planet orbits, using the above chosen a_1. The systems would need to be integrated for a significantly longer time than $\tau_{\rm CE} \approx 10^3$ years. Ten test systems were initiated with an integration time of 10^6 years and planet orbits $a_1 = 3.00$ au with $K = 3$. Between each realization a position in the orbit was randomly chosen for each of the three planets. Exoplanets do not form in circular orbits without any inclination, and hence small inclinations between -2° and 2° were also randomly chosen between each realization for the three planets.

Three of the systems experienced a planet-planet collision and one had a planet collide with the Sun. All of the systems were reasonably stable after $\sim 40,000$ years and experienced no further collisions or ejections after this time. A collision rate of 30% for these wide systems is reasonably large, and the rate is expected to increase significantly for the tighter systems. Since we only investigated ten systems, the time for all systems to become stable again may be larger, so we determined a reasonable maximum integration time for the systems to be 100,000 years.

In Table 3, the initial orbits of the four systems are listed. We do not want the simulations to take too long time, so we did not want to investigate very wide orbits of the planets as this will increase the iteration time needed. The choices of planet orbits gives a good spread in range from very tight to wide systems, where the outermost planet in the widest system ($a_1 = 3.00$ au) has an orbit similar to that of Jupiter. The orbital velocities of the planets will vary a lot when considering tighter orbits, but for wider systems the difference is less significant. Considering an object orbiting the Sun at 5 au (Jupiter) to 10 au (Saturn), where the orbital velocities are 13.32 km/s and 9.42 km/s respectively, the difference is not very large.

Changing the mass of the planets will only affect the impact velocities as the planets are accelerated by each other's gravitational pull. Hence it is not necessary to investigate different planet masses. At larger separations the host star's mass will dominate and the change in planet mass will not affect V_∞ significantly. Before the velocities at large separations are discussed the collision probabilities are discussed.

$M_i = 1$ M$_\mathrm{J}$		
a_1 [au]	a_2 [au]	a_3 [au]
0.10	0.13	0.17
0.50	0.65	0.84
1.00	1.30	1.89
3.00	3.89	5.04

Table 3: Simulated system using MERCURY where masses and semi-major axes of the planets are changed, and 100 realizations are done for each systems, randomly changing the inclination and position of the planets and their orbits. The planets' separation are determined by a factor $K = 3$ of their mutual Hill radius, as was discussed in Section 5.3.

5.5 Collision probability

Apart from planet-planet collisions, the systems may experience two other events that may stabilize them. The numerous close encounters that the planets experience will alter the orbits of the planets, changing their eccentricities and semi-major axes. If the eccentricity e becomes large enough, a planet may collide with the Sun, or be ejected from the system if $e > 1$. Either of these events will decrease the number of planets and may stabilize systems as the planets experience weaker perturbations.

a_1	0.1 au	0.5 au	1.0 au	3.0 au
Planet collisions	99%	68%	43%	17%
Collisions with Sun	5%	13%	12%	10%
One or more planets ejected	0%	9%	8%	6%
Collisions ending with three planets	0%	20%	51%	67%

Table 4: Collision probability ψ as a function of the semi-major axis of the inner-most planet a_1 for investigated systems using the N-body integrator MERCURY.

In Table 4 the fraction of realizations for each investigated system that experienced either of these events are listed. A few of the simulated systems ended up with only one planet as they experienced more than one of the above possible events. Since the simulations were stopped as soon as a planet collision occurred, none of the systems experienced two planet collisions.

Wide systems show a significantly lower rate for planet collisions as the expected mean time between close encounters are significantly longer for wide systems. There is a significant difference in the collision rate of the investigated systems, but also an expected difference in how common each of the systems are. While tight systems have the highest planet-planet collision rate, the planets need to migrate or planet-planet scattering into these orbits as gas giants are predicted to form in much wider

orbits (Marchi et al. 2009).

The planets will have different orbital velocities for the different systems, and this determines the velocity at which they will approach each other prior to the collision. The velocities of the planets prior to the collisions are discussed in the next section.

5.6 Velocity at infinity

For the collision simulations, the planets are initiated with a specified velocity at infinity (V_∞). The planets' relative velocity at a large separation will help to determine reasonable V_∞ to initiate the collisions with. The resulting relative velocities are plotted in Figure 8 as a function of the planet separation. The four systems cover a wide range of velocities at large separations. Comparison with theoretical evolution of the relative velocities will yield the equivalent V_∞.

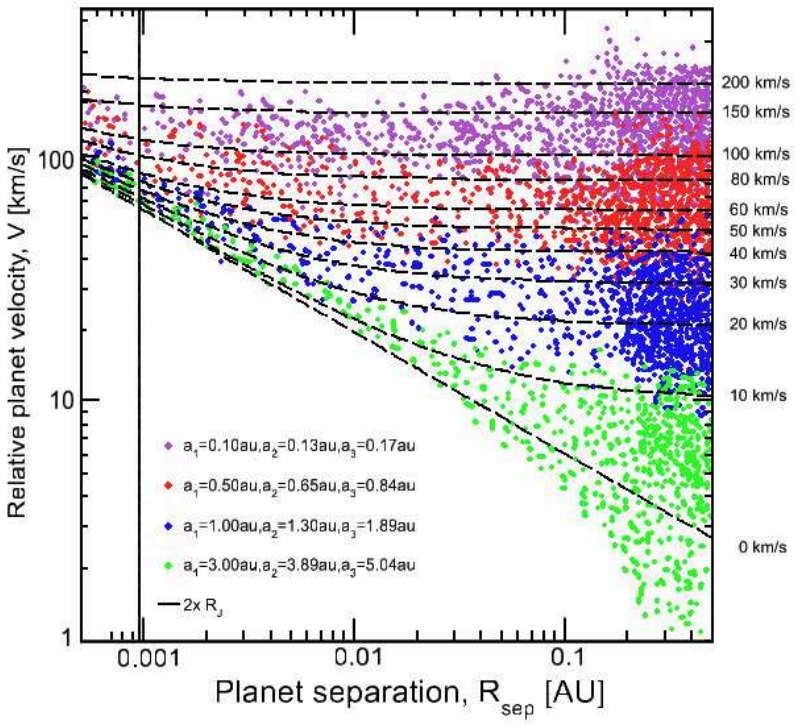

Figure 8: Relative velocities V between planets involved in close encounters as a function of their separation $R_{\rm per}$, for systems consisting of three Jupiter-mass planets, with initial orbits determined by $K = 3$ (see discussion in Section 5.3). The colors of the data represent the different investigated system, where the data of each system is gathered from 100 realizations where position and inclination of orbits have chosen randomly. The tightest systems are plotted in violet with the innermost planets at an orbit with $a_1 = 0.1$ au and the widest system in green with an orbit a_1 =3.0 au. In between the systems are initiated with an $a_1 = 0.5$ au plotted in red, and with $a_1 = 1.0$ au in blue.

Consider two planets initiated at an infinite separation with the relative velocity V_∞. In the rest frame of the first planet, the initial energy E_0 is computed using Eq. (4.4). At a later time with a finite separation, the total energy is computed using Eq (4.5) with a relative velocity V of the planets. Total energy is conserved at any time in the simulations. Rearranging the planets' relative velocity V can be computed for specific V_∞ as:

$$\begin{aligned} \frac{1}{2}M_p V_\infty^2 &= \frac{1}{2}M_p V^2 - G\frac{M_p^2}{R_{\rm sep}} \\ V^2 &= V_\infty^2 - \frac{2GM_p}{R_{\rm sep}} \end{aligned} \tag{5.3}$$

where M_p is the first planet's mass. A wide range of V_∞ were chosen to determine the evoluion of V with planet separation and they are plotted in Figure 8 as dashed lines. The dashed lines show a large spread for V_∞ ranging from $V_\infty = 0$ km/s up to $V_\infty = 200$ km/s. A small number of data points reside below the expected evolution of V with $V_\infty = 0$ km/s. Planets moving in opposite directions and pulled toward each other by their gravitational pull, can generate such measurements as the gravitational pull has to work more to reduce their oppositely directed velocities and cause them to collide. At smaller separations these ultra-low velocities disappear and the planets' follow the expected evolution from the theoretical calculations.

There is a spread in relative velocities at larger separations ($R_{\rm sep} \geq 0.1$ au) for the systems. During the numerous close encounters the planets experience prior to the collision, their orbits will change. In planet-planet scattering the planets can be sent into larger or smaller orbits with an increased eccentricity (Chatterjee et al. 2008), which will affect the orbital velocities and velocities at large separations.

a_1 au	$\langle V \rangle$ km/s	$\sigma_{\langle V \rangle}$ km/s
0.10	119.48	36.60
0.50	49.65	19.29
1.0	21.21	12.75
3.0	13.86	9.11

Table 5: Properties of four different systems investigated using the N-body integrator MERCURY, altering mass or orbits of the planets between systems with 100 realizations for each. The semi-major axis of the innermost planet is specified in the first column, and the orbits of the other planets are determined by a factor $K = 3$ of the planets' mutual Hill radius (see Section 5.3 for discussion on this). The average value of the relative velocity at large separations ($R_{\rm sep} \geq 0.1$ au) and its standard error is listed in the last two columns.

In Table 5 the extracted values for the systems are listed together with their standard error and a_1 of the systems. The mean velocity $\langle V_\infty \rangle$ of the system and its standard error are listed in the two last columns, determined from the planets at large separations $R_{\rm sep} \geq 0.1$ au. The standard error of the mean is calculated as:

$$\sigma_{\langle V \rangle} = \sqrt{\frac{1}{N}\sum_{i=1}^{N}(v_i - \langle v \rangle)^2}$$

In the project we want to investigate a range of reasonable impact velocities and three sets of V_∞ are chosen spawning from low-velocity collisions to violent collisions. The three chosen velocities are $V_\infty = 20, 60, 100$ km/s. The low-velocity collisions with $V_\infty = 20$ km/s are expected to generate small mass losses and the velocity is low enough for many of the collisions to result in mergers. Comparing the velocity to the orbital velocity of Jupiter $V_{\rm orb,J} = 13.07$ km/s, these collisions would be similar to gas giants forming in wide orbits. Collisions with $V_\infty = 60$ km/s will generate moderate amounts of mass losses, while $V_\infty = 100$ km/s will result in violent collisions which may significantly damage the planets' structure. Important to note, and the reason for our choice of investigating $V_\infty = 60$ km/s, is that the escape velocity at the surface of Jupiter is $V_{\rm esc,J} = 59.5$ km/s. In the next section the separations at closest approach for the collisions are discussed.

5.7 Periapsis

How violent the collisions are and how much material is lost will depend not only on the impact velocity but also the point of closest approach, periapsis, in the collision. The periapsis $R_{\rm per}$ is defined as the separation between the planets' centers of mass where $R_{\rm per} = 0$ $\rm R_J$ is a head-on collision and $R_{\rm per} = R_1 + R_2$ a grazing. Specifically for two Jupiter planets with radii 1 $\rm R_J$ the planets will have a grazing collision if $R_{\rm per} = 2$ $\rm R_J$.

Consider the observer situated in the rest frame of one of the planets (target) with the second planet (impactor) approaching for a collision. The probability for a collision with a specific periapsis $R_{\rm per}$ will depend on the collisonal cross section σ_c (Kessler 1981) calculated as:

$$\sigma_{\rm c} = \pi R_{\rm per}^2 (1 + V_{\rm e}^2/V_\infty^2) \tag{5.4}$$

where $V_{\rm e}$ is the escape velocity calculated as $V_{\rm e} = [2(M_1 + M_2)G/(R_1 + R_2)]^{0.5}$ and R_1, R_2 are the planets' radii. V_∞ is a constant in all simulations but the escape velocity depends on the planet separation. As the planets get closer, the gravitational forces become notable and will begin to pull them closer. This is called gravitational focusing represented by the second term in the parenthesis of Eq. (5.4). The concept of gravitational focusing is illustrated in Figure 9.

At large separations where $V_\infty > V_{\rm e}$, the gravitational focusing is negligible and the collision cross section scale to the periapsis as $\sigma_{\rm c} \propto R_{\rm per}^2$. At small separations,

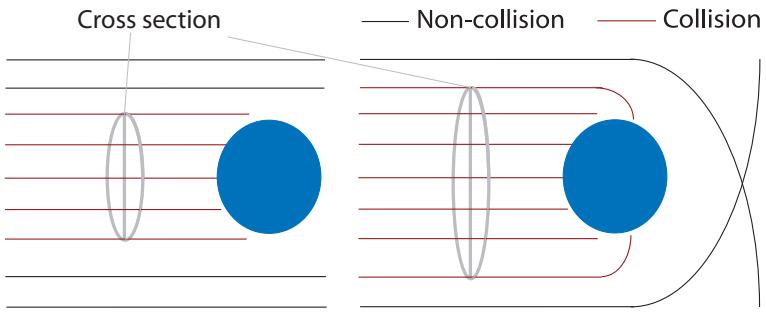

Figure 9: Illustration of the concept of gravitational focusing. Without it planets would only collide if they are initiated with a vertical separation of less or equal to two planet radii. Due to gravitational focusing the probability for collisions increase.

$V_e > V_\infty$ and the gravitational focusing term will no longer be negligible. The escape velocity scales to periapsis as $V_e \propto R_{per}^{-1/2}$, and depending on periapsis, the distribution is expected to be linear at small separations (head-on collisions) and quadratic at larger separations (grazing collisions), ranging $R_{per} = 0 - 2$ R$_J$.

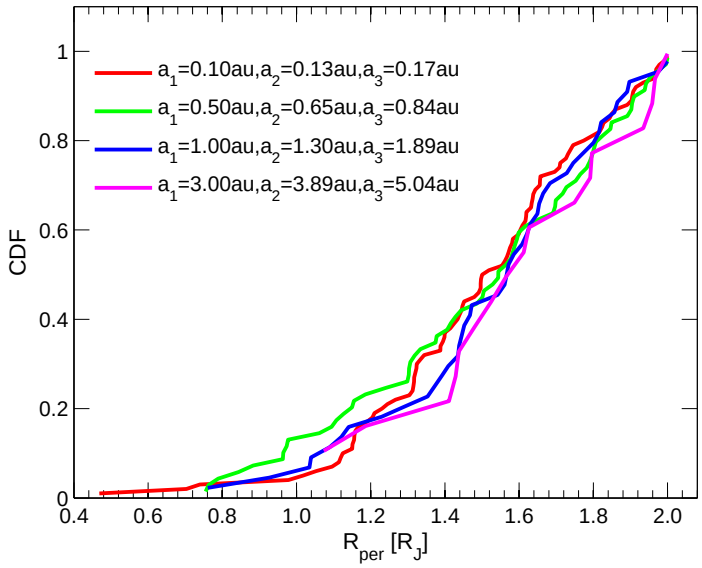

Figure 10: Cumulative distribution of R_{per} for the four planet systems (from MERCURY).

CDF of R_{per} for the four investigated systems are plotted in Figure 10. After normalized to unity, the four systems show a similar distribution of R_{per}. The theoretically predicted distribution of R_{per} compares well to the determined distribution from the MERCURY runs.

The systems are integrated with a finite time step in MERCURY and R_{per} of the collision cannot be determined accurately unless a very small time step is utilized.

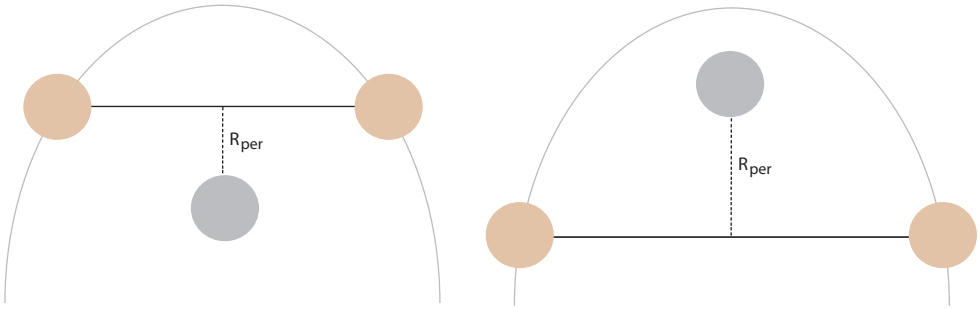

Figure 11: Illustration of how MERCURY determines $R_{\rm per}$ of a close encounter with an inadequate time step to resolve the encounter. In the left figure $R_{\rm per}$ is overestimated, and in the right underestimated due to interpolation at finite time steps. This will depend on the time step, and the motion of the planets during the close encounters.

For inadequately small time steps for the separations at the closest approach to be resolved during collisions, MERCURY solves this by interpolation of the two points closest to the periapsis to approximate its value. This works well for close encounters where the time step is short compared to the time of the close encounter, but less accurate for collision where the time frame of the event is very short. This may result in a under- or overestimation of $R_{\rm per}$ for the collisions, illustrated in Figure 11, and will affect the CDF, specifically for smaller values of $R_{\rm per}$.

The distribution of periapsides is consistent with the expected behavior at large periapsides. At smaller periapsides the time step is not small enough to resolve the collisions and the left case illustrated in Figure 11 occurs, which underestimates the periapsis during the collisions. The simulations invoked a time step of 0.01 days, and considering a mean velocity for colliding planets in all collisions $\langle V_{imp} \rangle \approx 91.5$ km/s. This means that MERCURY using $\Delta l = V \Delta t$, where Δl is the resolved length, resolves the collisions down to a scale of $R_{\rm per} \approx 1.11$ $R_{\rm J}$. A lower time step would allow to resolve the collisions at lower periapsides, but also result in an excessively longer integration time, instead we determine that the distribution hold also for smaller separations.

Collisions with large periapsides may lose enough energy to become bound (see Section 4.2), in which case the planets will be bound in an orbit and possibly return for a second collision. The gravitational focusing causes the periapsis to be lower for the second collision. This may boost the CDF at smaller periapsides. This effect on the CDF cannot be investigated using MERCURY as the code only simulates collisions as perfectly inelastic. Instead of just part of the kinetic energy being converted into thermal energy, both planets merge and the properties of the two planets are added to form one single new planet.

This means that we cannot investigate exactly how probable head-on collisions are, but we can predict that the CDF will be boosted for smaller periapsides. Head-on collisions are expected to be the most violent in terms of mass and energy losses, and are of interest even though they are less probable than grazing collisions.

Five periapsides are chosen evenly distributed from head-on to grazing collision. In a head-on collision the planets may stick together and instantly merge, just as for an inelastic collision. To investigate whether this is also possible for larger periapsides, and whether it gives similar results in terms of mass loss, a sixth periapsis is investigated with $R_{\text{per}} = 0.1$ R$_{\text{J}}$. In the next section the number of particles in the SPH collisions is discussed.

5.8 SPH particle numbers

As mentioned in the discussion on SPH in Section 3 the planet models are divided into a number of particles that each will represent a finite volume. The larger number of particles in the model, the higher the accuracy that can be attained. The time needed to complete one run will increase as well, scaling as $N \log N$ where N is the number of particles.

Two different planet models of Jupiter-massed objects were compared, consisting of 15,000 and 30,000 particles. One typical collision with $R_{\text{per}} = 1$ R$_{\text{J}}$ and $V_\infty = 60$ km/s and one violent with $R_{\text{per}} = 0.1$ R$_{\text{J}}$ and $V_\infty = 100$ km/s were initiated to compare the models.

The planet models were compared in three ways by: (1) The density profiles of the planet(s) prior and post collision. (2) Mass and energy losses using the methods discussed in previous sections. (3) The level of energy conservation.

The density profile is an important property of the models as it affects the other properties such as pressure and temperature. It is therefore useful to also compare the density profiles of the two models after the collisions. In Figure 12 the differences in density for the two models and both collisions are plotted. The difference is calculated from the average density of the two models as a function of radius, calculated for the models in evenly-spaced slices of $\Delta R = 0.01$ R$_{\text{J}}$, and normalized to the initial central density of the 30,000 particle model. The blue points are for the typical collisions and red for the violent collisions, and as expected the divergence is larger in the violent collision.

It is essential that the total energy of the simulation is conserved within reasonable levels or the determined mass and energy losses may not be accurate. An energy conservation of $\lesssim 1\%$ is endorsed for the collisions, giving an equivalent level of precision of the determined energy and mass losses. The energy error is determined by the maximum difference in total energy during the whole simulation as $E_{\text{err}} = E_{\text{max}} - E_{\text{min}}$. Collisions with small periapsides and large impact velocities will have the lowest energy conservation as these will be the most violent and most difficult to accurately simulate. The difference in total energy between the two models in the two collisions are plotted in Figure 13 as a function of time. The differences increase at the time of the collisions but are still insignificant.

In Table 6 values of energy conservation and mass loss are listed for the two models and collisions. The values are determined at the same time step for both models and the discrepancy is larger for the violent collision. The time needed to update properties of the planets in the SPH code will scale as $N\text{log}N$, where N

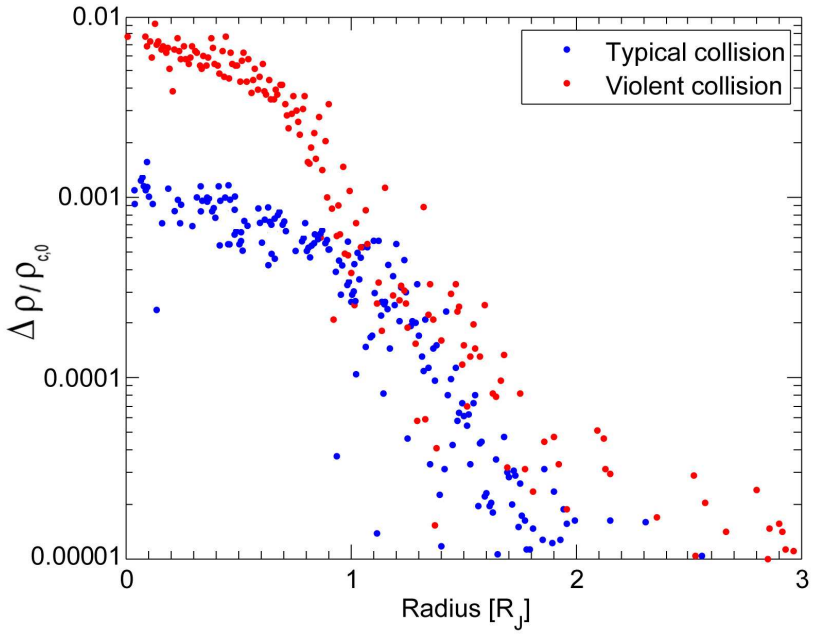

Figure 12: Difference in density profiles relative to the central density of the initial model for two different planet models of a Jupiter-like planet, consisting of 15,000 or 30,000 particles. The blue dots are from comparing models in a typical collision initiated with $V_\infty = 60$ km/s and $R_{\rm per} = 1$ R$_{\rm J}$, and the red dots for a violent collision with V_∞ =100 km/s and $R_{\rm per} = 0.1$ R$_{\rm J}$. $\rho_{\rm c,30}$ is the initial central density of 30,000 particle model which the density differences are normalized to.

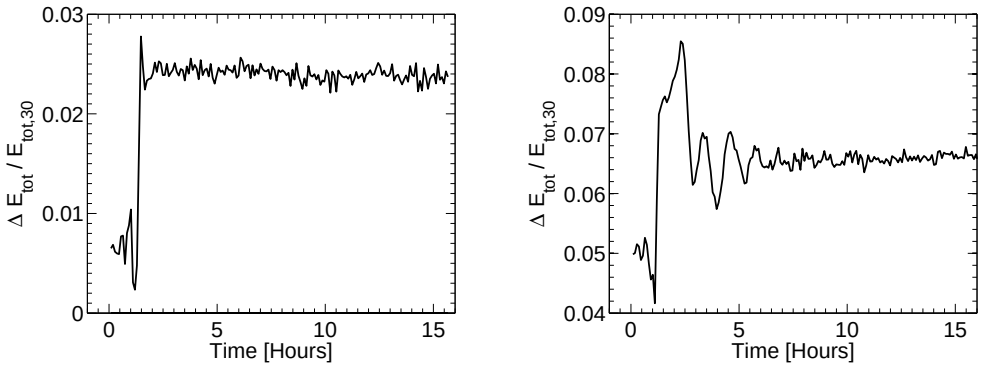

(a) Typical collision

(b) Violent collision

Figure 13: Difference in total energy between two polytropic models using 15,000 and 30,000 particles in one typical and one violent collision. The difference is determined as the difference in energy divided by the energy level of the 30,000 particle collision (which conserves energy best). $E_{\rm tot,30}$ is the energy level of the 30,000 particle model, which the energy differences between the models are normalized to.

Collision	N_{particle}	$\Delta E/E_0$	$\Delta M/M$	$E_{\text{err}}/E_{\text{min}}$
Typical	15,000	–0.861	1.86×10^{-2}	0.525
	30,000	–0.850	1.90×10^{-2}	0.522
Violent	15,000	IM	3.41×10^{-1}	1.25
	30,000	IM	3.36×10^{-1}	1.27

Table 6: Compared mass and energy losses as well as levels of energy conservation for two different collisions and planet models of 15,000 and 30,000 particles. The typical collision was initiated with $V_\infty = 60$ km/s and $R_{\text{per}} = 1$ R_J, and the violent $V_\infty = 100$ km/s and $R_{\text{per}} = 0.1$ R_J. IM denote that the systems instantly merged where no energy loss could be determined.

is the number of particles. Hence, doubling the amount of particles increases the simulation time by $\sim 60\%$. The insignificant gain in accuracy compared to the significant increase in simulation time lead us to choose planet models with 15,000 particles rather than 30,000 for this project. In next section the collision parameters investigated in this project are discussed.

5.9 Collision parameters

The systems investigated in the collision simulations, as discussed in previous sections, are listed in Table 7. The systems involve a range of V_∞ equivalent to that expected in solar-like planet systems as well as hot Jupiters. A range of periapsides are investigated that range from very violent head-on collisions ($R_{\text{per}} \approx 0$ R_J), to more subtle grazing collisions ($R_{\text{per}} \approx 2$ R_J). In all simulations the planets are initiate at a separation of ten Jupiter-radii with a velocity determined by the sum of the V_∞ and the gravitational acceleration determined by Eq. (5.3).

$M_1 : M_2[\text{M}_\text{J}]$	V_∞ [km/s]	$R_{\text{per}}[\text{R}_\text{J}]$
1:1	20,60,100	0, 0.1, 0.5, 1.0, 1.5, 2.0
3:1	20,60,100	0, 0.1, 0.5, 1.0, 1.5, 2.0
5:1	20,60,100	0, 0.1, 0.5, 1.0, 1.5, 2.0

Table 7: Preliminary table of setups to be investigated in this project. M_1 and M_2 are the masses of the two planets in the collision, and V_∞ their initial velocities. R_{per} is the separation at closest encounter (periapsis) where zero is a head-on collision and 2 R_J a grazing collision, and R_{per} is the initial separation between the planets.

6 Planet collisions

We have investigated collisions between Jupiter-mass planets initiated with a range of relative velocities, masses and planet separations at impact. From the results of these we aim to determine the parameters space for which planet merge relative to this parameters.

A range of potential velocities at infinity as well as periapsides were discussed and listed in Section 5. The simulations are grouped in sets by their velocity at infinity and the mass fractions between the planets, and for each group six different periapsides where investigated. The planet models were generated using the LEQ program with a polytropic index of $n = 1$ (refer to discussion in Section 2.5).

Short summaries of the results are listed in Table 9. Full summaries of the results are listed in the tables of Appendix C, where further information is available on the collisions. The collision results will be discussed later in this section.

In the discussion and all tables the most massive planet is denoted the primary M_1 and the lower mass secondary planet M_2. The primary mass M_1 will be changed in different simulation sets, but the secondary mass is always one Jupiter mass. The initially investigated periapsis range between 0 – 2 R_J are listed in Table 7, together with the investigated values of the other collision parameters; M_1 and V_∞. Three primary masses where investigated with $M_1 = 1, 3, 5$ M_J and the properties of the planet models, generated using the LEQ program with a polytropic index $n = 1$, are listed in Table 8.

M_1 [M_J]	R [R_J]	ρ_c [g cm^{-3}]	P_c [dyne cm^{-2}]	T_c [K]
1.0	1.00	4.80	4.49×10^{13}	1.13×10^{5}
3.0	0.87	18.49	5.64×10^{14}	8.15×10^{5}
5.0	0.82	37.32	2.02×10^{15}	1.45×10^{6}

Table 8: Summary of the modeled planet properties of this project. The radii are generated using the mass-radius relationship discussed in Section 2.5.

The energy loss $\Delta E/E_0$ was defined in Section 4.2 as the difference in energy after the collision to the initial, divided by the initial energy as in Eq. (4.6). As was discussed in Section 4.2, an energy loss of $\Delta E/E_0 \leq -1$ implies that the planets have lost enough energy to become bound. In all simulations the planets then returned for another collision and eventually merged. These collisions are hence the more interesting as an alternative way to build-up planet mass.

For bound planets the return time is dependent on the initial properties of the collision and how much energy was lost in the first collision. Bound systems have a relative semi-major axis a and period P which can be determined and was discussed in Section 4. Eventually the planets in these systems will merge and form a new planet. Each collision will cause mass loss, and so bound systems with multiple

collisions will generally suffer from somewhat larger mass losses, limiting the mass of the merged planet.

In cases where the energy loss is not large enough to bind the planets ($\Delta E/E_0 > -1$) they not experience additional collisions within the time frame of the simulations. These simulations do not lead to mergers of the planets, but their structure will be altered. It can be of interest to identify any observational signatures of previous collisions in the structures of the planets. Unbound systems will still suffer from mass loss, however the amount can in general be expected to be smaller than for the bound systems.

The results are divided into a number of parts, each concentrating on specific details of the collisions starting with the determined mass losses in Section 6.1.

6.1 Mass loss

Mass loss due to collisions would be expected to increase with decreasing cross sections and impact velocities. Transforming this into parameters used to initiate the simulations implies that small periapsis and high velocities at infinity generally should result in larger mass loss. For smaller periapsides larger parts of the planets will be physically involved in the collision, and hence larger amounts of material are affected. In this section mass loss and its dependence on the initial parameters is discussed.

For head-on collision large amounts of material can be expected to be ejected, while for larger periapsides ($R_{\text{per}} \approx 2$ R$_{\text{J}}$) the planets are expected to lose less material. The collisions are inelastic such that the kinetic energy is not conserved in a closed system and instead part of the initial kinetic energy is converted into internal energy. Consider a basketball bouncing against a flat solid surface. In each bounce the basketball will lose part of its kinetic energy, causing the height of the bounce to decrease as it is converted into thermal energy.

The difference between a head-on and grazing collision is that they convert different amounts of their kinetic energy into thermal, and it is this converted energy that causes mass loss by blowing up the planets as they are heated by the extra thermal energy. Bloated planets may fill their Roche lobes and part of their material can escape, possibly accreted by the other planet.

The Roche lobe is the space around an object in which it can retain material and the space that this lobe extends to depends on the masses of the two objects and their separation. If the object would expand past this Roche lobe material would be able to escape the gravitational pull of the object but in the close vicinity of each objects the gravitational pull from the companion is negligible. The Roche lobe can be approximated as a sphere of the same volume and the approximate formula from Paczyński (1971) can be used to estimate it as:

$$\begin{aligned} \frac{R_{\text{H}}}{R_{\text{sep}}} &= 0.38 + 0.2 \log \frac{M_1}{M_2} \quad , \text{ for } 0.3 < \frac{M_1}{M_2} < 20 \\ \frac{R_{\text{H}}}{R_{\text{sep}}} &= 0.46224 \left(\frac{M_1}{M_1 + M_2} \right)^{1/3} \quad , \text{ for } 0 \ < \frac{M_1}{M_2} \ < 0.8 \end{aligned}$$

Mass ratio		V_∞ =20 km/s		V_∞ =60 km/s		V_∞ =100 km/s	
$M_1 : M_2$	$R_{\rm per}$ [R$_{\rm J}$]	$\Delta E/E_0$	$\Delta M/M_0$	$\Delta E/E_0$	$\Delta M/M_0$	$\Delta E/E_0$	$\Delta M/M_0$
1 M$_{\rm J}$:1 M$_{\rm J}$	0.0	IM	3.20×10^{-2}	IM	6.66×10^{-2}	IM	3.21×10^{-1}
	0.1	IM	2.82×10^{-2}	IM	6.50×10^{-2}	IM	3.41×10^{-1}
	0.5	–4.79	1.57×10^{-2}	–1.93	4.65×10^{-2}	–1.42	2.69×10^{-1}
	1.0	–3.82	8.87×10^{-3}	–1.10	1.86×10^{-2}	–0.430	5.15×10^{-2}
	1.5	–2.69	4.99×10^{-3}	–0.410	2.18×10^{-3}	–0.0702	6.92×10^{-3}
	2.0	–1.86	3.17×10^{-3}	–0.0910	4.52×10^{-5}	–0.0130	7.31×10^{-7}
	2.5	–0.62	0.00	–	–	–	–
3 M$_{\rm J}$:1 M$_{\rm J}$	0.0	IM	2.33×10^{-2}	IM	4.06×10^{-2}	IM	8.22×10^{-2}
	0.1	IM	2.06×10^{-2}	IM	3.86×10^{-2}	IM	9.10×10^{-2}
	0.5	–2.45	1.50×10^{-2}	–1.36	3.23×10^{-2}	–1.17	8.90×10^{-2}
	1.0	–2.21	8.62×10^{-3}	–0.880	1.04×10^{-2}	–0.442	3.56×10^{-2}
	1.5	–1.86	4.79×10^{-3}	–0.360	2.42×10^{-3}	–0.107	5.42×10^{-3}
	2.0	–1.24	1.68×10^{-3}	–0.0703	4.13×10^{-5}	–0.0157	4.43×10^{-7}
	2.5	–0.29	0.00	–	–	–	–
5 M$_{\rm J}$:1 M$_{\rm J}$	0.0	IM	2.87×10^{-2}	IM	4.55×10^{-2}	IM	7.80×10^{-2}
	0.1	IM	2.50×10^{-2}	IM	4.33×10^{-2}	IM	8.21×10^{-2}
	0.5	–2.19	2.32×10^{-2}	–1.24	3.93×10^{-2}	–1.09	1.14×10^{-1}
	1.0	–1.97	1.64×10^{-2}	–0.650	2.30×10^{-2}	–0.256	6.41×10^{-2}
	1.5	–1.72	1.19×10^{-2}	–0.316	4.52×10^{-3}	–0.0523	1.22×10^{-2}
	2.0	–1.09	6.21×10^{-3}	–0.0552	1.80×10^{-4}	–0.00512	5.10×10^{-6}
	2.5	–0.17	0.00	–	–	–	–

Table 9: Short summary of results for simulations, initiated with varying primary planet masses M_1, periapsides $R_{\rm per}$ and velocities at infinity V_∞. $\delta M/M_0$ denote the total mass loss of the system and $\delta E/E_0$ the energy loss. Instantly merging collisions are denoted by IM and energy loss cannot be determined. For the collisions initiated with $V_\infty = 20$ km/s the planets did not generate any unbound systems even for grazing collisions, so one additional collision with $R_{\rm per} = 2$ R$_{\rm J}$ was investigated, but not for larger V_∞.

where R_{sep} is the planet separation and R_{H} defines a sphere with the same volume as the Roche lobe. In the collisions part of the planets' kinetic energy is converted into thermal energy, causing them to blow up and possibly expanding past the Roche lobe. The gravitational pull of another close-by planet will shrink the Roche lobe and may allow material to be accreted.

With larger V_∞ the kinetic energy of the collision will be larger for given impact parameters. The larger energy will lead to larger mass loss as a larger amount of material may reach energies allowing them to escape the planet(s) potential well. Conversely, low velocities at infinity will lead to less mass loss as less material reaches escape velocity.

Collisions between equal-mass objects resulted in similar mass losses for the planets. The structural differences compared to the initial planet model were also similar in the cases where the planets were unbound after the collision. In these equal-mass collisions the planets will have similar Roche lobes, and as such a similar amount of kinetic energy is converted into thermal energy for both planets and the planets lose a similar amount of mass.

If one planet is more massive however the planets lose different amounts of material in the collision. Here the planets' Roche lobes will be different, where the less massive secondary planet will have greater difficulty in retaining its mass to the primary planet. Further, the primary planet's large mass allows it to effectively bind material with the result that it will have a larger Roche lobe. In the collision, the massive primary planet can hence accrete material from the secondary resulting in a significant difference in mass loss between the planets. If the secondary planet is blown up enough by the collision, it may even be completely disrupted and large amounts of material is accreted by the primary.

The results from the analysis of mass loss are divided into different sets depending on the primary planet's mass. For bound systems the planets will eventually merge, and the mass loss is given relative to the system's total initial mass, while for unbound systems the planets' individual mass losses are also given relative to their initial mass. Collisions with $R_{\text{per}} \leq 0.1$ R_J will instantly merge, as will be discussed in more detail later in Section 6.3, and often suffered less mass loss than collisions with somewhat larger periapsides.

For collisions with equal primary and secondary masses ($M_1 = M_2 = 1$ M_J), the relative mass loss is plotted in Figure 14 as a function of periapsis. In the figure, filled symbols represent bound systems, unfilled represent unbound systems and the colored lines represent the various velocities at infinity.

The results listed in Table 9 show that the planets lost similar amounts of mass for collisions where they were unbound, as was predicted. This similarity holds irrespective of V_∞ and causes the planets individual mass losses to overlap in Figure 14.

6.1.1 Equal-mass collisions

The green line in Figure 14 shows an exponential decrease in mass loss with periapsis for $V_\infty = 20$ km/s. Mass loss is expected to decrease with increasing periapsis as only

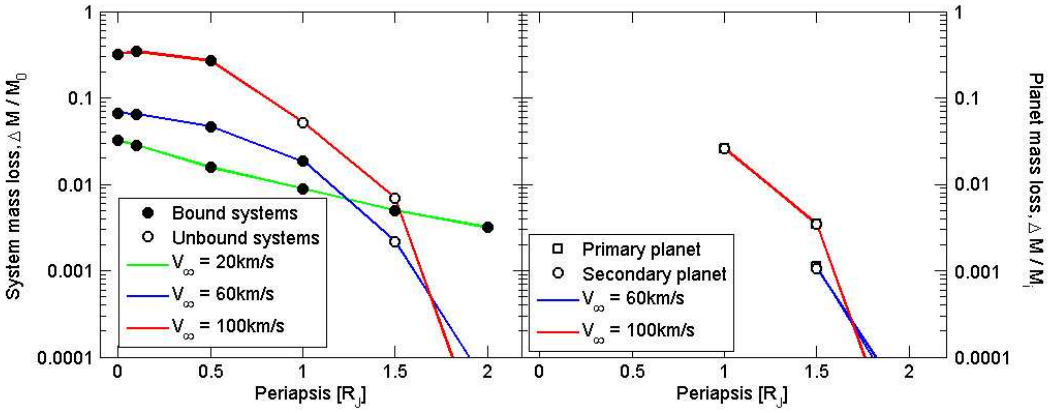

Figure 14: Mass loss for collisions between two Jupiter-mass planets for a range of periapsis and velocities at infinity. Filled symbols represent systems with bound planets, and unfilled - unbound. In the left figure the mass loss for both planets is considered, and in the right the planets' individual mass loss relative to their initiated mass. The figure is limited to mass losses down to $\delta M/M_0 = 10^{-4}$ since lower values represent insignificant losses.

the outer parts physically collides. The investigated periapsides extend out to grazing collisions $R_{\rm per} = 2.0$ R$_{\rm J}$ however for low-velocity collisions with $V_\infty = 20$ km/s any additional periapsis of $R_{\rm per} = 2.5$ R$_{\rm J}$ was also investigated as grazing collisions did not generate an unbound systems. The limiting periapsis for bound systems can be found by interpolation of two points around this limiting periapsis. This periapsis is denoted the capture radius $R_{\rm cap}$ and will be discussed in Section 6.2.

For higher values of V_∞, the dependence of mass loss with periapsis appears to steepen. At small periapsis a high V_∞ results in higher mass loss, while for larger periapsis ($R_{\rm per} \geq 1$ R$_{\rm J}$) the mass loss drops significantly. The rapid decrease in mass loss with larger $R_{\rm per}$ and V_∞ may be due to the short time of physical interaction between the planets during the collision. Therefore the interaction between the planets is more limited, and they do not have enough time to disrupt each other significantly.

The collisions between unequal-mass planets will, contrary to the collisions discussed here, result in differential mass losses for the two masses and structural differences. These unequal-mass collisions are discussed next.

6.1.2 Unequal-mass collisions

Mass loss has been plotted as a function of periapsis for collisions with a primary planet mass $M_1 = 3$ M$_{\rm J}$ in Figure 15 and for a primary planet mass $M_1 = 5$ M$_{\rm J}$ in Figure 16. Properties of the two models are listed in Table 8 and the differences in radius and density between the planets can be seen.

In the left plot of Figure 15 the total mass loss of the systems is plotted as a function of periapsis, and in the right plot the planets' individual mass losses are

given with respect to the their respective initial mass. The secondary planet loses a significantly larger amount of mass than the primary in the collision, due to its lower mass. The deeper potential well of the primary planet, allows it to bind material more efficiently than the secondary planet, resulting in a systematically smaller mass loss. This divergence is expected to increase with an increasing mass of the primary planet.

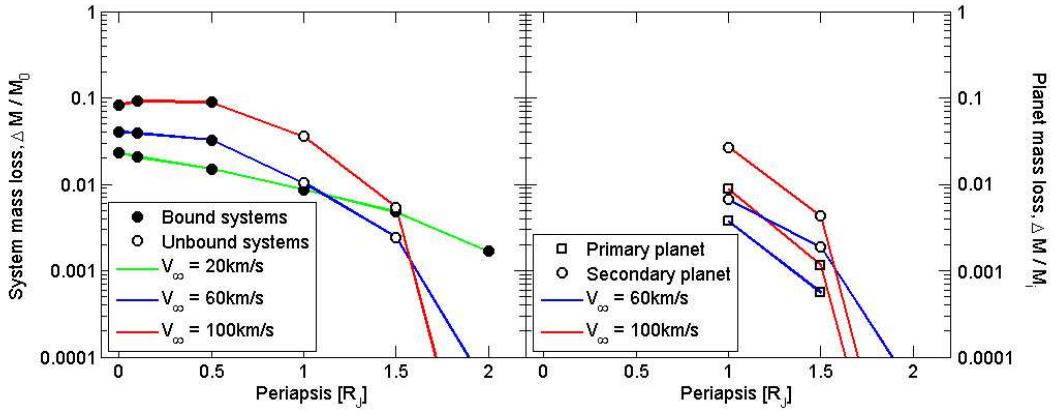

Figure 15: Mass loss for collisions between two planets of unequal mass, primary planet mass $M_1 = 3$ M_J and secondary $M_2 = 1$ M_J, for a range of periapsis and velocities at infinity. Filled symbols represent bound systems, and unfilled for the unbound. In the left figure is the systems total mass loss considered, that is the total loss of both planets, and in the right the planets' individual mass loss.

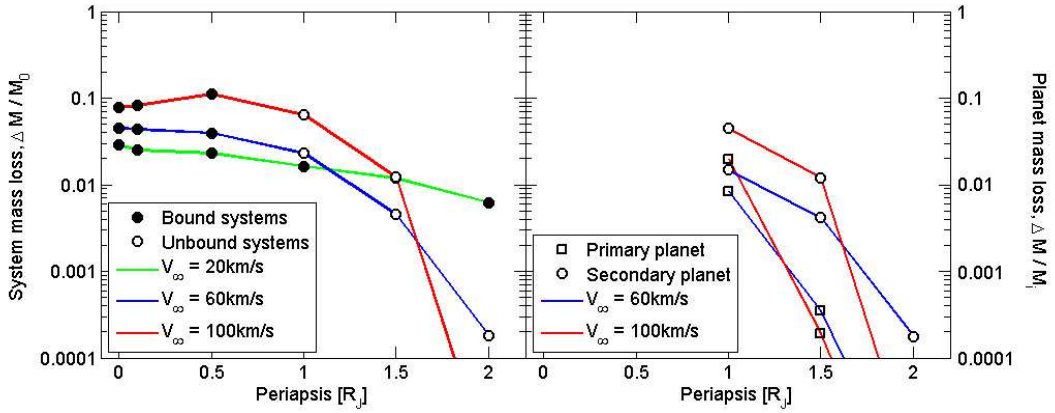

Figure 16: Mass loss for collisions between two planets of unequal mass, primary planet mass $M_1 = 5$ M_J and secondary $M_2 = 1$ M_J, for a range of periapsis and velocities at infinity.

Similarly for collisions between two Jupiter-mass planets, the low velocity runs with V_∞= 20 km/s show an exponential decrease of mass loss with periapsis in Figure 15. The same is evident in Figure 16 for a primary planet mass $M_1 = 5$ M_J.

As expected, larger velocities at infinity and smaller periapsides result in larger mass losses, as larger velocities can eject more of the planets' material as more energy is available in these collisions. With smaller periapsides more material is involved in the collision that can be ejected. This is the same general dependence as the equal-mass collisions showed in Figure 14 and show that this behavior is not significantly dependent on the mass ratio of the planets.

For the smallest periapsis $R_{\rm per} = 0$ $\rm R_J$ and $R_{\rm per} = 0.1$ $\rm R_J$ the planets appear to instantly merge during the collision. For larger periapsides the dominating potential well of the primary planet may cause significant damage to the secondary planet. As the planets pass each other the primary's potential well is strong enough in a few cases to almost completely disrupt the secondary planet, and allows the primary to accrete large amounts of the material afterwards. For the collisions with periapsis $R_{\rm per} = 2$ $\rm R_J$ the planets barely have any contact resulting with insignificant amounts of mass and energy loss.

In the next section the capture radius is discussed. This is the radius at which planets will be bound after a collision, and depends on the velocity at infinity and masses of the planets.

6.2 Capture radius

As discussed previously in Section 4, planets may lose enough energy in the collision to become bound to each other. This energy loss, previously discussed in Section 4, is denoted $\Delta E/E_0$ where E_0 is the initial energy, determined by the kinetic energy with a velocity defined at an infinite separation (V_∞).

Determining the periapsis at which the planets would be barely bound, where $\Delta E/E_0 = -1$, is an interesting parameter. Determining it through additional simulations would take too much time. Instead, looking at the behavior of the energy loss with periapsis, the capture radius can be found by estimating the intersection of $\Delta E/E_0 = -1$.

A decrease of the capture radius with larger V_∞ is expected, as energy loss is expected to decrease with periapsis. For the same reason, $R_{\rm cap}$ is expected to be greater for smaller V_∞, as these systems require less energy loss to become bound.

Determined values of the energy and mass losses are listed in the summary Table 9. Values are listed for all investigated periapsis, except the cases where the planets merge instantly ($R_{\rm per} \leq 0.1$ $\rm R_J$).

Davies et al. (1991) discuss that the tidal dissipation energy is strongly dependent on the objects' separation. They studied collisions between a 0.8 $\rm M_\odot$ red giant and a impactor mass 0.4 and 0.6 $\rm M_\odot$, where the impactor is treated as a point mass and assumed to be a white dwarf or main-sequence star. The impactor passing by the red giant will induce a tidal oblateness of the red giant. The energy associated with this oblateness is $E_{\rm tidal} \simeq (GM_{\rm RG}M_{\rm env}/R_{\rm RG})\epsilon^2$ where $M_{\rm RG}$ is the object mass, $M_{\rm env}$ the envelope mass and $R_{\rm RG}$ the red giant radius. ϵ is the induced oblateness of the red giant scaling to the object separation $R_{\rm sep}$ as $\epsilon \propto R_{\rm sep}^{-3}$. At the point of closest

approach R_{per} the energy associated with the tidal bulge is expected to scale as:

$$E_{\text{tidal}} \propto R_{\text{per}}^{-6} \tag{6.1}$$

This is expected for larger periapsis, as Davies et al. (1991) state that the tides raised will be in the non-linear regime for smaller values of R_{per}, and the relation in Eq. (6.1) will not hold.

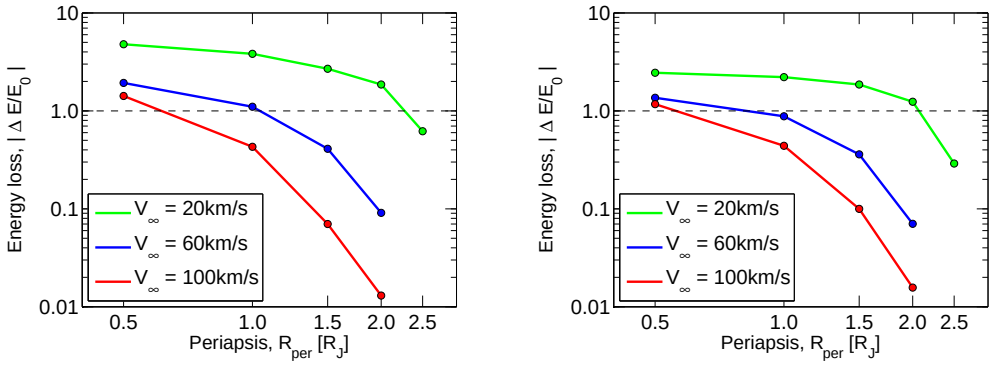

(a) Primary mass $M_1 = 1$ M$_\text{J}$.

(b) Primary mass $M_1 = 3$ M$_\text{J}$.

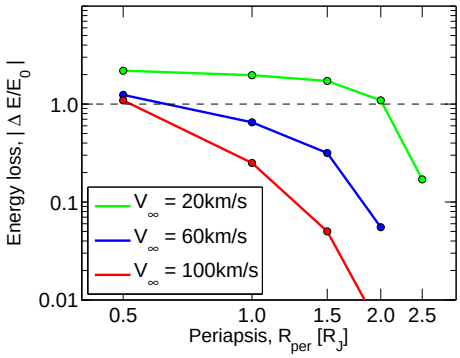

(c) Primary mass $M_1 = 5$ M$_\text{J}$.

Figure 17: Energy losses for different simulation sets with varying primary masses M_1 and a range of periapsis R_{per} and velocities at infinity V_∞. In the upper box the expected behavior of the decline for larger periapsis has been plotted from Davies et al. (1991). Errors in the energy losses are determined from the errors in the in the energy conservation E_{err} which are too small to be visible in the figure, but are listed in Appendix C.

In Figure 17 the determined energy losses have been plotted as a function of periapsis. The limiting energy loss between bound and unbound systems is drawn in the plots for and the expected behavior of the energy loss with periapsis as from Eq. (6.1) is shown in the upper box.

The energy loss decreases with an increasing mass of the primary planet in Figure 17. Comparing simulations of equal- and unequal-mass systems, the general

dependence of energy loss with periapsis appears the same, however the energy losses are lower with larger primary planet mass. The same divergence in energy loss behavior is found when comparing the two unequal-mass simulation sets.

For the low velocities at infinity, the capture radius is large enough that it can be expected to follow the behavior from Eq. (6.1). Hence, it can be determined through interpolating of the two points around the limit $\Delta E/E_0 = -1$ with the equivalent relation $\Delta E/E_0 \propto R_{\rm per}^{-6}$. For larger V_∞ the energy losses in the region of the planets' capture radius will diverge from the expected behavior, instead the capture radius is calculated through a linear interpolation.

M_1[M$_{\rm J}$]	V_∞ [km/s]		
	20	60	100
1	2.28 R$_{\rm J}$	1.06 R$_{\rm J}$	0.62 R$_{\rm J}$
3	2.13 R$_{\rm J}$	0.83 R$_{\rm J}$	0.57 R$_{\rm J}$
5	2.05 R$_{\rm J}$	0.62 R$_{\rm J}$	0.54 R$_{\rm J}$

Table 10: The resulting capture radii for different V_∞ and M_1, as determined from interpolation of data points close to the boundary $\Delta E/E_0 = -1$.

The capture radii are listed in Table 10, and show a decrease with larger V_∞ but also with increasing mass of the primary planet. In the next section, typical examples of different collision types are presented and discussed.

6.3 Collision types

Four specifically interesting categories of collisions where identified from the simulations; violent, grazing, disrupting, and returning collisions. Typical examples of these categories are presented and discussed in this section. For each of the examples nine frames with density maps are plotted. Each frame is specifically chosen to visualize the evolution of each simulation. In order to see the structural differences arising from the collision only central slices of $|z| \leq 0.2\ R_J$ are plotted in the figures, revealing the density profile of each planet. Collisions with large V_∞ are discussed first, where the high energies involved causes significant structural damage to the planets.

6.3.1 Violent collisions

Investigated collisions with large V_∞ will create a violent collision where large amounts of material may be ejected and significant damage caused to the interior structure of the planet remnant(s). The large V_∞ allows the planets to remain unbound after the collision unless the planets collide with a small enough periapsis to generate significant energy losses to bind the planets. One subcategory of violent collisions where found where planets initiated with very small periapsides $R_{\rm per} \leq 0.1$ R$_{\rm J}$ instantly merged.

Normally two planet remnants can be distinguished after the collision, however for collisions with small periapsides ($R_{\rm per} \leq 0.1$ R$_{\rm J}$) the planets instantly merge as the gravitational pull becomes very strong due to the small separation. Even simulations with large velocities at infinity are unable to escape this fate. In these collisions large amounts of material where ejected. Part of this material might be accreted by the merged planet, but some will escape the system.

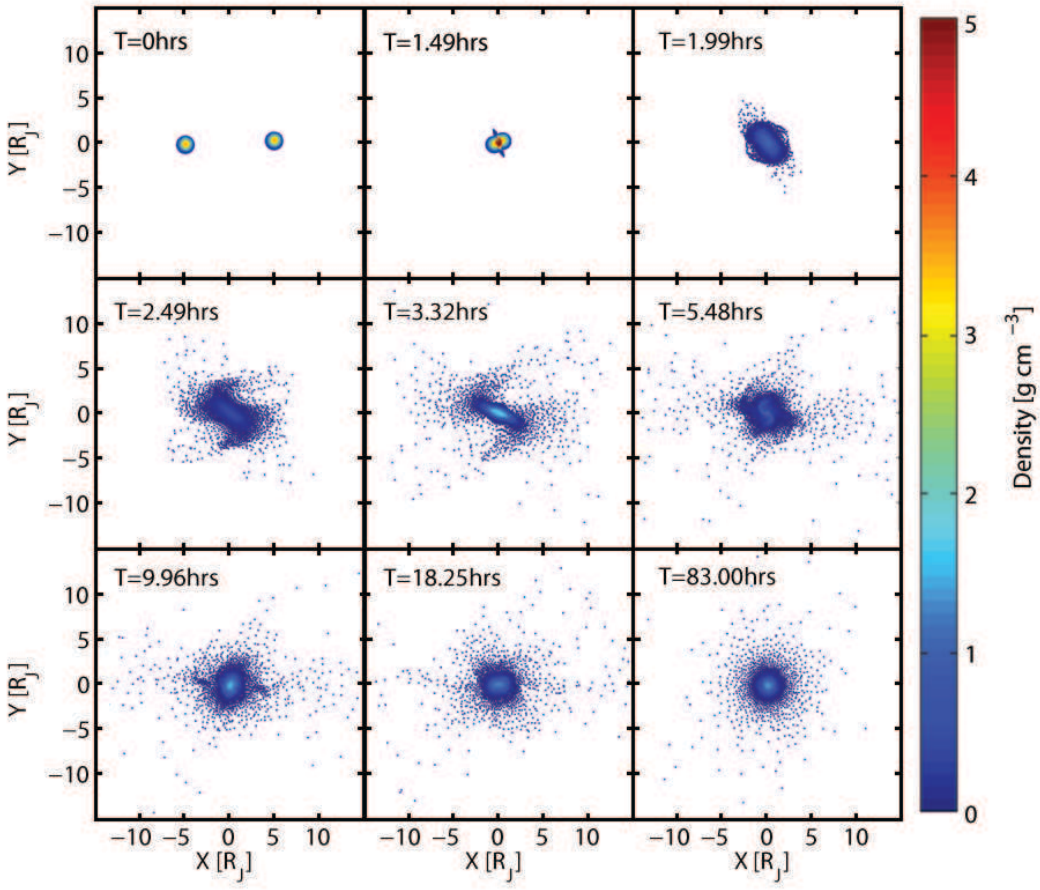

Figure 18: Example of a highly energetic collision with small periapsis such that the planets instantly are caught in each others' potential well and rapidly merge. The simulation was initiated with two Jupiter-like planets, with a velocity at infinity of $V_\infty = 60$ km/s and periapsis of $R_{\rm per} = 0.1$ R$_{\rm J}$.

Snapshot frames of a typical example run of an instant merger is plotted in Figure 18. The collision was initialized with two Jupiter-mass planets with initial velocity at infinity of $V_\infty = 60$ km/s and periapsis $R_{\rm per} = 0.1$ R$_{\rm J}$. The planets make first contact 1.49 hours after initiation of the simulation. Quickly after contact the planets are caught in each other's potential well due to the small separation and merge instantly. Large amounts of material are ejected in the collision, of which some

remains bound and accreted by the merged planet. After approximately 16 hours the planet has accreted much of the bound material, and has retained an elongated form.

Approximately 50 hours after initialization the merged planet has stabilized. It has then accreted some debris material, allowing it to grow both in size and mass after the collision. A majority of the mass is bound to the merged planet, of which some $\sim 10\%$ forms a debris cloud that encases the planet.

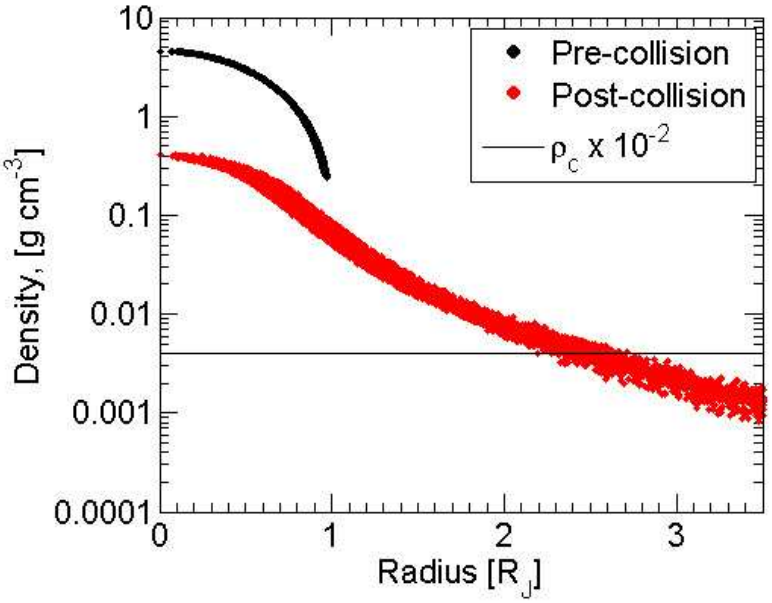

Figure 19: Density profile of the planet model before and after collision for a simulation initiated with $M_1 = 1$ M_J, $V_\infty = 60$ km/s and $R_{per} = 0.1$ R_J. The black points give the density profile of the planet model before the collision, and the red points as it has relaxed after the collision. In this project the planet radius after the collision is defined as the radius at which the density has decreased by two orders of magnitude from the core density of the initial model.

In Figure 19 the density of the planet has been plotted as a function of its radius. There is a difficulty in determining the exact boundary where the planet itself ends and the low-density debris cloud begins. In this project the radius of a planet after the collision is defined as the point at which the density has dropped two orders of magnitude from the core density. This way, the planet has a approximate radius of 2.4 R_J. If the planet is left alone, the debris cloud remains stable, but would eventually dissipate due to disturbing external forces from the host star or the other planets in the planetary system.

Even though observable signatures exist from the debris disc, these types of collisions will be unlikely compared to the collisions with larger periapsides. From the large increase in radius compared to the increase in mass, the planet will have

notably lower density. The central regions reach at most 1.73 g cm^{-3}, and the average density of the planet is 0.143 g cm^{-3}. This is a significant decrease compared to the initial values of the Jupiter models, as listed in Table 8. The planet closest to this average density is Saturn with an average density of $\bar{\rho} = 0.7$ g cm^{-3} (Hamilton 1995), the smallest value of the planets in the Solar system. There is no evidence that Saturn has previously been involved in a collision, and its low density is determined to come from its composition which is mainly gas. The other gas giants in the solar system are also gaseous, but Jupiter is so massive that its inner regions are very compressed. Uranus and Neptune are instead so cold that their inner regions are frozen solid (Fortney & Nettelmann 2009).

After the collision, the planet is in a state similar to a planet just formed from a protoplanetary disk. The cooling time for such a planet will depend greatly on the structure of the planet, specifically its mass and radius, but also composition. Baraffe et al. (2010) discussed our current knowledge of the physical properties of exoplanets. They determined the cooling and contraction time for Jupiter-mass planets with a range of different models and the characteristic thermal time scale for planet contraction $\tau_{\rm KH}$, called the Kelvin-Helmholtz timescale, is determined by:

$$\tau_{\rm KH} \sim \frac{GM^2}{RL} \tag{6.2}$$

Jupiter, at the beginning of its evolution with a luminosity $L \sim 10^{28}$ erg s^{-1}, will have a relatively short time scale of $\tau_{\rm KH} \sim 10^7$ years while with a luminosity $L \sim 10^{25}$ erg s^{-1} at an age of 1 Gyr the planet will take significantly longer time with $\tau_{\rm KH} \sim 10^{10}$ years. For planets in tight orbits the timescale will increase due to the induced thermal energy from the proximity of the host star. It would take an excessive amount of time to simulate the collisions until the bound material of the planets settle with these expected time scales. Therefore we only mention that reasonable time scales for the planets to fully settle are in the range of $\sim 10^{10}$ years.

A recent discovery by Anderson et al. (2010) revealed the planet WASP-17b with an ultra-low density, with an estimated mass of 0.3 $M_{\rm J}$ and radius $1.5 - 2$ $R_{\rm J}$ giving it an average density of $0.046 - 0.11$ g cm^{-3}. The low density of WASP-17b is not predicted to have been caused by a collision however. They suggest that tidal heating from recent or ongoing tidal circularization might cause the planet to bloat, with a low density as a result. Many other of these bloated planets have been observed, and most if not all have the characteristics of hot Jupiters, with tight orbits in which tidal forces exerted by the host star become significant.

Collisions initiated with large V_∞ require a small periapsis in order to become bound and merge and are very unlikely compared to grazing collisions, as results in Section 5.7 showed. As was also discussed, collisions with large V_∞ are most likely for planets orbiting their host star in a tight orbit, with a resulting large orbital velocity. As gas giants form a few au from the host star, the planets need to move into tighter orbits after formation for them to have large orbital velocities consistent with the larger V_∞.

As the results in Section 5.5 showed, collisions in unstable planetary systems with multiple Jupiter-like planets in tight orbits are very likely. The determined capture radii for such systems in Section 6.2 showed that the planets are required to collide with such small periapsides however that the probabilities for such collisions to result in mergers may be improbable. The violent collisions may still invoke considerable damage on the planets, especially if one of the planets is more massive (discussed in more detail in Section 6.3.3). The low density planets may be possible to observe, but they would be difficult to distinguish from bloating effects due to proximity to the host star.

6.3.2 Glancing and unbound collisions

Collisions with large periapsides will only have limited physical contact, resulting in small mass and energy losses. This will not be enough to bind the planets after the collisions, and hence no mergers occur. Collisions with large periapsides are the most probable, as was discussed earlier in Section 5, however they do not normally lead to mergers. The only exception to this are collisions initiated with the lowest $V_\infty = 20$ km/s, which have such a low initial energy that they easily become bound. An example of these collisions that later merge are later discussed in Section 6.3.4.

In Figure 21 snapshot frames for different time steps of a typical grazing collision have been plotted. The system was initiated with two Jupiter-mass planets, $V_\infty =$ 60 km/s and $R_{\text{per}} = 1.5$ R_J. The two planets have first physical contact after approximately 1.49 hours from initiation of the simulation, and 4 hours later the planets have reached a separation of approximately 10 R_J, and lost only a minor amount of mass. The tidal interaction has caused the planets to become elongated and they have begun to slowly rotate as a result of interaction during the collision. As the planets move further away, they begin to stabilize and retain once again a spherical form after approximately 9 hours while still rotating.

The density of the two planets after the collision has been plotted as a function of the planet radius in Figure 21. Only small changes are apparent in the density profile of the planets, but a cloud of low-density material engulfs the planets. This is similar to the example of an instant merger discussed in the previous section, however the debris is smaller with a small mass compared to the planet of $\sim 1\%$. Using the same definition for the new radius of the planets as in the previous section, the planet radii have increased somewhat, but less compared to the result of instant mergers. With a determined radii for the two planets of 1.15 R_J and insignificant changes in planet masses, the average density decreases to 0.719 g cm^{-3}. This can be compared to the initial model's $\bar{\rho} = 1.63$ g cm^{-3} or Saturn's $\bar{\rho} = 0.7$ g cm^{-3}.

As the planets are unbound they continue to increase their separation after the collision. Their orbits have however changed. A small deflection angle close to 45° is evident after the collision. This will alter the planets' orbit and may leave them in more eccentric orbits. The large eccentricities increases the probability for further close encounters and collisions with planets, or it might send any of the planets into the host star or eject them from the systems.

These types of collisions involve large periapsides, which are more probable. However, the weak interaction results in an insignificant difference in the planet structures. Collisions with larger V_∞ will however merge also at large periapsides. Similar to the instantly merging collisions discussed above, the planets both have a debris disk around them which may be observable. Considering the two planets in orbit around a host star, possibly with other planets, this disk may dissipate due to the other planets' or the host star's gravitational pull. Since the planets do not lose enough energy in the collision to become bound, the collision results in no build-up of planet mass, but rather a small decrease in mass, minor structural distortions and a debris disk.

6.3.3 Disrupting collisions

Two of the simulation sets involved collisions of unequal-mass planets and the results of these are found in Table 9 for primary planet mass 3 M_J or 5 M_J. As was

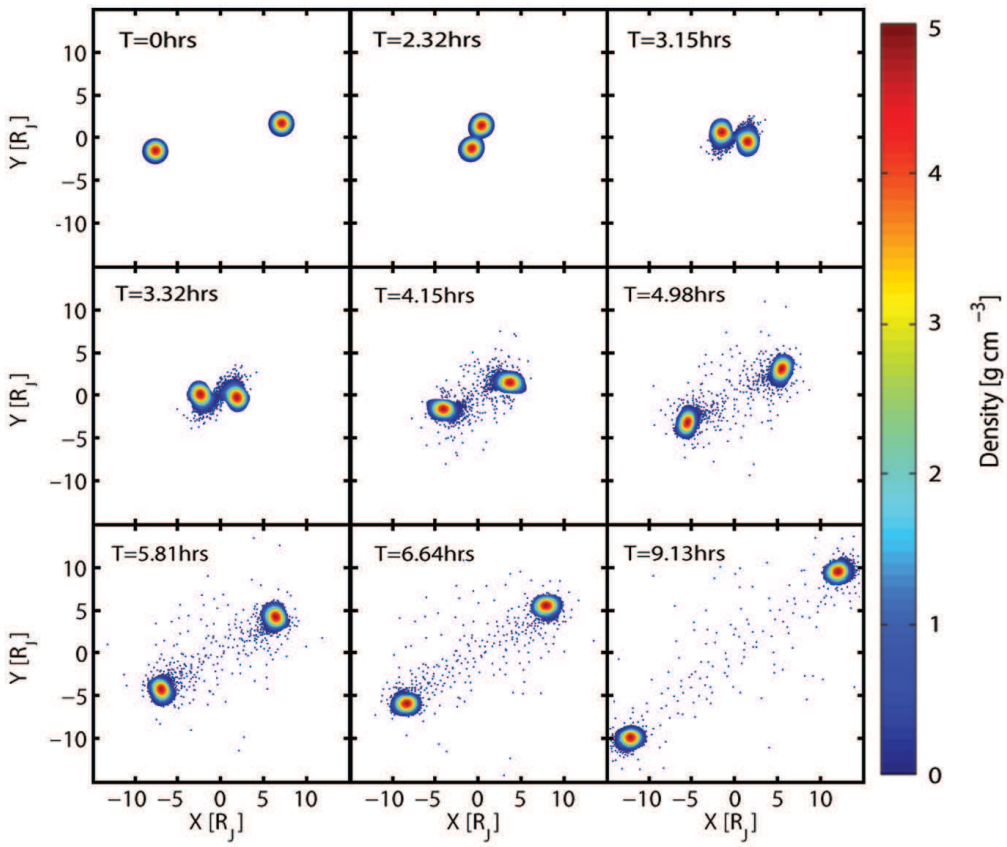

Figure 20: Example of a grazing collision. The simulation was initiated with two Jupiter-like planets, a velocity at infinity of $V_\infty = 60$ km/s and periapsis of $R_{\rm per} = 1.5$ R_J.

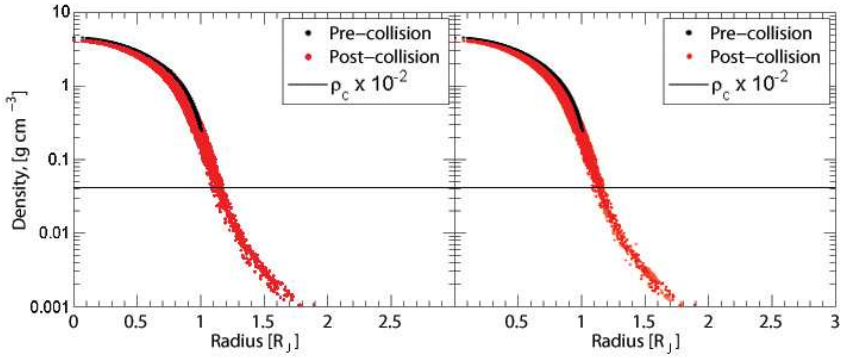

Figure 21: Density profile before and after collision of a grazing simulation with initial parameters $M_1 = 1$ M_J, $V_\infty = 60$ km/s and $R_{per} = 1.5$ R_J. The figure shows the density profiles of the two planet remnants from the collision.

discussed in the context of mass losses for collisions between planets of unequal mass in Section 6.1.2, the more massive planet will be able to accrete larger amounts of material from the secondary due to its larger Roche lobe. As the planets get closer, the primary might be able to tidally disrupt the secondary, stripping it of large amounts of mass, causing significant damage to its interior structure. With a larger fractional mass of the planets, and decreasing periapsis, this damage would be expected to increase and the primary might even be able to completely disrupt the secondary planet.

Snapshot frames of a typical example of a disrupting collision are plotted in Figure 22. The simulation was initiated with two unequal-mass planets, the primary with a mass of $M_1 = 3$ M_J and collisional parameters $V_\infty = 60$ km/s and $R_{per} = 1.0$ R_J. The planets have first physical contact 1.49 hours after the simulation is initiated and the structural differences are evident between the two planets at this point from the density mapping. Large parts of the planets are physically involved in the collision due to the small periapsis, which will result in larger mass and energy losses.

With a stronger pulling force due to the potential well, especially with the small periapsis, the primary planet is able to disrupt parts of the secondary planet. The secondary planets moves close to the primary and begin to experience the strong forces that causes significant structural damage and are almost strong enough for the secondary to be completely disrupted. After the collision a tail of material forms after the primary planet, and a small remnant of the secondary escapes the primary.

While the secondary planet is almost completely disrupted from the collision, the primary planet has lost only a smalla amount of mass in the collision but is also able to accrete some of the disrupted material from the secondary planet. The amount of mass lost will depend on the collisional parameters that the simulation is initiated with; M_1, M_2, V_∞ and R_{per}. Both planets will be affected by the collision, the secondary however lose significantly more mass in the collision for two reasons: (1) the stronger forces exerted by the primary (2) the smaller mass is less efficient

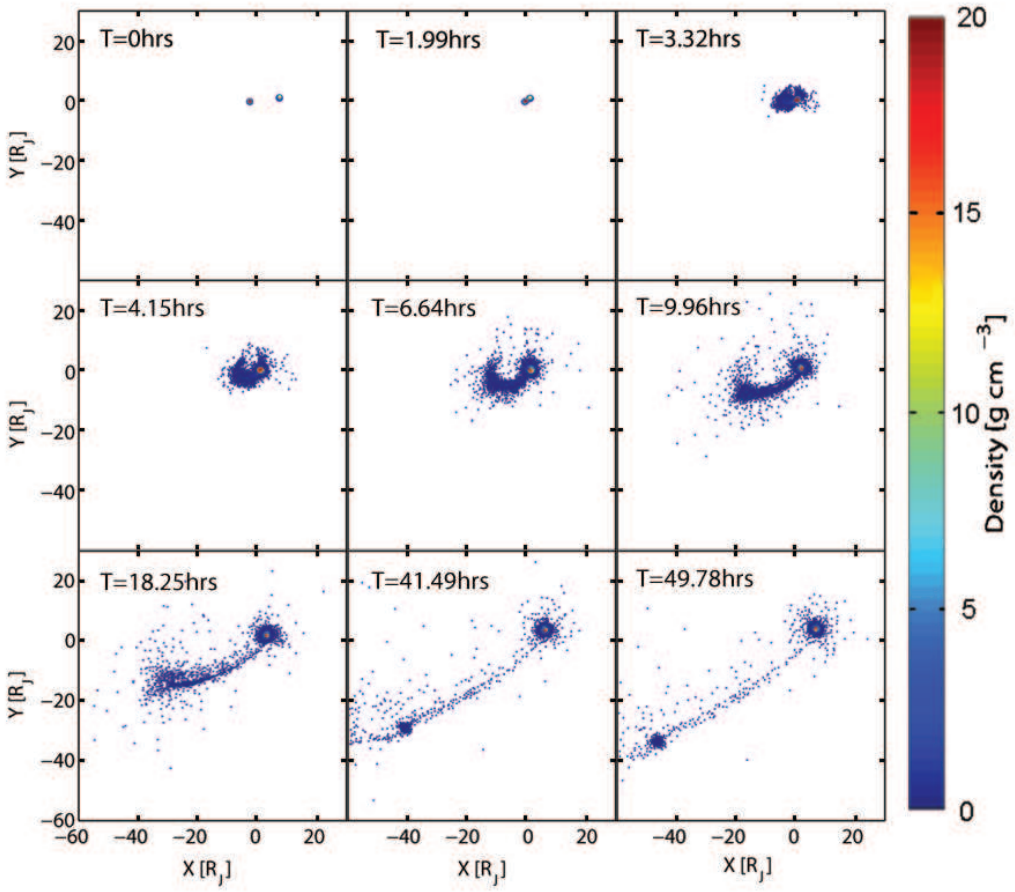

Figure 22: Example of a unequal-mass collision where the primary's tidal forces is strong enough to disrupt parts of the secondary planet. The simulation was initiated with primary planet mass $M_1 = 3$ M_J, with a velocity at infinity of $V_\infty = 60$ km/s and periapsis of $R_{\rm per} = 1.0$ R_J.

at binding material after the collision.

The density profiles are plotted in Figure 23 for the two planets before and after the collision, the primary to the left, and the secondary to the right. The primary planet has lost some material, and this has resulted in a small decrease in the density of the inner regions, while a large amount of low-density material engulfs the planets in the form of a debris cloud.

This type of collisions will not result in any significant build-up of planet mass, since the primary planet lose a comparable amount of mass to what it is able to accrete from the disrupted material of the secondary. Apart from the debris cloud engulfing the primary planet, the massive planet often show no significant structural differences. The secondary planet is however disrupted in many cases. This may be observed as large amount of unbound mass, or a smaller planet with an age

inconsistent with the other planets of the system.

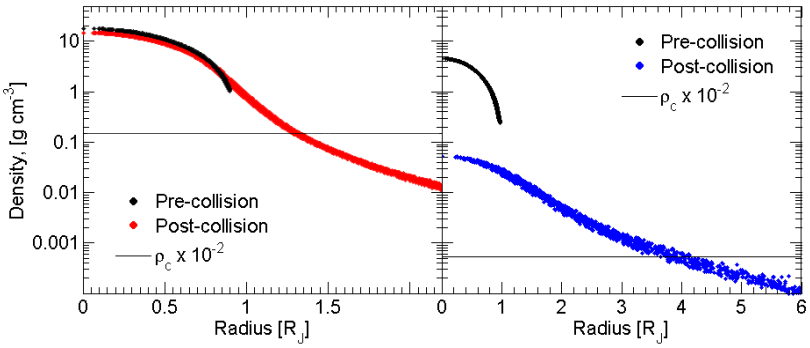

Figure 23: Density map for before and after collision of a disrupting simulation with $M_1 = 3$ M_J, $V_\infty = 60$ km/s and $R_{per} = 1.0$ R_J. The density profile of the primary planet is plotted in the left figure, and the secondary in the right.

6.3.4 Bound systems with additional collisions

In some cases the planets might lose enough energy to become bound without instantly merging from the collision. These collisions will diverge from the instantly merging collisions in Section 6.3.1 such that the conservation of angular momentum will cause the merged planet to rotate significantly.

All collisions investigated that generated bound planets returned for another collision rather than generate a binary planet. These planets will require some time to return. This return time will depend on the fractional energy loss from the initial value, as it determines how tightly bound the planets are. For large fractional losses the planets will be tightly bound, possibly even so tight that the planets' center of mass are situated inside the planet's radius. The return time will be small for the extreme example above. For smaller fractional losses, such that $\Delta E / E_0 \approx -1$, the planets will only just be bound and the return time will be extremely long.

The merging collisions are the most promising alternative to build up planet mass from standard formation theory. Collisions with small $V_\infty = 20$ km/s are especially promising as these may merge even for larger periapsides which are more likely (see discussion in Section 5), and these suffer from the smallest mass losses of the investigated collisions. The return time for the planets may be long, and determination of this time was discussed previously in Section 4, where the period of the binary system is determined through its semi-major axis.

In Figure 24 snapshot frames of a typical simulation with the planets bound after the collision has been plotted. The system was initiated with two Jupiter-mass planets, $V_\infty = 20$ km/s and $R_{per} = 1.5$ R_J. 4.31 hours after initializing the simulation, the two planet have first physical contact. Same as for the typical example of a grazing collision, presented previously in Section 6.3.2, the planets start to rotate and become elongated shortly after the collision. A stripe of ejected material form

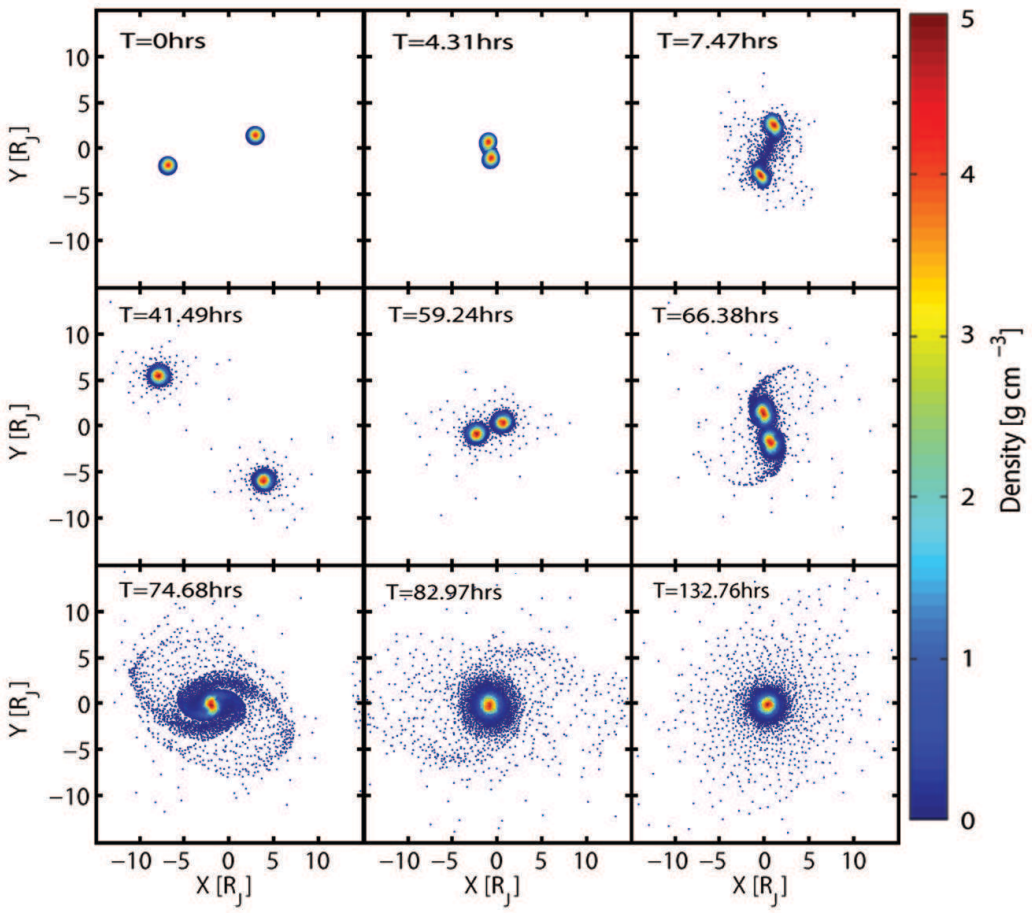

Figure 24: Example of a collision where the planets lose enough energy to become bound and return for additional collision until they eventually merge. The simulation was initiated with two Jupiter-like planets, with a velocity at infinity of $V_\infty = 20$ km/s and periapsis of $R_{\rm per} = 1.5$ $\rm R_J$.

between the planets as they increase their separation. Approximately 41.5 hours after initialization the planets reach the maximum separation and return for another collision.

The planets collide for the second time 59.2 hours after initialization and the system becomes even tighter due to further energy loss. After the second collisions, the planets' center of mass begin to spiral in, ejecting material as the travel deeper into each other's potential well. Approximately 15 hours later the planets merge, and have more or less stabilized after an additional $\sim$ 50 hours.

In Figure 25 the density profile for the merged planet has been plotted and compared to the density profile of a relaxed Jupiter-mass model. Using the same definition for the radius of the planet, it has increased to $\sim$ 1.6 $\rm R_J$ together with

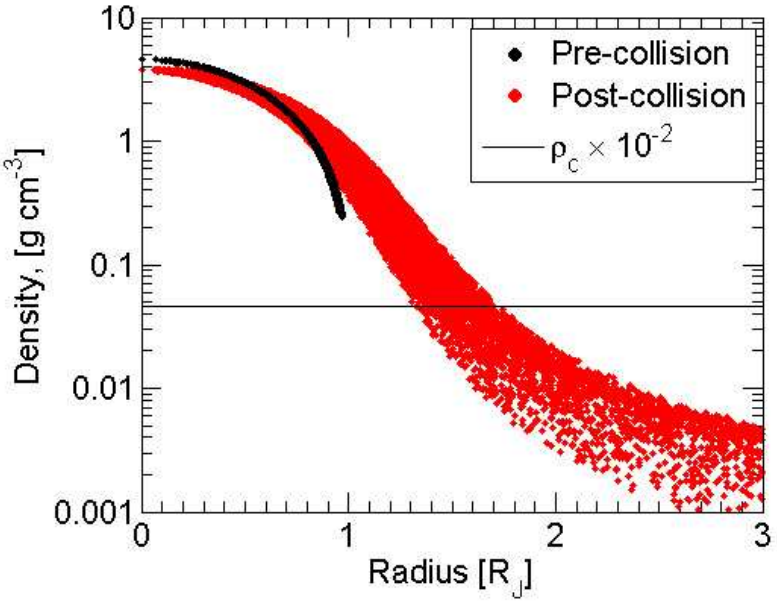

Figure 25: Density profile for before and after collision where the planets return for additional collisions, initiated with $M_1 = 1$ M_J, $V_\infty = 20$ km/s and $R_{per} = 1.5$ R_J.

an increase in mass to $\sim$ 1.5 M_J the planet's density has decreased. The density at the center has decreased to 3.58 g cm^{-3}, while the average density has dropped even more to 0.477 g cm^{-3}. Comparing the density profile to the initial model, the drop is generally in the central regions while the density has increased somewhat instead toward the surface.

The collisions initiated with $V_\infty = 20$ km/s appear to be the most plausible to result in merging planets. The V_∞ is low enough for the planets to easily become bound after the collision, even for glancing collisions. These low V_∞ are expected for planets orbiting their host star in wide orbits, with resulting low orbital velocities. The longer orbital periods of these planets result in a smaller collision probability $\sim 10\%$ compared to tight systems $\sim 60\%$ (see discussion in Section 5.5). However, since the planets merge for the full range of investigated periapsides, from head-on to grazing collisions, the total probability might be comparable or maybe larger compared to collisions with larger V_∞. Hence collisions with low V_∞, most possibly resulting from collisions occurring in wide systems, may be the best candidate of merging collisions that result in a build-up in mass.

6.4 Bound systems

A number of the investigated collisions resulted in bound systems where the planets in all cases returned for additional collisions until they finally merged. Whether the planets lose enough energy in the collision will depend on the collisional parameters

which the planets are initiated with. Requirements for mergers can be extracted from the results discussed previously of the energy losses and capture radii.

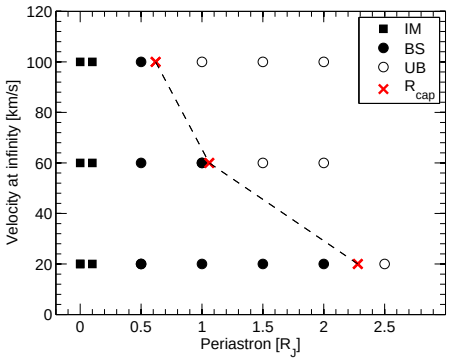

(a) $M_1 = 1$ M$_\mathrm{J}$

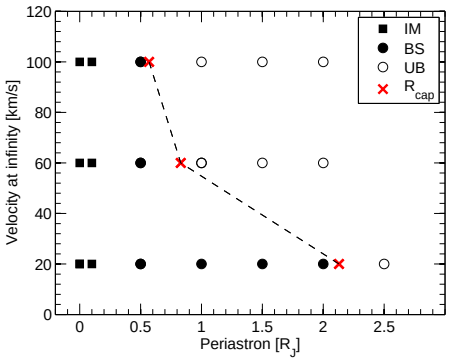

(b) $M_1 = 3$ M$_\mathrm{J}$

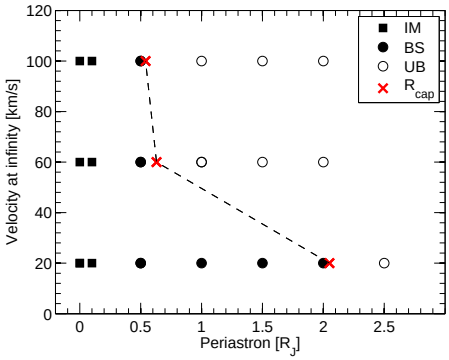

(c) $M_1 = 5$ M$_\mathrm{J}$

Figure 26: Bound and unbound systems for simulation set with collisions of two planets for a range of periapsis and velocities at infinity. The secondary, lightest planet, has a mass that of Jupiter's, while the primary is different between the three figures. The left figure shows results from equal-massed systems with two Jupiter-massed planets. In the middle figure the primary planet's mass is 3 M$_\mathrm{J}$, and in the right 5 M$_\mathrm{J}$.

The dependence of merging collisions to the collisional parameters is shown in Figure 26, where V_∞ is plotted as a function of R_per and for different primary planet masses. The filled squares represent systems that have instantly merged, as discussed in Section 6.3.1, while filled and unfilled circles represent bound and unbound systems respectively. The filled symbols represent merged systems and are of interest in the context of planet mass build-up. In the figure, the capture radii (as determined in Section 6.2) are plotted as red crosses.

There is a significant difference between collisions initiated with small velocities at infinity ($V_\infty = 20$ km/s) and systems with larger velocities ($V_\infty = 60, 100$ km/s). Low-velocity collisions become bound and merge even when initiated with large

periapsides, which result in small mass and energy losses. For larger V_∞ the planets have to collide with small periapsides in order to become bound, since the initial energy E_0 is larger and more energy needs to be lost. The fractional mass between the planets also affects the results of the collisions, since the larger mass of the primary can bind more material after the collision and less energy is lost. The effects of increasing the primary planet mass is barely notable in the determined capture radii plotted in Figure 26 for collisions initiated with $V_\infty = 100$ km/s, while more notable the lower V_∞ is.

The mass loss, as determined in Section 6.1, generally increases with increasing V_∞ and decreasing R_{per}. Grazing collisions result in insignificant amounts of material lost, with $> 99\%$ of the system's material bound to the merged planet, while head-on collisions resulted in a mass loss in the range of $\sim 10\%$. The more massive planets are able to retain more material in the collisions while possibly able to accrete more material from the secondary as well. This causes the mass losses to diverge for the two planets in the unequal-mass collisions as was discussed in Section 6.1.2, and the difference increases with the larger fractional mass of the planets.

7 Conclusions

We have investigated the outcome of collisions between Jupiter-like planets initiated with a range of masses, velocities at infinity and periapsides. Planets may lose enough energy in collisions to become bound and eventually merge. Mergers are likely to result in a build-up of planet mass which is of interest as an alternative path of planet mass build-up together with the standard formation theory for planets. As has been discussed in previous sections, the outcomes of the collisions can vary significantly depending on the parameters of the simulation, and the aim has been to quantify the parameter space resulting in bound systems.

The collision probabilities discussed in Section 5.5 were determined through N-body simulations of three Jupiter-mass planets. Apart from the instability expected in young planetary systems (Wetherill 1990) instability may be induced by external perturbations, such as stellar fly-bys. Unstable planetary systems are much more likely to host collisions compared to stable systems like our Solar system (predicted to be stable on scales of hundred millions of years by Batygin & Laughlin (2008)).

Results of the N-body simulations show that planets initiated in Jupiter-like orbits will be less likely to host a collision compared to tight planetary systems. Planetary systems with gas giants in tight orbits are consistent with the many observed hot Jupiters, and the close orbits may over time induce enough instability to cause collisions. The wide systems are sensitive to external perturbations induced by fly-bys, and may cause these systems to be unstable enough to generate significant collision probabilities.

The collisional parameters M_1, V_∞ and R_{per} affect the outcomes of the collisions differently. Large V_∞ result in violent collisions where large amounts of material may be ejected. Increasing the mass of the primary planet will allow it to retain more

material after the collision but also accrete some material from the secondary, while the secondary planet may lose orders of magnitudes more mass,

Collisions most likely to result in mergers are those initiated with small $V_\infty = 20$ km/s or small $R_{\text{per}} \leq 0.5$ R_J. Planets initiated with low $V_\infty = 20$ km/s merged even for grazing collisions, which resulted in insignificant amounts of mass loss, while planets initiated with $V_\infty \geq 60$ km/s required $R_{\text{per}} < 1.0$ R_J for the planets to merge. The planets initiated with low velocities are the most probable to eventually merge as this is possible for a range of periapsides including grazing which are the most probable (see discussion in Section 5.7). These collisions would dominantly occur in planetary systems with planets on orbits.

There are two possible observable features post-collision; the low-density cloud engulfing the planet(s) and low-density planets resulting from violent collisions. Most of the collisions investigated in this project showed signs of the low-density cloud after the collisions, extending far beyond the planet. In the scope of this project, the long-term evolution of the planets after the collisions was not investigated. It would be interesting to investigate how long these debris clouds can remain visible and observable. The time scale is expected to depend on the local environment, specifically the orbits of the other planets and whether these can disrupt the cloud during close encounters. From determined relaxing times of protoplanets, the low-density clouds is expected to be accreted within 10^7 – 10^{10} years if it is not before then dissipated by external perturbations.

Observations of a few stars have revealed signatures of large concentrations of dust believed to be the aftermath of collisions (Mamajek & Meyer 2007; Lisse et al. 2009). These were collisions involving rocky planets rather than gas giants, which is expected since rocky planets form in tighter orbits where collisions rates are higher. These systems have been identified as hosts of past collisions through the observation of large amounts of debris which cannot be explained as protoplanetary debris.

The types of collisions discussed in Section 6.3.1 revealed how the most energetic collisions with large V_∞ and small periapsides ($R_{\text{per}} \leq 0.1$ R_J) generate bloated planets with low densities. These small periapsides causes large amount of kinetic energy to be converted into thermal energy, which bloats the planet remnant(s). These types of collisions are interesting as recent observations have revealed a number of such low-density planets (Anderson et al. 2010; Latham et al. 2010). The observed bloated planets are however believed to be the result of environment rather than past collisions, as they orbit their host star in tight orbits and tidal forces causes the planets to bloat. Distinguishing these inflated planets resulting from collisions or proximity to the host star will be difficult.

Our model only consisted of one single polytropic profile, while Jupiter-like planets are believed to have a solid core structure surrounded by a large gaseous envelope. Anic et al. (2007) investigated collisions between young Jupiters and Earth-like projectiles, and found that the presence of a Jupiter core did not affect results significantly. However, there are no results showing that the same is true for collisions between gas giants. It would therefore be interesting to investigate further the impact of a core, for example by using two or more combined polytropic profiles.

In conclusion, we have found that collisions between gas giant planets are more probable in tight planetary systems where the gas giants have moved into tighter orbits (due to migration or planet-planet scattering). These collisions can have large impact velocities and mass loss from the systems can reach $\sim 10\%$. A fraction of the bound material constitutes a large debris cloud engulfing the remnant(s). Debris clouds may be observable but more investigation is needed to determine the time scale of these clouds before they are dissipated due to perturbations of other planets or accretion by the planet. Mergers are more likely to occur for planets in wide orbits, where the impact velocities are lower and a lower energy loss is required for the planets to merge. Through mergers, planets can increase their mass up to approximately 50%, which show that planets may build-up in mass through collisions in young planetary systems or older planetary systems with induced instabilities from stellar fly-bys as an example.

References

Anderson, D. R., Hellier, C., Gillon, M., et al. 2010, ApJ, **709**, 159

Anic, A., Alibert, Y., & Benz, W. 2007, A&A, **466**, 717

Bahcall, J. N. 2005, Physica Scripta Volume, **T121**, 46

Baraffe, I., Chabrier, G., & Barman, T. 2010, Reports on Progress in Physics, **73**, 016901

Barnes, J. & Hut, P. 1986, Nature, **324**, 446

Bate, M. 1995, PhD thesis, Univ. Cambridge

Batygin, K. & Laughlin, G. 2008, ApJ, **683**, 1207

Benz, W. 1984, A&A, **139**, 378

Benz, W. 1990, in Numerical Modelling of Nonlinear Stellar Pulsations Problems and Prospects, ed. J. R. Buchler, 269–288

Benz, W., Slattery, W. L., & Cameron, A. G. W. 1988, Icarus, **74**, 516

Benz, W., Slattery, W. L., & Cameron, A. G. W. 1989, Meteoritics, **24**, 251

Bobrov, A. M., Vasil'Ev, P. P., Zharkov, V. N., & Trubitsyn, V. P. 1978, Soviet Astronomy, **22**, 489

Borucki, W. J., Koch, D. G., Basri, G. B., et al. 2003, in Astronomical Society of the Pacific Conference Series, Vol. **294**, Scientific Frontiers in Research on Extrasolar Planets, ed. D. Deming & S. Seager, 427–440

Cameron, A. G. W. & Benz, W. 1991, Icarus, **92**, 204

Canup, R. M. 2005, Science, **307**, 546

Chabrier, G., Baraffe, I., Leconte, J., Gallardo, J., & Barman, T. 2009, in American Institute of Physics Conference Series, ed. E. Stempels, Vol. **1094**, 102–111

Chambers, J. E. 1999, MNRAS, **304**, 793

Chambers, J. E., Wetherill, G. W., & Boss, A. P. 1996, Icarus, **119**, 261

Chatterjee, S., Ford, E. B., Matsumura, S., & Rasio, F. A. 2008, ApJ, **686**, 580

Collins, G. W. 1989, The fundamentals of stellar astrophysics

Cumming, A., Butler, R. P., Marcy, G. W., et al. 2008, PASP, **120**, 531

Dale, J. E. & Davies, M. B. 2006, MNRAS, **366**, 1424

Davies, M. B., Benz, W., & Hills, J. G. 1991, ApJ, **381**, 449

Fortney, J. J. & Nettelmann, N. 2009, The Interior Structure, Composition, and Evolution of Giant Planets, http://www.springerlink.com/content/h088j883105k5813/?p=c5adb50a5f1a494296fa9255c09985f5

G. P. Horedt, ed. 2004, Astrophysics and Space Science Library, Vol. **306**, Polytropes - Applications in Astrophysics and Related Fields

Geroyannis, V. S. 1993, Earth Moon and Planets, **61**, 131

Gingold, R. A. & Monaghan, J. J. 1977, MNRAS, **181**, 375

Gladman, B. 1993, Icarus, **106**, 247

Guillot, T. 1999, Science, **286**, 72

Hamilton, C. 1995, NASA STI/Recon Technical Report N, **95**, 27326

Hernquist, L. & Katz, N. 1989, ApJS, **70**, 419

Ida, S. 2010, in EAS Publications Series, ed. T. Montmerle, D. Ehrenreich, & A.-M. Lagrange, Vol. **41**, 339–354

Kessler, D. J. 1981, Icarus, **48**, 39

Latham, D. W., Borucki, W. J., Koch, D. G., et al. 2010, ApJL, **713**, 140

Lindegren, L. 2010, in IAU Symposium, ed. S. A. Klioner, P. K. Seidelmann, & M. H. Soffel, Vol. **261**, 296–305

Lisse, C. M., Chen, C. H., Wyatt, M. C., et al. 2009, ApJ, **701**, 2019

Liu, G. R. & Liu, M. B. 2007, Smoothed Particle Hydrodynamics: a meshfree particle method, ed. Liu, G. R. and Liu, M. B.

Lubow, S. H. & Ida, S. 2010, arXiv:0706.1234v1 [ph.EP]

Lucy, L. B. 1977, AJ, **82**, 1013

Mamajek, E. E. & Meyer, M. R. 2007, ApJL, **668**, 175

Marchi, S., Ortolani, S., Nagasawa, M., & Ida, S. 2009, MNRAS Letter, **394**, 93

Marcus, R. A., Stewart, S. T., Sasselov, D., & Hernquist, L. 2009, ApJL, **700**, 118

Marzari, F. & Weidenschilling, S. J. 2002, Icarus, **156**, 570

Mayor, M. & Queloz, D. 1995, Nature, **378**, 355

Melosh, H. J. 1989, in Impact Cratering - a Geologic Process (New York: Oxford University Press)

Mohanty, S., Jayawardhana, R., Huélamo, N., & Mamajek, E. 2007, ApJ, **657**, 1064

Monaghan, J. J. & Lattanzio, J. C. 1985, A&A, **149**, 135

Paczyński, B. 1971, ARA&A, **9**, 183

Perryman, M. A. C. 2003, in Astronomical Society of the Pacific Conference Series, Vol. **298**, GAIA Spectroscopy: Science and Technology, ed. U. Munari, 3–12

Prialnik, D. 2010, An Introduction to the Theory of Stellar Structure and Evolution

Safronov, V. S. 1972, Evolution of the protoplanetary cloud and formation of the earth and planets.

Saumon, D., Chabrier, G., & van Horn, H. M. 1995, ApJS, **99**, 713

Stern, S. A. 1992, ARA&A, **30**, 185

Stoer, J. & Bulirsch, R. 1980, Introduction to Numerical Analysis, ed. N. Y. Springer-Verlag

Urey, H. C. 1951, Geochim. Cosmochim. Acta, **1**, 209

Wetherill, G. W. 1990, Annual Review of Earth and Planetary Sciences, **18**, 205

Wiechert, U., Halliday, A. N., Lee, D., et al. 2001, Science, **294**, 345

A Program Manuals

A number of programs have been used for the various aspects of the project. The aim of the project was to do a number of different collisions between Jupiter-like planets and determine the requirements for mergers and mass losses due to the collision. All steps of the project are described here; from generating planet models to analyzing the results of the SPH runs. The programs used in the project are listed in Table (11) with a short description of their use.

Program	Description
MERCURY	Generate statistics on initial parameters for the planet collisions
LEQ	Solves the Lane-Emden equation and generates planet models
SPH	Initiates and iterates the planet collisions using results from LEQ and parameters from MERCURY

Table 11: List of programs used in the project and their use.

The programs will be discussed here together with a short tutorial of their use. MERCURY will be discussed in the next section, which was used to attain statistics on the collisional parameters that the simulations were initiated with.

A.1 In summary

Below is a quick summary of the steps; from generating a planet model to analyzing post-collision results.

- First create a directory for the simulation. Preferably describe essential details of the run in the directory name such as the collision parameters and model properties (object masses, periapsides and velocity at infinity).
- Inside the directory, initiate the LEQ program and refer to the tutorial in Section A.3.1 for information on the required inputs. An output named MODEL_1_PLANET with the polytropic model is generated in the working directory.
- Convert the polytropic model into an SPH model by calling the STARBUILDER_NG program, located in the folder ./PROGRAMS/INIT_CONDITIONS_CODE from the working directory (see tutorial in Section A.4.1 for details). Make sure the program loads the correct file name which was generated by the LEQ program as the file name is hardcoded.

- Load each of the SPH planet models into the SPH code and iterate them individually to make sure the planet models are in complete hydrostatic equilibrium (refer to the tutorial in Section A.4.2 for details). Unless this is done, the planets may show unphysical behavior prior to the collision, which may affect the results of the collisions.

- Load both the relaxed planet models into the STARCOLLIDER program, which will initialize the models for the collisions (see tutorial in Section A.4.3 for help on the required inputs). The collision parameters V_∞, $R_{\rm per}$ and planet separation needs to be specified.

- Edit the MSBH001 file from the SPH program package to define the properties of the collision, and then initiate the run with the command ./SPH_TREE EVOLUTION MSBH001.

- Once the simulations are done, call the FINDESCIT program in the working directory to process the results (see tutorial in Section A.4.4). The program will analyze the planet remnant(s) after the collision and determine whether they are bound and destined for another collision.

A.2 MERCURY - Generating statistics on collisions

Statistics on the collision parameters were discussed in Section 5, where the N-body integrator MERCURY by Chambers (1999) was used to gather statistics. Using MERCURY a number of different systems were investigated with a range of orbits, listed in Table 3. The investigated systems consist of three Jupiter-like planets that are initiated with unstable orbits, as discussed previously in Section 5.3, which quickly allow perturbations to build up. This will cause the systems to experience numerous close encounters shortly after they are initiated, and the chance that some of the close encounters will in collisions becomes significant.

The MERCURY code has been modified in order to generate specific output with information on the collisions. This output contains information on the separation for the planets' closest approach and the corresponding time. Using this information the systems are rerun a second time with another modification of the code, which tracks the evolution of the planets and their properties prior to the collision. A tutorial for using MERCURY is presented below.

A.2.1 Tutorial - Using MERCURY

The information for initiating a run with MERCURY is found in two specific files; BIG.IN and PARAM.IN. The first file specifies the properties of the big objects such as the gas giants, with information on their orbits. The same information holds for smaller objects in the file SMALL.IN for terrestrial planets. In PARAM.IN the properties of the simulation are specified, such as simulation time, integration method and more.

A.3 LEQ - Generating a planet model

A method for generating the planet models was discussed in Section 2.2. The theory was implemented in the program LEQ, written for this project. The Lane-Emden equation (Eq. 2.18) can only be solved analytically for a small number of polytropic indices, and needs to be solved numerically otherwise. The LEQ program needs input from the user to determine the model properties. The radius is determined using the mass-radius relation discussed in Section 2.5 which is extrapolated from the mass and radius of Jupiter. The program step-wise determines the profile of the dimensionless potential $\theta(\xi)$. From the determined $\theta(\xi)$ profile the other properties of the planet, such as density and pressure profiles together with their central values, can be determined as was discussed in Section 2.3.

Column	Property	
1	N_{s}	– Shell number
2	θ	– Dimensionless potential function for the polytropic model
3	P_{s}	– Pressure in shell
4	ρ_{s}	– Mass density of shell
5	T_{s}	– Temperature of shell
6	$grga$	– *Unused parameter*
7	M_{s}	– Shell mass in units of $\mathrm{M}_{\odot}$
8	$[\mathrm{H}^{1}]$	– Hydrogen abundance
9	$[\mathrm{He}^{4}]$	– Helium abundance
10	$[\mathrm{C}^{12}]$	– Carbon abundance
11	R_{s}	– Shell radius
12	L_{s}	– Shell luminosity
13	E_{therm}	– Shell thermal energy
14	E_{nuc}	– Shell nuclear energy
15	E_{bind}	– Shell binding energy

Table 12: The output parameters generated by the LEQ program.

The program is dependent on input from the user for the polytropic index n, object mass M and number of shells for the model profile to be divided into. Two outputs are generated by running the program:

- TABLE1.TXT - Generates output of the dimensionless density profile θ, determined by stepwise calculating θ using its first and second derivative (refer to Section 2.4 for details).

- MODEL_1_PLANET - Model profile generated compatible with the reading subroutine in the SPH code. The columns in the output file contains the properties listed in Table 12.

Several of the properties such as composition were not investigated in this project, and hence LEQ will only print out hard-coded values for these properties. If LEQ is to be used for an extensive investigation of model composition after the collisions, proper values need to be generated.

A.3.1 Tutorial - Using LEQ

The program is situated in the folder LEQ. Compile the code by running the makefile and initiate it by running the command ./LEQ. The model needs to be divided into a number of slices for it to be compatible with the reading subroutine of the SPH code. The LEQ program asks for three inputs from the user that specify the polytropic index, mass and slices of the model and then generates two outputs; one for the dimensionless density profile θ and the second the model profile that is compatible with the SPH code. The required inputs are discussed below:

- Enter n, the polytropic index, of your object

  The polytropic index is a number between 0 to 5 (refer to Section 2.2 for discussion on polytropic indices).

- Enter object's mass

  Units are in Jupiter masses $M_J = 1.90 \times 10^{27}$ kg $= 0.000955$ $M_\odot$.

- Specify number of layers for the model

  A typical value is 200 layers. Number of slices will increase precision at which SPH can generate particles, but should not be made too large so that slice widths are comparable to mean particle separations.

A.4 SPH - Colliding the planet models

The SPH method used to simulate the planet collisions in this project has previously been discussed in Section (3). Simulation of the collisions are divided into four steps; (1) The polytropic models for the colliding planets are converted into SPH models (2) The two planets are iterated individually in order to relax the models. (3) A program initializes the planets with a specified velocity at infinity, initial separation and periapsis for the collision. (4) The collision run is started.

A.4.1 Tutorial - Generating SPH model

Polytropic models generated using LEQ are not compatible with SPH code, but needs to be converted before they can be used. The program STARBUILDER_NG converts the polytropic model into an SPH model by reading in the parameter profiles of the model, and distribute a number of particles to form the planet with attributes accordingly to the profiles. The program is found in the directory SIMULATION_CODE and is initialized with the command ./STARBUILDER_NG. Required inputs from the user are discussed below for the program.

- Specify core mass

  The unit is in solar radii. Specify mass of the core, if such is present.

- Specify core smoothing length

  The smoothing length at the core in units of solar radii. A large value may result in too many neighbors for the particles, significantly increasing computational time, while a low value will result in bad precision. A typical number of neighbors is ~ 50.

- Do you wish to exclude the core from the profile?

  Option used for steep density gradients close or at the core. A uniform sphere is generated with radius smaller that of the object, and then the model is stretched out to the radius while leaving a user specified inner region of the model intact. Option especially useful when modeling very dense objects such as white dwarfs or neutron stars.

- Specify particle number:

  Typical numbers are in the order of 10^4, high resolution simulation can use a magnitude larger (depends on computational power).

- Deform close-packed grid?

  Option used for objects with odd internal structures, such as red giants. It will ask for a radius of the grid and an inner radius, inside which no deformation will take place. The grid is then stretched out using a sinh or cosh function. This will give a large resolution in the core. Getting a good fit is however difficult and the user has to manually look at the profile afterwards and look out for particles with low masses or locally steep gradients.

- Requested number of particles: ...
  Actual number of particles: ...
  Is this OK?

  Yes, unless the number of particles is for some reason odd or incorrect for your use. If the answer is NO the program quits.

- Do you wish to add a point mass?

  A point can be added to represent the model core. Useful for very steep central density profiles as for dense objects.

- Set velocities to zero?

  Yes. Models should be iterated individually before the collision to make sure they are relaxed, setting the velocities to zero may speed this up.

A.4.2 Tutorial - Initiating SPH collisions

The next step is to initialize two models for the collision simulation. The models are not always generated in hydrostatic equilibrium. By simulating each of the models by themselves for a time until they have settled and no odd behaviors such as oscillations are evident. The same program used to iterate the collisions is used for this and is found in the folder SIMULATION_CODE. The program is initiated with the command ./SPH_TREE EVOLUTION MSBH001. A file named MSBH001 is used by the SPH program to read in parameters of the collisions such as time step and iteration time, and explanations to the parameters are found in the file. The program is used in the same way whether it is for relaxing the models or for simulating the collisions. The only difference is that the two models needs to be combined into one output, and the modeled objects initiated with specific collision parameters.

A.4.3 Tutorial - Initiate models for collisions.

As soon as both models are relaxed, they need to be initialized for the collision, by the user with a specified velocity at infinity, initial separation and periapsis. The program for this is ran with the command ./STARCOLLIDER, and the user is asked for input on the collision parameters. The different inputs required by the user from the program are discussed below.

- What type of collision - MS-MS(1) or MS-PM(2)?

  Program asks whether both objects are SPH models or if one of them is a point mass. The latter is useful when simulating collisions with very dense objects such as neutron stars or black holes.

- Enter binary file containing star 1/2 (7 char.):

  Program asks for the file name of the two (relaxed) models for the collisions. The files need to be in binary form.

- Enter name for combined file (7 char.):

  Input the name of your choice for the output file.

- Delete unbound particles from star 1?

  Answer yes(y) or no(n) if particles not bound to the first object (target) should be removed. If large amounts of material are removed, the model should probably be re-made.

- Specify relative velocity at infinity:

  Input the V_∞ for the objects, value in units of $\sqrt{GM_\odot/R_\odot} = 436.7$ km/s.

- Specify periapsis:

  Input $R_{\rm per}$ in units of $R_\odot$.

- Specify initial separation:

  Input the separation of the objects as the simulation is initiated in units of $R_\odot$. The program helps with giving information on the objects' Roche lobes, inside which the perturbations between the objects will be stronger than that of the host star.

- Is the target star (star 1) rotating?

  Your own choice. If the target is rotating, it will affect the rotation of the objects after the collision. With an initial rotation the target may be spun to high enough velocities for mass to become unbound and ejected.

- Limit hs?

  Limits the particle's smoothing lengths to a certain upper boundary. If particles have a longer smoothing length than the limit they will be removed (and mass is lost from the object). This is helpful if some particles have too many neighbors (and possibly a large smoothing length).

- Recalculate smoothing lengths?

  Decide whether smoothing lengths should be recalculated. This may be useful if some material has been lost (or removed) from the initial model.

A.4.4 Tutorial - Post-processing

After the collisions have been initiated the results can be extracted using a iterative procedure by Dale & Davies (2006). It determines the energy and mass loss of two colliding objects, and different versions exist for whether one of the objects are modeled by a point mass or not. The procedure begins with a simple estimation of the planet's COM, calculated from the particles that were bound to the planet prior to the collision. This is a crude estimation, especially for violent collisions, as material is ejected and transferred between the objects in the collision. The COM, and its velocity, is calculated by summing the contribution of each particle, weighted by their individual mass $m_{\rm p,i}$ as:

$$\boldsymbol{r}_{\rm com} = \frac{\sum_{i=1}^{N} m_{\rm p,i}\boldsymbol{r}_{\rm i}}{\sum_{i=1}^{N} m_{\rm p,i}} \tag{A.1}$$

$$\boldsymbol{v}_{\rm com} = \frac{\sum_{i=1}^{N} m_{\rm p,i}\boldsymbol{v}_{\rm p,i}}{\sum_{i=1}^{N} m_{\rm p,i}} \tag{A.2}$$

where $m_{\rm p,i}$ is the mass of the ith particle, and $r_{\rm i}$, $v_{\rm i}$ its position and velocity vectors respectively. After collisions the COM for bound particles can be determined for each remnant by calculating the total energy $E_{\rm t}$ as:

$$E_{\rm t} = E_{\rm kin} + E_{\rm int} + E_{\rm pot} \tag{A.3}$$

where $E_{\rm kin}$, $E_{\rm int}$ and $E_{\rm pot}$ are the kinetic, internal and potential energies respectively. An unbound particle will move away from the COM with a positive total energy, while a bound particle has a negative energy and is captured in the potential well of the planet, and from the remaining bound material a new COM can be determined. This procedure is repeated a number of iterations and in the end the energy and mass loss can be determined from the bound material to the remnant(s).

The program is called FINDESCIT and require a specific format of the read-in as the SPH code used by Dale & Davies (2006). Below the different required inputs from the user are discussed for the FINDESCIT program.

- Title

  Specify a title for the simulation, this will be printed in the output and can be used to distinguish different outputs.

- Name of binary file

  Binary file to be read in, if standard names have been used they consist of 4 characters and three digits.

- Input jump:

  Several dumps can be read in at the same time, specify here the jump or specifically the difference in dump numbers between compared dumps.

- How many jumps

  Specify how many dumps to analyze.

- Variable of state: 1:energy 2:entropy

  Specify whether energy or entropy is the variable for state, where other examples of variables of state are pressure, temperature and volume. This will depend on the input, the code of Dale & Davies (2006) implements energy. However, if entropy is chosen the variable of state is transformed into energy, using:

  $$u_i = \frac{u_i^{1+1/n}}{1+1/n}$$

  where n is the polytropic index and u_i the particles individual total specific energy.

- Dump number (9999=last)

  Each generated output may, depending on the number of particles and file size limitations, contain outputs of several time steps. Here the user specifies which of the dumps in the output that should be read.

B LEQ - Program code

```
       program Leq

c*****************************************************************
c* Program is a by Albertsson (2010) modified version of the    *
c* original code for solving the Land-Emden equation from:      *
c*  http://www.astro.utu.fi/~cflynn/Stars/l5.html               *
c*                                                              *
c* The program is written to solve the Lane-Emden equation      *
c*                                                              *
c* d^2x/dt^2 = - ((2/t)*(dx/dt) + x**n)                         *
c*                                                              *
c* where x is the dimensionless density function (denoted       *
c* theta in the thesis work)                                    *
c* and t is the dimensionless length (denoted xi in the thesis) *
c*                                                              *
c* initial conditions are      x = 1                            *
c*                          dx/dt = 0                           *
c*                                                              *
c* The polytropic index n has only known analytical soluations  *
c* for indices n = 0,1,5 and must otherwise be numerically      *
c* solved.                                                      *
c*                                                              *
c*                                                              *
c* The program is divided into two parts:                       *
c* (1) First the Lane-Emden equation is numericaly solved       *
c*     to find the root of the planet radius.                   *
c* (2) Then the structure profiles of the planets is            *
c*     calculated.                                              *
c*                                                              *
c*                                                              *
c* The program then generates an output for different object    *
c* characteristics of pressure, density, mass and temperature   *
c* which can be plotted versus radius. The output is then used  *
c* to distribute sph particles with the profiles as references. *
c*                                                              *
c*****************************************************************
real dxdt, n, dt, xlast, dxdtlast, M, Mu, Ru
       real V, RhoMean, ap, gamma, Ko, mp, k, dxdt1, t1
real RhoFrac,dR,R,aScale
real, allocatable :: xiN(:), thetaN(:), TempN(:), rhoN(:)
real, allocatable :: RadiusN(:), PN(:), MassN(:), dphidxN(:)
real, allocatable :: xi(:), theta(:), Temp(:), rho(:)
real, allocatable :: P(:), Radius(:), Mass(:), dphidx(:)
       integer steps,i,j,l, nshells, lastStep, shell
       character*50 name

      steps = 10000000

      allocate(xiN(steps))
      allocate(thetaN(steps))
      allocate(TempN(steps))
      allocate(rhoN(steps))
      allocate(RadiusN(steps))
      allocate(PN(steps))
      allocate(MassN(steps))
      allocate(dphidxN(steps))

      write(6,*) 'Enter n, the polytrope index '
400   continue
      read(5,*) n
```

```
      if (n.ge.5) then
         write(6,*) 'n is too big, star radius is infinite'
         write(6,*) 'Try again....'
         write(6,*) ''
         goto 400
      end if

      write(6,*) 'Enter the objects mass'
      read(5,*) M


      write(6,*) 'Enter number of slices for the model'
      read(5,*) nshells


* Initial values

      x    = 1.0
      dxdt = 0.0
      t    = 1.0E-6
      j    = 0

* Specify iteration step length dt
* The smaller the step the more accurate the calculation
* but the longer it takes!

      dt = 0.001

* Constants

      Mu = 1.90E30
      Ru = 7.15E09

* Determine planet radius through mass-radius relation of Chabrier (200X)

      R = M**(-1./8.)

* Convert radius and mass into Jupiter units

      M = M * Mu
      R = R * Ru


* open the file for output of results

      open(20,file='table1.txt',status='unknown')
      open(111,file='structure.txt',status='unknown')


* now the MAIN program loop

      do i = 1, steps
          j = j + 1

* calculate the next dxdt
          dxdt = dxdt - ( 2.0*dxdt/t + x**n )*dt

* calculate the next x
          x = x + dxdt*dt
```

```
* increment the dimensionless radius (move outward in the star)
          t = t + dt

* Save and print values of x (/theta) and t (/xi)
          thetaN(j) = x
          xiN(j) = t
          dphidxN(j) = dxdt

          write(20,*) t,x,dxdt

* check if the solution has become negative yet (iterated past planet radius)
          if (x.lt.0.0) goto 999

* save the current values of x and t, for interpolating the root later
              xlast = x
              dxdtlast = dxdt

       end do


999    continue

* calculate the position of the root, using the current x (which
* is the first value < 0, and the previous x (stored as xlast)
* which is the last calculated value which was still > 0

              t1 = t + (x/(xlast-x))*dt
              dxdt1 = dxdt - (t-t1)*(dxdt-dxdtlast)/dt

** This is the second part of the program which uses the root
** of the Lane-Emden equation which was just determined above


* Calculate constants of the structure equations
* Structure units are:
* density: g cm^-2
* temperature: K
* pressure: dyn cm^-2

              pi = 3.14159
              aScale = R / t1
              ap = - Mu / (4*pi * t1**2 * dxdt1)
              V = 4*pi*R**3 / 3
              RhoMean = M / V
              RhoC = -RhoMean * dxdt1**(-1) * t1 / 3

              G = 6.67259E-8
              mp = 1.67E-24
              k = 1.38E-16
              gamma = 1 + 1/n

              Pc = (G*M**2 / R**4) * (4*pi * (n+1) * dxdt1**2)**(-1)
              Tc = Pc * mp / (k * RhoC)
              Ko = Pc / (RhoC**gamma)
              RhoFrac = RhoC / RhoMean

* Calculate objects structure

              allocate(xi(j))
              allocate(theta(j))
              allocate(Temp(j))
              allocate(rho(j))
```

```
               allocate(P(j))
               allocate(Radius(j))
               allocate(Mass(j))
               allocate(dphidx(j))

               DO i = 1,j
                  xi(i) = xiN(i)
                  theta(i) = thetaN(i)
                  Temp(i) = TempN(i)
                  rho(i) = rhoN(i)
                  P(i) = PN(i)
                  Radius(i) = RadiusN(i)
                  Mass(i) = MassN(i)
                  dphidx(i) = dphidxN(i)

                  rho(i) = RhoC * theta(i)**n
                  P(i) = Ko*(rhoC**gamma)*theta(i)**(n+1)
                  Temp(i) = Tc*theta(i)
                  Radius(i) = a*xi(i)/Ru
                  Mass(i) = -4*pi*aScale**3*RhoC*xi(i)**2*dphidx(i)

                  write(111,*) Radius(i), rho(i), P(i), Temp(i), Mass(i)
               END DO

        close(111)


* Print structure to file in specified number of shells
* Data is printed backwards, i.e. from planet surface to the core

        dR = R / ( Ru * (nshells-1) )

        shell = nshells
        open(unit=88,file='model_1_planet',status='unknown')
        Ri = dR
        DO i = 1,lastStep

           if ( Radius(i).GT.Ri) then

              write(88,99009) shell-1,xi(i),P(i),rho(i),Temp(i),
     &        1.111E+07,Mass(i)/Mu,1.111E+07,1.111E+07,
     &        1.111E+07,Radius(i),1.111E+07,1.111E+07,
     &        1.111E+07,1.111E+07,1.111E+07

              Ri = Ri + dR
              shell = shell - 1
           end if
       END DO

       close(88)

        write(6,*) ' '
        write(6,*) ' '

* Print out model properties

        write(6,*) 'Properties of the generated planet model'
        write(6,*) '-------------------------'
        write(6,*) 'first root of theta at xi   = ',t1
        write(6,*) 'at this point dtheta/dxi    = ',dxdt1
        write(6,*) ' '
```

```
        write(6,*) '----Planet structure----'
        write(6,*) 'Planet radius          [Rj] = ', R/Rj
        write(6,*) 'Planet mass            [Mj] = ', M/Mj
        write(6,*) 'Polytropic index            = ', n
        write(6,*) ' '

        write(6,*) '----Central structure properties'
        write(6,*) 'Rho core / Rho mean         = ', RhoFrac
        write(6,*) 'Core density                = ', RhoC
        write(6,*) 'Core pressure  [dyn cm^-2]  = ', Pc
        write(6,*) 'Core temperature       [K]  = ', Tc
        write(6,*) 'K                           = ', Ko
        write(6,*) ' '
        write(6,*) '...'
        write(6,*) 'Structure printed to file model_1_planet'
        write(6,*) 'Model divided into number of shells: ', nshells
        write(6,*) ' '


99009 FORMAT (I4, 1P, 15E10.3)
        end
```

C Tables of collision runs

Tables where all available information from the collision simulations are listed in this Appendix. The tables show the collisional parameters and values for energy and mass loss, the energy conservation error and comments on the simulations are listed.

V_∞ [km/s]	$R_{\rm per}$ $R_{\rm J}$	$\Delta E/E$ –	$\Delta M/M_0$ –	$\Delta M/M_1$ –	$\Delta M/M_2$ –	$E_{\rm err}/E_{\rm min}$ –	Comments
20	0.0	IM	3.20×10^{-2}	–	–	1.26	Instantly merge
	0.1	IM	2.82×10^{-2}	–	–	0.91	Instantly merge
	0.5	–4.79	1.57×10^{-2}	–	–	0.73	Returns and merge
	1.0	–3.82	8.87×10^{-3}	–	–	0.59	Returns and merge
	1.5	–2.69	4.99×10^{-3}	–	–	0.46	Returns and merge
	2.0	–1.86	3.17×10^{-3}	–	–	0.29	Grazing, returns and merge
	2.5	–0.62	0.00	–	–	0.23	Grazing, no mass loss
60	0.0	IM	6.66×10^{-2}	–	–	1.37	Instantly merge
	0.1	IM	6.50×10^{-2}	–	–	1.17	Instantly merge
	0.5	–1.93	4.65×10^{-2}	–	–	0.891	Returns and merge
	1.0	–1.10	1.86×10^{-2}	–	–	0.623	Returns and merge
	1.5	–0.410	2.18×10^{-3}	1.11×10^{-3}	1.07×10^{-3}	0.521	Hit-and-run
	2.0	–0.0910	4.52×10^{-5}	1.94×10^{-5}	2.60×10^{-5}	0.322	Grazing
100	0.0	IM	3.21×10^{-1}	–	–	1.58	Instantly merge
	0.1	IM	3.41×10^{-1}	–	–	1.25	Instantly merge
	0.5	–1.42	2.69×10^{-1}	–	–	0.938	Returns and merge
	1.0	–0.430	5.15×10^{-2}	2.56×10^{-2}	2.59×10^{-2}	0.674	Hit-and-run
	1.5	–0.0702	6.92×10^{-3}	3.47×10^{-3}	3.45×10^{-3}	0.567	Hit-and-run
	2.0	–0.0130	7.31×10^{-6}	3.57×10^{-6}	3.74×10^{-6}	0.353	Grazing

Table 13: Full summary of collisions with primary mass $M_1 = 1$ $M_{\rm J}$. Properties listed are $V_\infty, R_{\rm per}$, energy and mass losses and the energy conservation error.

V_∞ [km/s]	$R_{\rm per}$ $R_{\rm J}$	$\Delta E/E$ –	$\Delta M/M_0$ –	$\Delta M/M_1$ –	$\Delta M/M_2$ –	$E_{\rm err}/E_{\rm min}$	Comments
20	0.0	IM	2.33×10^{-2}	–	–	1.95	Instantly merger
	0.1	IM	2.06×10^{-2}	–	–	1.23	Instantly merge
	0.5	–2.45	1.50×10^{-2}	–	–	0.603	Secondary disrupted
	1.0	–2.21	8.62×10^{-3}	–	–	0.365	Returns and merge
	1.5	–1.86	4.79×10^{-3}	–	–	0.339	Returns and merge
	2.0	–1.24	1.68×10^{-3}	–	–	0.250	Grazing, returns and merge
	2.5	–0.29	0.00	–	–	0.213	Grazing, no mass loss
60	0.0	IM	4.06×10^{-2}	–	–	2.53	Instantly merger
	0.1	IM	3.86×10^{-2}	–	–	1.87	Instantly merge
	0.5	–1.36	3.23×10^{-2}	–	–	0.951	Secondary disrupted
	1.0	–0.880	1.04×10^{-2}	3.72×10^{-3}	6.67×10^{-3}	0.547	Hit-and-run
	1.5	–0.360	2.42×10^{-3}	5.57×10^{-4}	1.86×10^{-3}	0.285	Hit-and-run
	2.0	–0.0703	4.13×10^{-5}	0.00	4.13×10^{-5}	0.166	Grazing
100	0.0	IM	8.22×10^{-2}	–	–	2.68	Instantly merger
	0.1	IM	9.10×10^{-2}	–	–	2.21	Instantly merge
	0.5	–1.17	8.90×10^{-2}	–	–	1.34	Returns and merge
	1.0	–0.442	3.56×10^{-2}	8.73×10^{-3}	2.69×10^{-2}	0.717	Hit-and-run
	1.5	–0.107	5.42×10^{-3}	1.15×10^{-3}	4.27×10^{-3}	0.594	Hit-and-run
	2.0	–0.0157	4.43×10^{-7}	1.17×10^{-7}	3.26×10^{-7}	0.392	Grazing

Table 14: Full summary of collisions with primary mass $M_1 = 3$ M_J. Properties listed are $V_\infty, R_{\rm per}$, energy and mass losses and the energy conservation error.

V_∞ [km/s]	$R_{\rm per}$ $R_{\rm J}$	$\Delta E/E$ –	$\Delta M/M_0$ –	$\Delta M/M_1$ –	$\Delta M/M_2$ –	$E_{\rm err}/E_{\rm min}$ –	Comments
20	0.0	IM	2.87×10^{-2}	–	–	2.36	Instantly merge
	0.1	IM	2.50×10^{-2}	–	–	1.67	Instantly merge
	0.5	–2.19	2.32×10^{-2}	–	–	1.02	Returns and merge
	1.0	–1.97	1.64×10^{-2}	–	–	0.693	Returns and merge
	1.5	–1.72	1.19×10^{-2}	–	–	0.492	Returns and merge
	2.0	–1.09	6.21×10^{-3}	–	–	0.333	Grazing, returns and merge
	2.5	–0.17	0.00	–	–	0.270	Grazing, no mass loss
60	0.0	IM	4.55×10^{-2}	–	–	2.65	Instantly merge
	0.1	IM	4.33×10^{-2}	–	–	2.00	Instantly merge
	0.5	–1.24	3.93×10^{-2}	–	–	1.23	Secondary disrupted
	1.0	–0.650	2.30×10^{-2}	8.32×10^{-3}	1.47×10^{-2}	0.744	Hit-and-run
	1.5	–0.316	4.52×10^{-3}	3.48×10^{-4}	4.19×10^{-3}	0.453	Hit-and-run
	2.0	–0.0552	1.80×10^{-4}	2.01×10^{-6}	1.78×10^{-4}	0.327	Grazing
100	0.0	IM	7.80×10^{-2}	–		2.81	Instantly merge
	0.1	IM	8.21×10^{-2}	–		2.42	Instant merge
	0.5	–1.09	1.14×10^{-1}	–		1.75	Secondary disrupted
	1.0	–0.256	6.41×10^{-2}	1.96×10^{-2}	4.45×10^{-2}	0.885	Hit-and-run
	1.5	–0.0523	1.22×10^{-2}	1.92×10^{-4}	1.20×10^{-2}	0.657	Hit-and-run
	2.0	–0.00512	5.10×10^{-6}	4.02×10^{-7}	5.27×10^{-6}	0.342	Grazing

Table 15: Full summary of collisions with primary mass $M_1 = 5$ M_J. Properties listed are $V_\infty, R_{\rm per}$, energy and mass losses and the energy conservation error.